Doctoral Dissertation

CONTINUOUS DISPLACEMENT MONITORING BY USING GPS AND ITS APPLICATION TO A LARGE-SCALE STEEP SLOPE

（GPS による連続変位計測と長大急傾斜斜面への適用に関する研究）

March, 2019

NGUYEN TRUNG KIEN

Graduate School of Sciences and Technology for Innovation

Yamaguchi University

ABSTRACT

Continuous monitoring is very important for predicting the displacement behavior of slopes and for designing countermeasures against it. For instance, continuous monitoring is essential for large-scale steep slopes where the ground is likely to be unstable and great damage will be caused if the slopes collapse. It is known to be technically difficult to precisely and continuously monitor the displacement at such sites.

Recent studies have shown that the Global Positioning System (GPS) has the potential to continuously and precisely monitor displacements over extensive areas in civil and mining projects. Although GPS can measure three-dimensional displacements with mm accuracy for baseline lengths of less than 1 km, the measurement results include fatal errors due to obstructions above the antennas and tropospheric delays caused by weather conditions.

The objective of this research is to establish a method for precise slope monitoring by using GPS. The research includes

- Verification of the applicability of error-correction methods for reducing the influence of obstructions above the antennas and tropospheric delays at a large-scale steep slope for long-term monitoring;

- Discussion on the mechanism of the occurrence of large displacements of the slope due to an increase in the groundwater level by a numerical analysis based on the monitoring results;

- Investigation of the measurement performance of new GPS sensors, developed inexpensively compared with the current sensor, which can be installed at many points and can monitor displacements at any interval.

Chapter 1 describes the problem setting in this study and the organization of the dissertation, and Chapter 2 presents a literature review of GPS application for displacement monitoring together with an outline of GPS.

In Chapter 3, the applicability of error-correction methods for reducing the effects of obstructions above the antennas and tropospheric delays is investigated using GPS for displacement monitoring at a large-scale steep slope. As a result of applying the error-correction methods, the errors are reduced and/or eliminated from the

measurement results, and the measurement accuracy is improved. Thus, it is shown that monitoring results without errors can be obtained. Furthermore, the displacement results by GPS are compared with those by an extensometer and the Diffusion Laser Displacement Meter. It is found that the measurement sensitivity of the GPS displacement monitoring system is almost equivalent to that of the extensometer and the Diffusion Laser Displacement Meter.

Chapter 4 shows the results of long-term continuous monitoring at the slope using the error-correction methods described in Chapter 3. It is illustrated that the displacement could be continuously monitored with standard deviations of 1-2 mm in the horizontal direction and 3-4 mm in the vertical one without missing any data. During the measurement period, the groundwater level rose due to heavy rainfalls, the displacement greatly increased, and then parts of the slope were unstable in some cases. Thus, the mechanism of the occurrence of large displacements of the slope due to the increase in the groundwater level was investigated by numerical simulations based on the displacement monitoring results.

In the future, in order to conduct GPS monitoring more effectively, it will be necessary to install an inexpensive sensor at many points. In addition, it will also be essential to reduce the measurement interval from one hour to shorter intervals corresponding to the actual displacement behavior. New GPS sensors, which are capable of meeting such demands, are desired.

In Chapter 5, the measurement accuracy and the appropriate measurement intervals for the measurement performance by two new GPS sensors are investigated using the kinematic method. Fundamental experiments are conducted using the kinematic method with a 1-second measurement interval in which the baseline length and the height difference between the reference point and the observation point are changed. Standard deviations are improved by the arithmetic average of the 1-second kinematic results. Furthermore, experiments for detecting displacement are carried out. Field experiments with the new sensors are conducted at the slope discussed in Chapters 3 and 4.

Finally, Chapter 6 draws conclusions from the dissertation and discusses recommendations for future research works.

To

my father and mother
for their love and support.

ACKNOWLEDGMENTS

PREFACE

This dissertation is hereby submitted to the Graduate School of Sciences and Technology for Innovation of Yamaguchi University as part of the requirements for the degree of Doctor of Engineering. The research described herein was conducted under the supervision of Prof. Norikazu Shimizu and Assoc. Prof. Shinichiro Nakashima of the Department of Civil and Environmental Engineering, Yamaguchi University. The manuscript is an original contribution by the author, except where acknowledgements and references are made to previous studies. Part of this work has already been presented in the publications given below.

1. Peer-reviewed journal paper

a. Shinichiro Nakashima, Yota Furuyama, Yuichiro Hayashi, **Nguyen Trung Kien**, Norikazu Shimizu, Seiichi Hirokawa. Accuracy enhancement of GPS displacements measured on a large steep slope and results of long-term continuous monitoring. Journal of the Japan Landslide Society 2018;55(1):13-24.

This paper presents the verification of the applicability of error-correction methods for reducing the influence of obstructions above antennas and tropospheric delays at a large steep slope. Furthermore, the GPS displacement monitoring system and the error-correction methods were applied for long-term monitoring of the displacement at the slope. The error-correction methods presented in this paper are included in Chapter 3 of this dissertation. The long-term monitoring results in this paper, together with recent monitoring results, are included in Chapter 4.

2. Peer-reviewed conference proceedings paper

a. **Nguyen Trung Kien**, Shinichiro Nakashima, Norikazu Shimizu. Mechanism of landslide behavior at an unstable steep slope based on field measurements and a numerical analysis: a case study. In: Proceedings of ARMS 10th Asian Rock Mechanics Symposium – The ISRM International Symposium for 2018. Singapore; 2018.

This paper presents the displacement results at a large-scale steep slope monitored with GPS. Based on the monitoring results, it is seen that local collapses have occurred in some cases of the slope due to the increase in the groundwater level after rainfall events. Hence, the mechanism of the displacement behavior of the slope was investigated by considering both field measurements and numerical simulations. The results of this paper are included in Chapter 4 of this dissertation.

3. **Non-peer-reviewed conference proceedings papers**

   a. **Nguyen Trung Kien**, Yuichiro Hayashi, Shinichiro Nakashima, Norikazu Shimizu. Long-term displacement monitoring using GPS for assessing the stability of a steep slope. In: Proceedings of the 2017 ISRM Young Scholars' Symposium on Rock Mechanics (YSRM 2017 – an ISRM Specialized Conference) and the 2017 International Symposium on New Developments in Rock Mechanics and Geotechnical Engineering (NDRMGE 2017). Jeju; 2017. p. 165 – 168.

   This paper presents an outline of the GPS monitoring system and continuous displacement monitoring results using GPS at a large-scale steep slope. The results of this paper are included in Chapter 4 of this dissertation.

   b. **Nguyen Trung Kien**, Yuichiro Hayashi, Shinichiro Nakashima, Norikazu Shimizu. Displacement monitoring using GPS for a steep and large slope. In: Proceedings of 37th West Japan Symposium on Rock Engineering. Yamaguchi; 2016. p. 83 – 90.

   This paper provides an outline of the GPS monitoring system, the error-correction methods, and practical application for monitoring slope stability. The contents of this paper are included in Chapters 3 and 4 of this dissertation.

   c. **Nguyen Trung Kien**, Shinichiro Nakashima, Norikazu Shimizu. Consideration of mechanism of landslide behavior at an unstable slope caused by changes of the groundwater level. In: Proceedings of 39th West Japan Symposium on Rock Engineering. Nagasaki; 2018. p. 36 – 39.

   This paper describes the results of numerical simulations to understand the mechanism of the displacement behavior considering changes in the groundwater level. Part of this paper is included in Chapter 4 of this dissertation.

4. **Extended abstract**

   a. **Nguyen Trung Kien**, Shinichiro Nakashima, Norikazu Shimizu. Mechanism of landslide behavior at an unstable slope caused by changes of the groundwater level. In: Proceedings of the 20th International Summer Symposium – The 73rd Annual Conference of the Japan Society of Civil Engineers. Sapporo; 2018.

   This extended abstract describes the results of numerical simulations to understand the mechanism of the displacement behavior considering changes in the groundwater level. Part of this paper is included in Chapter 4 of this dissertation.

TABLE OF CONTENTS

LIST OF FIGURES

LIST OF TABLES

LIST OF ACRONYMS

GPS	Global Positioning System
GNSS	Global Navigation Satellite System
ISRM	International Society for Rock Mechanics and Rock Engineering
EDM	Electronic Distance Meter
TDR	Time Domain Reflectometry
DLDM	Diffusion Laser Displacement Meter
SAR	Synthetic Aperture Radar
LOS	Line of Sight
DInSAR	Differential Interferometry Synthetic Aperture Radar
C/A-code	Coarse/Acquisition-code
P-code	Precision-code
WGS84	World Geodetic System 1984
DoD	Department of Defense
JGD2000	Japanese Geodetic Datum 2000
CR-InSAR	Corner Reflector Interferometric Synthetic Aperture Radar
ZTD	Zenith Tropospheric Delay
DEM	Distinct Element Method
UDEC	Universal Distinct Element Code
GWL	Groundwater level
RTK	Real-time kinematic

LIST OF SYMBOLS

Δt_i	Measured travel times of codes from four satellites
ρ	Measured code pseudoranges between the receiver and the satellites
c	Speed of light in vacuum 2.99792458 x 10^8 m/s
δ_t	Unknown clock bias
x_i, y_i, z_i	Coordinates of satellites from navigation message transmitted from satellites
X, Y, Z	Unknown coordinates of receiver point
$\lambda,\ \Phi,\ h$	Longitude, latitude, and height
ϕ_{mi}^k	Signal phase from satellite k to observation point mi
r_{mi}^k	Distance from satellite k to observation point mi
$I_{\phi mi}^k$	Ionospheric delay (error) of signal phase from satellite k to observation point mi
$T_{\phi mi}^k$	Tropospheric delay (error) of signal phase from satellite k to observation point mi;
δt_{mi}	Receiver mi clock bias (error)
δt^k	Satellite k clock bias (error)
λ	Wavelength of signal
N_{mi}^k	Unknown integer ambiguity from satellite k to observation point m_i
$\varepsilon_{\phi mi}^k$	Observation error of signal phase from satellite k to observation point m_i
ϕ_{mi-mr}^{k-l}	Double-phase difference between observation point mi and reference point mr for satellite k and l
a	Semi-major axis
b	Semi-minor axis
$1/f$	Reciprocal flattening
f	Inverse flattening
ω	Earth's angular velocity
GM	Earth's gravitational constant

X, Y	Northing, Easting
m_0	Scale factor
φ_0	Latitude of origin
λ_0	Central meridian
B	Meridian arc length
y	Measurement value
u_0	Exact value
ε_p	Error due to signal disturbance caused by obstruction above antenna
ε_T	Error due to tropospheric delay
ε_R	Random error due to receiver noise
ΔR^{Trop}	Tropospheric delay
N^{Trop}	Refractivity
N_d^{Trop}	Dry component of tropospheric delay
N_w^{Trop}	Wet component of tropospheric delay
$N_{d,0}^{Trop}$	Refractivity of dry component
$N_{w,0}^{Trop}$	Refractivity of wet component
h_d	Height of dry component
h_w	Height of wet component
h	Height above surface
p	Atmospheric pressure
e	Partial pressure of water vapor
T	Absolute temperature
RH	Humidity
y'_n	Corrected measurement results with random errors
u_n	Estimates for exact values of displacements
D_t	Measurement interval
t	Progressing time
Δ	Operator for finite difference
Δ^k	Rank "k" difference

v_n, ε_{Rn}	White noises with average value of 0, standard deviation of τ, and observation error with standard deviation of σ.
j_{kn}	Normal stiffness of discontinuity
j_{ks}	Shear stiffness of discontinuity
j_{fric}	Friction angle of discontinuity
j_{coh}	Cohesion of discontinuity
j_{perm}	Permeability factor
a_{res}	Residual hydraulic aperture
a_{zero}	Aperture at zero normal stress
h_w	Groundwater height measured from level of slope toe on right-hand side
h_d	Discontinuity height measured from level of slope toe on right-hand side

Chapter 1
INTRODUCTION

1.1. General background

A landslide is "the movement of a mass of rock, earth or debris down a slope" (Cruden, 1991). It is one of the most serious natural hazards in mountainous areas. It often occurs suddenly and causes a threat to human life, the economy, etc. Due to changes in climate, fast population growth, a rise in infrastructural construction, etc., the tendency and frequency of the occurrence of landslides have increased and reached alarming rates in many countries (Saito et al., 2014; Dou et al., 2015; Avila et al., 2016; Scaringi et al., 2018). Two relevant peculiarities of landslides are their widespread spatial distribution and their inclination to be highly influenced by both human and natural factors that induce changes in the slope and the controlling factors (Gutiérrez et al., 2010). Landslides are also characterized as being time-dependent (Flageollet, 1996; Qin et al., 2001). A natural slope that has been stable for many years may suddenly collapse due to changes in topography, groundwater flows, the loss of strength, etc. (Abramson et al., 2002). In general, these failures may not be very well understood until the failure actually occurs and brings about the necessity to consider them. According to Hoek et al. (2000), rock slope failures are geological events that are controlled by natural physical processes. Although many researchers have investigated various ways to predict future failures of slopes, attempting to understand the mechanism behind large-scale failures is still a challengeable task.

The quest to understand the displacement (deformation) behavior of a slope has resulted in the development of various slope monitoring techniques. On the other hand, monitoring data play an important role in assessing slope stability, in predicting future slope behavior, and in designing countermeasure works. The monitoring techniques are based on different types of sensors, for instance, remote sensing, photogrammetric, and geodetic sensors, as well as geotechnical instruments, etc. These methods can also be divided into conventional and more recent techniques. To monitor the evolution of landslides, especially active landslides, the method should provide the real-time

evolution of the displacement. Therefore, this dissertation considers an automatic displacement monitoring system that can be used in real-time applications.

Using satellite remote sensing techniques provides the potential for understanding the landslide processes and for detecting displacements with sub-centimeter accuracy (Yin et al., 2010). However, the temporal resolution is limited by the frequency of the satellites traveling over an actual area, and these techniques are limited to episodic applications.

Airborne photogrammetry is a method that compares pictures taken at different epochs in time (Chandler and Moore, 1989). Although it is effective for determining long-time slow-moving landslides, it has the same problem of being episodic. It is impossible to perform real-time monitoring with this technique.

Several geotechnical techniques have been conventionally employed to monitor the displacement of grounds and structures, etc. Extensometers are used to measure the changes in distance between two points. Inclinometers are applied to measure the slope of initially straight boreholes. Piezometers are used to measure pore water pressure, and tiltmeters are used to measure the deviation from a horizontal plane, etc. However, all these conventional geotechnical techniques can only be applied to limited areas.

The last group of techniques are geodetic; they can be divided into two subgroups, ground-based and satellite-based systems. The first subgroup, the ground-based techniques, apply leveling instruments, total stations, laser scanners, etc., and can perform an episodic monitoring program. However, these techniques are not only very labor intensive, but they are also expensive to use, especially when high temporal resolution is required. Another drawback is that it is troublesome to perform absolute displacement analyses with them in cases where the distance to the fixed points is long, which often occurs in high-risk landslide areas. The second subgroup, the satellite-based systems, makes use of the available Global Navigation Satellite Systems (GNSS), such as GPS, GLONASS, GALILEO, etc. These systems show the potential to measure baselines with high accuracy over long distances and extensive areas without any demand for a line-of-sight between receivers in real-time.

2

1.2. Problem statement

Landslides cause many problems to human life, property and constructed facilities, infrastructures, and the natural environment. Mitigation is an urgent task to reduce the effects of landslides. There are four basic strategies for mitigating a particular landslide (Smelser, 2014):

- Stabilization
- Protection
- Avoidance
- Maintenance and monitoring

This research will be focused on the aspect of monitoring. Various techniques for assessing slope deformation have been studied to facilitate the design of countermeasures and to understand the mechanism of slope behavior. The question arises as to *which parameters are most significant* (Dunnicliff, 1988). The measurements of pressure, stress, load, strain, and temperature are often influenced by the specific conditions within a very small zone or the location of the slope. On the other hand, these parameters are dependent on the local characteristics of the zone. Therefore, they may not represent the conditions on a larger scale. In the case of requiring a large number of measurement points before confidence can be placed in the data, displacement (deformation) measurements can be meaningful and reliable. In addition, displacement monitoring is often the simplest way to examine the evolution of slope failure. Hence, displacement is chosen as the parameter for monitoring in this research.

The Global Positioning System (GPS) is a satellite-based positioning system. Nowadays, GPS is widely used to monitor the deformation of grounds and structures. Moreover, it is recognized that the GPS monitoring system can provide three-dimensional displacements with mm accuracy over extensive areas.

On the other hand, the GPS measurement results are generally scattered due to various error sources. To guarantee the reliability of the measurement results, some appropriate methods should be applied to reduce and/or eliminate the errors included in the measurement results. The errors due to tropospheric delays can be corrected by using an appropriate tropospheric delay model, like the modified Hopfield model

(Masunari and Shimizu, 2007; Masunari et al., 2009; Shimizu et al., 2011, 2014; Nakashima et al., 2012b). In addition, the errors due to obstructions above the antennas can be reduced by an analysis performed without the data taken from the satellites moving behind the obstructions (Masunari et al., 2008; Shimizu, 2009; Shimizu et al., 2011, 2014). The random errors arising from random fluctuations can be removed by the application of an adequate method (Shimizu, 1999; Shimizu et al., 2014). These separated error-correction methods are also written in the ISRM Suggested Method for monitoring rock displacements using the Global Positioning System (GPS) (Shimizu et al., 2014) as suggestions for use with GPS monitoring. The question arises as to how the three separated error-correction methods can work together to improve the GPS measurement results, for example, when using GPS monitoring at a large-scale steep slope where the errors due to obstructions above the antennas and tropospheric delays occur at the same time. It is essential to apply a procedure with error-correction methods to enhance the accuracy of the measurement results for high precision monitoring when using GPS.

Another question is how to use the GPS measurement results for assessing the displacement behavior of a slope. On the other hand, the interpretation and the mechanism of the displacement behavior based on field measurements should be discussed.

In addition, the GPS sensors and the monitoring system are still expensive compared to standard geotechnical instruments (e.g., extensometers). In order to conduct GPS monitoring more effectively, sensors should be installed at many points and should be able to monitor the displacement at any interval. New sensors which can cope with these demands are desired. An investigation of the measurement performance with new GPS sensors should be conducted.

1.3. Objectives and scope of research

The research work presented in this dissertation is aimed at continuous displacement monitoring by using GPS and its application at a large-scale steep slope. In order to study and investigate the displacement evolution and its mechanism, long-term monitoring using GPS is conducted at the slope. In this research, a procedure with

error-correction methods to enhance the accuracy of the displacement monitored with GPS is proposed and validated to reduce and/or eliminate the bias errors from obstructions above the antennas and tropospheric delays at a large-scale steep slope for long-term monitoring. This study focuses on the baselines between a reference point and monitoring points which are less than one kilometer in length. After achieving the long-term monitoring displacements, numerical simulations are conducted to better understand the mechanism of the displacement behavior in considering field measurements and numerical simulations. Furthermore, the measurement performance of new GPS sensors is investigated using the kinematic method. The specific objectives of this research are as follows:

- Verification of the applicability of the error-correction methods for reducing the influence of obstructions above the antennas and tropospheric delays at a large-scale steep slope for long-term monitoring;

- Discussion on the mechanism of the occurrence of large displacements of the slope due to an increase in the groundwater level by a numerical analysis based on the monitoring results;

- Investigation of the measurement performance of new GPS sensors, developed inexpensively compared with the current sensor, which can be installed at many points and can monitor displacements at any interval.

1.4. Organization of dissertation

The dissertation is divided into six chapters. The flowchart of the dissertation is shown in Fig. 1.1. The content of each chapter is presented as follows:

Chapter 1 provides an introduction to the problem of slope failure, the background, the problem statement, the research objectives and scope of displacement monitoring for steep slopes, and the organization of the dissertation.

Chapter 2 presents a literature review of the conventional and the recent techniques for displacement monitoring. Furthermore, the application of GPS for displacement monitoring is reviewed together with an outline of GPS.

Chapter 3 investigates the applicability of the error-correction methods for reducing the effects of obstructions above the antennas and tropospheric delays when

using GPS for displacement monitoring at a large-scale steep slope. A procedure with error-correction methods to enhance the accuracy is proposed, and its applicability is verified for improving the GPS measurement results at a large-scale steep slope. Furthermore, the validity of the procedure is shown by a comparison between the displacement results by GPS and those by an extensometer and the Diffusion Laser Displacement Meter.

Chapter 4 shows the application of the GPS displacement monitoring system and the proposed procedure for long-term continuous monitoring at the large-scale steep slope. The interpretation of the displacement results is shown in plan views and vertical sections for assessing the time-evolution of the displacement behavior. Furthermore, the mechanism of the occurrence of large displacements at the slope due to the increase in the groundwater level was investigated by numerical simulations based on the displacement monitoring results.

Chapter 5 investigates the measurement performance of new GPS sensors using the kinematic method. Fundamental and field experiments are conducted to obtain the standard deviations of the new GPS sensors. The arithmetic average of the kinematic results is obtained when using the new GPS sensors.

Chapter 6 draws conclusions from the research presented within this dissertation and proposes recommendations for future research works.
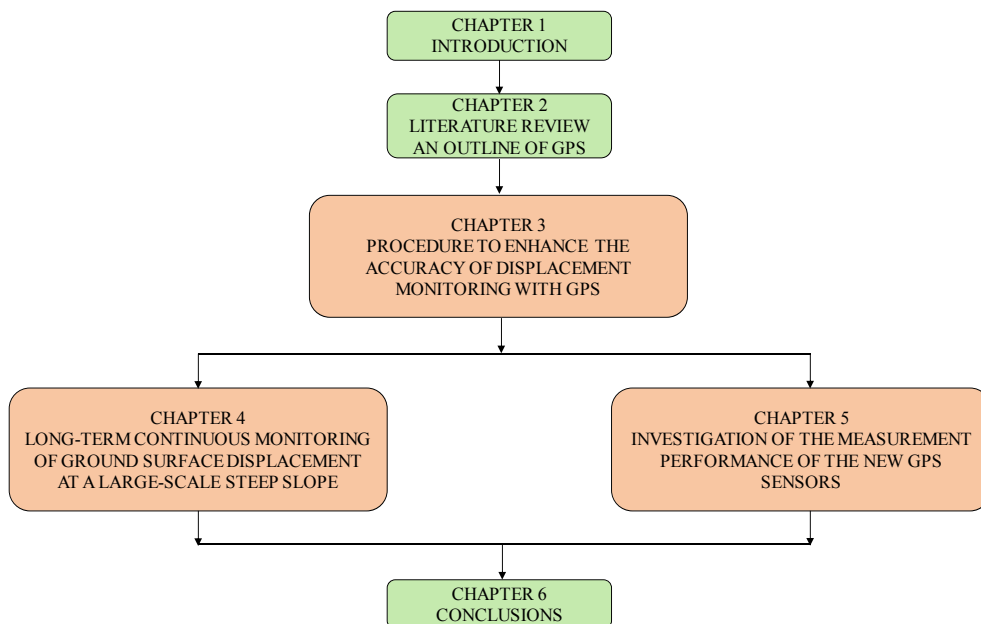
Fig. 1.1. Flowchart of the dissertation

Chapter 2

LITERATURE REVIEW AND OUTLINE OF GPS

Monitoring techniques are used to observe and analyze the displacements of slopes and the conditions that trigger them, and they provide information for designing countermeasures, etc. Hence, it would also be beneficial to understand the monitoring techniques. Herein, a literature review of the conventional and recent techniques for displacement monitoring are presented. Furthermore, a review of GPS applications for displacement monitoring is also presented together with an outline of GPS.

2.1. Literature review

2.1.1. Conventional and recent displacement monitoring techniques

There are various displacement monitoring techniques that can provide the evolution of slope displacement over time, the responses to triggering conditions, and useful information for designing countermeasures, etc. The monitoring techniques involve periodic and automatic measuring. The evolution of the displacement at a steep slope can be understood by using many types of sensors. Geotechnical engineers have the important task of determining which sensors will provide the best description of the deformation. Gili et al. (2000) summarized the main techniques for measuring surface displacements and their degrees of precision (Table 2.1).

Several types of monitoring techniques have been developed and applied to measure ground movements in unstable areas. Precision tape and wire devices have been applied to measure changes in the distance between points or crack walls (Dunnicliff, 1984; Gulla et al., 1988; Brückl et al., 2013). Inclinometers have been applied to detect the depth of shear movement. This depth is also the depth of the failure surface (Slope Indicator, 2011). Tiltmeters have been used to perform rapid and precise measurements (Wyllie and Mah, 2004). Ashkenazi et al. (1998) used levels, theodolites, Electronic Distance Meters (EDM), and a total station to measure coordinates and changes in targets, control points, and landslide features. Aerial and terrestrial photogrammetry are convenient tools that have been employed to make

contour maps and to find the cross sections and point coordinates of landslide areas. In addition, photogrammetric compilation has proven useful for analyzing the changes in slope morphology and for determining the movement vectors (Ballantyne et al., 1988; Chandler and Moore, 1989; Oka, 1998). The advantages of these conventional techniques are that they are able to obtain precise measurements. However, they only provide one-dimensional displacements and they can only be applied to measure local areas. In other words, these conventional techniques are not suitable for landslide covering in high-altitude mountainous zones or extensive areas. Furthermore, it is difficult to collect data automatically and continuously in real-time at large-scale steep slopes with these techniques.

Table 2.1. Overview of surface displacement measuring techniques and their precision (Gili et al., 2000).

Method	Results	Typical range	Typical precision
Precision tape	Δdistance	< 30 m	0.5 mm/ 30 m
Fixed wire extensometer	Δdistance	$< 10 - 80$ m	0.3 mm/30 m
Rod for crack opening	Δdistance	< 5 m	0.5 mm
Offsets from baseline	ΔH, ΔV	< 100 m	$0.5 - 3$ mm
Survey triangulation	ΔX, ΔY, ΔZ	$< 300 - 1000$ m	$5 - 10$ mm
Surveying traverses	ΔX, ΔY, ΔZ	Variable	$5 - 10$ mm
Geometrical leveling	ΔZ	Variable	$2 - 5$ mm/km
Precise geometrical leveling	ΔZ	Variable	$0.2 - 1$ mm/km
Electronic distance measurement	Δdistance	Variable (usual $1 - 14$ km)	$1 - 5$ mm $+ 1 - 5$ ppm
Terrestrial photogrammetry	ΔX, ΔY, ΔZ	Ideally < 100 m	20 mm from 100 m
Aerial photogrammetry	ΔX, ΔY, ΔZ	$H_{flight} < 500$ m	10 cm
Clinometer	$\Delta\alpha$	$\pm 10°$	$0.01 - 0.1°$
GPS	ΔX, ΔY, ΔZ	Variable (usual < 20 km)	$5 - 10$ mm $+ 1 - 2$ ppm

Recently, new technologies have been used to monitor slopes such as the Global Positioning System (GPS), Time Domain Reflectometry (TDR), the Diffusion Laser Displacement Meter (DLDM), and Synthetic Aperture Radar (SAR). With TDR, the depth to a shear plane or shear zone in a landslide can be located. However, TDR cannot determine the actual magnitude or direction of movement (Cortez et al., 2009). TDR can only detect the shear plane or shear zone. Moreover, if water infiltrates a

TDR cable, it will change the electrical properties of the coaxial cable. This may make it difficult to interpret the results.

The DLDM was developed by Naya et al. (2008, 2014) for monitoring rock/ground displacements. It can detect displacements of at least 1-2 mm for a baseline length of 62.5 m under rainfall intensities up to 120 mm/hr and displacements of at least 1-2 mm for a baseline length of 30 m even under rainfall intensities up to 200 mm/hr. The DLDM is similar to extensometers and inclinometers in that it can only observe the displacement in one-dimension.

Synthetic Aperture Radar (SAR) is a form of radar used to capture two- or three-dimensional images of objects. It can detect the displacement components along the sensor target line of sight (LOS) with high precision. The differential SAR interferometry (DInSAR) technique is employed for monitoring the small-scale movements on the surface. The accuracy of DInSAR is in the order of sub-centimeters. However, the drawbacks of DInSAR are geometric and temporal decorrelation, as well as atmospheric disturbances (Perissin and Wang, 2011).

2.1.2. *GPS application for displacement monitoring*

Conventional displacement monitoring techniques are limited to use in small areas and can measure only one-dimensional displacements. In addition, these conventional techniques are difficult and dangerous to install at large-scale steep slopes. The drawbacks of recent techniques, such as TDR, the DLDM, and DInSAR, are the inability to determine the actual magnitude and direction of movement, observing displacements in only one-dimension, and temporal decorrelation, respectively.

Nevertheless, the Global Positioning System (GPS), a displacement monitoring system, shows the potential to overcome the limitations of the above techniques. This research, therefore, employs the GPS technique for displacement monitoring.

GPS was established as a method for navigation and long baseline surveys (Hofmann-Wellenhof et al., 2001; Misra and Enge, 2011). It was first used for displacement monitoring in the mid-1980s in the fields of civil and mining engineering and other related fields (Burkholder, 1988, 1989; Chrzanowski and Wells, 1988).

Since then, many researchers have used GPS in practical applications (Stewart and Tsakiri, 1993; Behr and Hudnut, 1998; Gili et al., 2000; Malet et al., 2002; Kim et al., 2003; Taşçi, 2008), and preliminary guidelines have been published for displacement (deformation) monitoring (US Army Corps of Engineers, 2002; Vermeer, 2002; Bond, 2004).

Recently, GPS techniques have been widely used to monitor the ground (Ma et al., 2012), slopes (Shimizu and Nakashima, 2017), and dams (Nakashima et al., 2012a), etc. Some studies have used GPS for displacement monitoring and have compared the results from conventional techniques, such as theodolite, electronic distance measurement, levels, total station, inclinometers, and wire extensometers (Gili et al., 2000; Moss, 2000; Malet et al., 2002; Rizzo, 2002; Coe et al., 2003; Tagliavini et al., 2007; Bertacchini et al., 2009; Calcaterra et al., 2012). Other studies have combined GPS and other surveying techniques, for example, terrestrial laser scanning, SAR interferometry, CR-InSAR, and photogrammetry for landslide investigations (Mora et al., 2003; Rott and Nagler, 2006; Peyret et al., 2008; Yin et al., 2010; Wang, 2011; Zhu et al., 2014). These integrations have provided useful information on displacements, magnitude, direction, evolution, etc. Based on the above studies, it is now recognized that the GPS monitoring system can provide three-dimensional displacements with mm accuracy over extensive areas.

Furthermore, the GPS displacement monitoring system can be classified by a number of factors, namely, automation, enhancement accuracy, etc. (Szostak-Chrzanowski and Chrzanowski, 2008). Based on the scope of this research, those factors related to displacement monitoring using GPS are reviewed.

2.1.2.1. Monitoring campaign and data acquisition

GPS displacement monitoring has been performed by both periodic (Rawat et al., 2011; Wang, 2012) and continuous (Masunari et al., 2003; Wang et al., 2012; Xiao et al., 2012) monitoring campaigns. The choice of a particular monitoring campaign depends on the critical factors of accuracy, cost, and safety of the equipment, etc.

On the other hand, in the standard method for monitoring displacements with GPS, it is required that a survey team revisit the monitoring site at regular intervals, for example, every few weeks or months. The static, rapid static or real-time kinematic

GPS surveying techniques can be used to construct a time series of the displacements observed at the monitoring points.

The main advantage of the standard method is that it requires a lower initial cost. One set of GPS equipment can be used to monitor several locations of a slope. Furthermore, the GPS equipment can also be used for other surveying purposes when it is not being used for displacement monitoring.

However, there are some disadvantages in using the standard method. The lower precision and poorly represented samples from the time series are two main disadvantages of this method. In this method, ground marks are used as monumentations. Setup errors can also occur in this method. It is often required that many points be observed in a short period of monitoring time. The coordinate precision is low as a result of the short observation times. Furthermore, the discontinuous time series is another disadvantage. The short period observations are often not enough to adequately grasp the trend of the displacement.

When standard receivers are employed for monitoring displacements, the GPS data are downloaded manually from the receivers. Then, data processing is conducted to obtain the coordinates of the monitoring points and to calculate the displacements for each session. This is inconvenient and ineffective for continuous monitoring.

To overcome the above limitations of the standard method, an automatic monitoring system that was previously developed (Shimizu and Matsuda, 2002; Iwasaki et al., 2003; Masunari et al., 2003) is employed in this study. The automatic monitoring system requires the following items (Iwasaki et al., 2003):

- System stability for long-term monitoring
- High accuracy of the measurements
- Quick data acquisition, analysis, and evaluation for many slopes at once
- Rapid notification of the monitoring results to the clients
- Low cost

2.1.2.2. GPS processing methods

GPS displacement monitoring systems are classified based on how the system processes, utilizes, and handles the GPS observation data. The first method is post-processing in which all the observations are processed by means of the least squares

method to obtain a set of coordinates. Then, some software packages are used to perform the displacement analysis. One of examples of this post-processing method is Leica GEOMoS (Leica Geosystems, 2009). This method has a small delay in the early detection of failure.

The second method utilizes position solutions by a real-time kinematic (RTK) mode to perform the displacement analysis (Shimizu et al., 1996, 1997). Another example of this processing method is used in the GOCA system (Kälber and Jäger, 2001; Jäger and González, 2006). The third method involves the simultaneous transmission of the raw data that have been acquired at all the GPS stations to the server computer. Then, the calculations are performed. GRAZIA (Gassner et al., 2002) is software that follows this approach.

The goal of this research is to conduct continuous displacement monitoring by GPS and to describe its application at a large-scale steep slope. A system that consists of GPS sensors, data-links between them, and a server computer, etc. was developed (Shimizu and Matsuda, 2002; Iwasaki et al., 2003; Masunari et al., 2003). An outline of the system will be given in Chapter 3.

2.1.2.3. Accuracy of monitoring systems

Accuracy plays an important role in any displacement monitoring system (Brown et al., 2006). To achieve displacement monitoring with high precision, many studies have been made on the modeling components of the GPS measurement results, such as models for tropospheric delays (Saastamoinen, 1972; Niell, 1996), etc. On the other hand, tropospheric delays, one of the bias errors, are obtained by using average parameters from numerical weather predictions together with time and approximate coordinates (Leandro et al., 2006; Lagler et al., 2013). Unfortunately, the wet delay component in the tropospheric delays depends on the water vapor content. The water vapor changes over time and space. Therefore, the above models are insufficient for achieving monitoring with high precision.

A correction method using the modified Hopfield model together with meteorological conditions observed at the monitoring site was proposed for correcting tropospheric delays (Masunari and Shimizu, 2007; Masunari et al., 2009; Shimizu et

al., 2011, 2014; Nakashima et al., 2012b). This correction method was proven effective for improving the measurement accuracy.

Another source of bias errors is caused by obstructions above antennas (Shimizu et al., 2014). Furthermore, the number of satellites that are observed by the receiver also affects the measurement accuracy (Koo et al., 2017). The analysis of data without the data from the satellites moving behind the obstructions is effective for reducing these errors and for improving the accuracy (Masunari et al., 2008; Shimizu, 2009; Shimizu et al., 2011, 2014).

Furthermore, it is recommended that random errors, caused by random fluctuations, be reduced by an adequate method (Shimizu et al., 2014). A trend model can yield good estimates from the original measurement results (Shimizu, 1999; Shimizu et al., 2014).

In order to achieve monitoring with high precision, especially at large-scale steep slopes where there are simultaneously obstructions above the antennas and a difference in height between the reference point and the monitoring points, a procedure with error-correction methods to enhance the measurement accuracy is proposed in this research for improving the measurement results. The detailed procedure is shown in Chapter 3.

2.1.2.4. Costs of monitoring schemes

GPS is now recognized as useful technology for monitoring extensive areas and large structures. It has the potential to measure three-dimensional displacements with mm accuracy for baseline lengths of less than 1 km. In order to conduct GPS monitoring more effectively, a sensor should be installed at many points and should be able to monitor displacement at any interval. Unfortunately, if GPS receivers are employed to monitor a huge area, such as dams and landslides, the investment costs are very high. In recent years, many researchers have been working on low-cost GPS receivers in an attempt to find a more economical solution to displacement monitoring using GPS. In particular, some studies have investigated the accuracy of low-cost single-frequency GPS receivers (Janssen and Rizos, 2003; Squarzoni et al., 2005). Other studies have also used low-cost GPS receivers in post-processing (Dabove et al., 2014; Cina and Piras, 2015), in near real-time (Eyo et al., 2014), and in real-time

approaches to monitoring landslide behavior. Furthermore, Zhang and Schwieger (2017) investigated the performance of the L1-optimized choke ring ground plane for a low-cost GPS receiver system. The performance of low-cost GPS receivers has also been investigated through the use of free and open source software, such as RTKLIB (Takasu and Yasuda, 2009; Bellone et al., 2014; Biagi et al., 2015, 2016) and goGPS (Biagi et al., 2015, 2016). Schrader et al. (2016) combined multiple consumer-grade GPS receivers to present an inexpensive way to achieve a better GPS performance. In addition, an automatic low-cost GPS monitoring system using WLAN communication has been introduced (Günther et al., 2008; Zhang et al., 2012). These studies show that low-cost GPS receivers have the potential to provide centimeter or sub-centimeter accuracy.

In the research within this dissertation, the measurement performance of new GPS sensors, being developed by a collaboration of the Shimizu Lab. (Yamaguchi University) and a manufacturer, is also investigated by experiments and field experiments using the kinematic method.

2.2. Outline of GPS

2.2.1. GPS segments
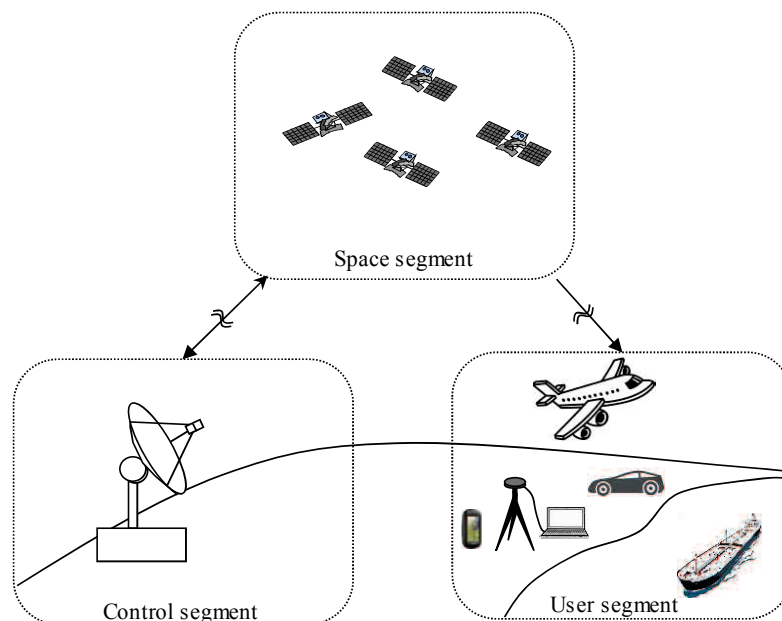
Fig. 2.1. GPS segments (adapted from Shimizu et al., 2014).

The Global Positioning System (GPS) is a satellite-based positioning system. There are three different segments in the GPS, namely, the space segment, the control segment, and the user segment (Fig. 2.1). The space segment provides global coverage with observable satellites above elevations of 15º (Hofmann-Wellenhof et al., 2001). The satellites move in nearly circular orbits with an altitude of approximately 20200 km above the earth in a period of about 12 sidereal hours. The constellation currently contains 31 of these satellites. A platform for radio transceivers, atomic clocks, computers, and various ancillary equipment is provided by the GPS satellites to operate the system. Atomic clocks precisely control all the signal components to achieve the system's accuracy.

The control segment comprises a master control station, worldwide monitor stations, and ground control stations. The control segment tracks the satellites for the orbit, clock determination, prediction modeling, time synchronization of the satellites, and upload of the data message to the satellites. The user segment consists of the user equipment for either the military or civilians. The receivers are characterized by the observables (i.e., code pseudoranges or carrier phase) and the codes (i.e., C/A-code or P-code). The signals are provided by the satellites which track them simultaneously.

2.2.2. *GPS observables*

The GPS observables are differential ranges from the measured time or phase between the received signals and receiver-generated signals. The position of the user receiver can be obtained by determining the distances (ranges) from it to the satellites. These distances can be calculated with code pseudoranges or the carrier phase. Satellites and receiver clocks are used for the calculations. Doppler observations are not used in this dissertation. Hence, they are not mentioned any further.

2.2.2.1. *Code pseudoranges*

The code range method is used to measure the amount of time shift required to align the C/A-code replica, generated at the receivers, with the signals received from the satellites (Misra and Enge, 2011). Then, the time is multiplied by the speed of light in a vacuum to compute the distance. Since the satellite and the receiver clocks are not

synchronized, a small delay needs to be added to the time on the receiver clock (clock bias) (Fig. 2.2). At least four satellites are used to determine the four unknowns, *X, Y, Z*, and the receiver clock delay. Eq. (2.1) shows the equations used to obtain the coordinates of an observed point. The precision of this procedure is low due to the large distance between the satellites and the antennas. Hence, it is not suitable for high-precision surveying such as that required for landslide monitoring.

$$\rho_1 = \sqrt{(X - x_1)^2 + (Y - y_1)^2 + (Z - z_1)^2} = c(\Delta t_1 + \delta_t)$$
$$\rho_2 = \sqrt{(X - x_2)^2 + (Y - y_2)^2 + (Z - z_2)^2} = c(\Delta t_2 + \delta_t)$$
$$\rho_3 = \sqrt{(X - x_3)^2 + (Y - y_3)^2 + (Z - z_3)^2} = c(\Delta t_3 + \delta_t) \qquad (2.1)$$
$$\rho_4 = \sqrt{(X - x_4)^2 + (Y - y_4)^2 + (Z - z_4)^2} = c(\Delta t_4 + \delta_t)$$

where: Δt_i: measured travel times of the codes from four satellites;

ρ: measured code pseudoranges between the receiver and the satellites;

c: speed of light in a vacuum 2.99792458 x 10^8 m/s;

δ_t: unknown clock bias;

x_i, y_i, z_i: coordinates of the satellites from the navigation message transmitted from the satellites.

X, Y, Z: unknown coordinates of the receiver point.
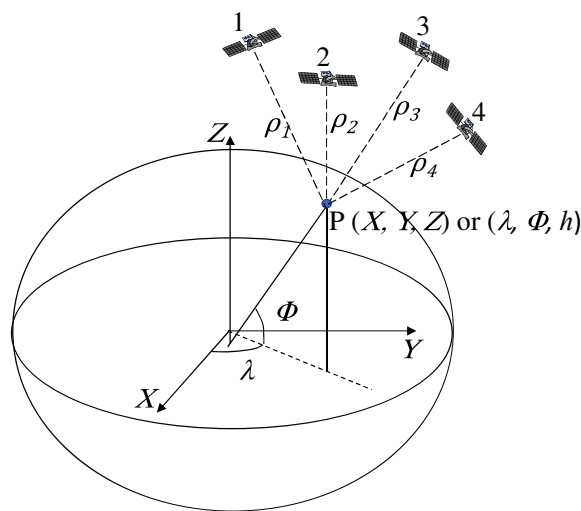
Fig. 2.2. GPS observation of a point based on code pseudoranges: λ, Φ, and *h* are longitude, latitude, and height of the point above the reference ellipsoid; *X, Y,* and *Z* are the global geocentric Cartersian coordinates.

16

2.2.2.2. Phase pseudoranges
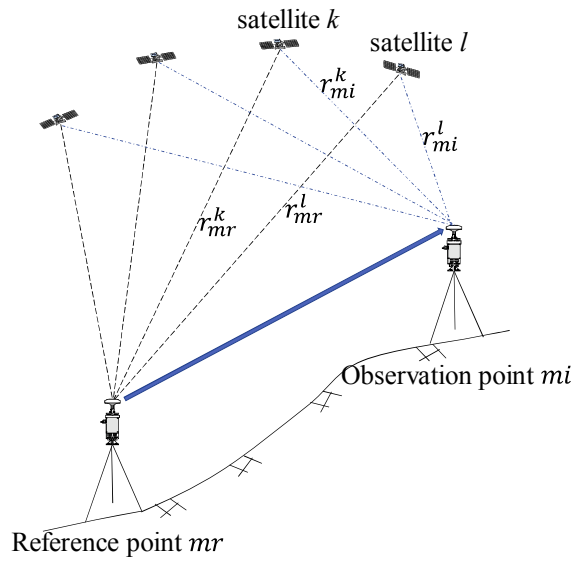
Fig. 2.3. Schematic of GPS carrier phase measurement.

In contrast, much more precise measurements can be achieved with millimeter accuracy by carrier phase measurements. The carrier phase method measures the phase difference between the carrier signal, generated by the receiver, and the carrier received from a satellite (Misra and Enge, 2011). Fig. 2.3 shows a schematic of the GPS carrier phase measurement. However, the carrier phase measurement remains fixed at a fraction of a cycle. The distance between the receiver and a satellite can be calculated by an unknown number of whole cycles plus the measured fractional cycle. This result is referred to as integer ambiguity. Complicated algorithms are required to achieve the solution (single, double, and triple differencing).

Methods to correct the various errors (i.e., tropospheric delays and ionospheric delays) and to resolve the integer ambiguities are applied to obtain accurate position estimates. Eq. (2.2) shows the basic equation including errors.

$$\phi_{mi}^k = \frac{r_{mi}^k + I_{\phi mi}^k + T_{\phi mi}^k}{\lambda} + \frac{c(\delta t_{mi} + \delta t^k)}{\lambda} + N_{mi}^k + \varepsilon_{\phi mi}^k \qquad (2.2)$$

where:

- ϕ_{mi}^k: signal phase from satellite k to observation point mi;

17

- r_{mi}^k: distance from satellite k to observation point mi;

- $I_{\phi_{mi}}^k$: ionospheric delay (error) of signal phase from satellite k to observation point mi;

- $T_{\phi_{mi}}^k$: tropospheric delay (error) of signal phase from satellite k to observation point mi;

- c: speed of light in a vacuum 2.99792458×10^8 m/s;

- δt_{mi}: receiver mi clock bias (error);

- δt^k: satellite k clock bias (error);

- λ: wavelength of the signal;

- N_{mi}^k: unknown integer ambiguity from satellite k to observation point mi;

- $\varepsilon_{\phi_{mi}}^k$: observation error of signal phase from satellite k to observation point mi.

The single-phase difference between observation point mi and reference point mr for satellite k, $\phi_{mi}^k - \phi_{mr}^k$, is calculated. Similarly, the single-phase difference for satellite l, $\phi_{mi}^l - \phi_{mr}^l$, is also calculated. The double-phase difference, $(\phi_{mi}^k - \phi_{mr}^k) - (\phi_{mi}^l - \phi_{mr}^l)$, is obtained as follows:

$$\phi_{mi-mr}^{k-l} = \frac{r_{mi-mr}^{k-l}}{\lambda} + N_{mi-mr}^{k-l} + \varepsilon_{\phi_{mi-mr}}^{k-l} + \frac{T_{\phi_{mi-mr}}^{k-l}}{\lambda} \qquad (2.3)$$

Eq. (2.3) shows the fundamental equation for relative positioning. The biases of the receiver clock and the satellite clock are eliminated by using the double-phase difference process. Furthermore, when the baseline length between the observation point and the reference point is short, less than a few km in length, the ionospheric delay is also eliminated (Shimizu et al., 2014). The tropospheric delay remains when the height difference between the observation point and the reference point is a few tens of meters.

The double-phase difference is calculated from the observed phase by a GPS receiver. Then, the three-dimensional coordinates of the observation point and integer ambiguity, r_{mi-mr}^{k-l} and N_{mi-mr}^{k-l}, are determined by means of the least squares method for the residual, $\varepsilon_{\phi_{mi-mr}}^{k-l}$.

2.2.3.   Coordinate systems

The position of a receiver can be expressed in a coordinate system that is fixed to the earth and moves with it (Misra and Enge, 2011). Based on the scope, this subsection presents an outline of the World Geodetic System of 1984 (WGS84) that is widely used around the world. The study site in this research is located in Yamaguchi Prefecture, Japan. Therefore, in order to obtain the displacements, the conversion from WGS84 to the local coordinate system, Transverse Mercator (Japan zone 3), is also conducted.

2.2.3.1. World Geodetic System 1984 (WGS84)

WGS84 is a 3-D, earth-centered reference system that was developed by the Defense Mapping Agency of the U.S. (Fig. 2.4), Department of Defense (DoD) (Misra and Enge, 2011). It is the official reference system for all mapping, charting, navigation, and geodetic products to be used throughout the DoD. WGS84 includes a coherent set of global models and definitions:

- An earth-centered, earth-fixed Cartesian coordinate frame
- An ellipsoid of revolution as a geometric model of the shape of the earth
- A characterization of the earth's gravity field and geoid
- A consistent set of fundamental constants
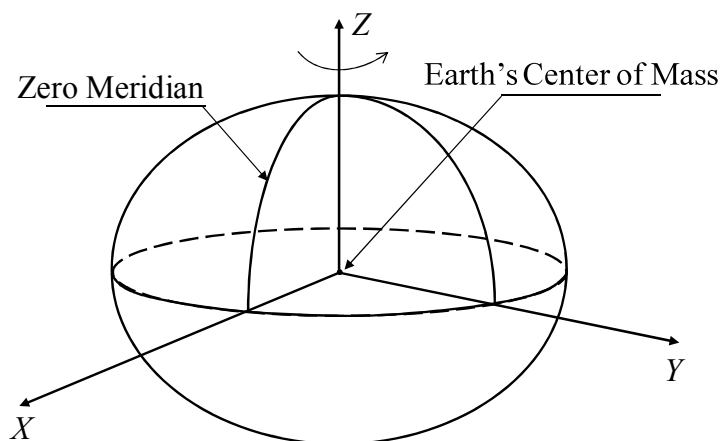
Fig. 2.4. WGS84 reference frame (adapted from Misra and Enge, 2011).

19

Table 2.2. WGS84 fundamental parameters (Misra and Enge, 2011).

Parameter	Value
Ellipsoid	
Semi-major axis (a)	6378137.0 m
Reciprocal flattening ($1/f$)	298.25223563
Earth's angular velocity (ω)	7292115.0 x 10^{-11} rad/sec
Earth's gravitational constant (GM)	3986004.418 x 10^8 m^3/s^2
Speed of light in a vacuum (c)	2.99792458 x 10^8 m/s

The user will refer to the position of a point in WGS84 as WGS84 *LLA* (for latitude, longitude, and altitude), or WGS84 *XYZ* coordinates. The positions of the GPS satellites are expressed in WGS84. The receiver positions, therefore, are obtained as WGS84 coordinates. The WGS84 is defined by fundamental parameters (Misra and Enge, 2011), as shown in Table 2.2.

2.2.3.2. Transverse Mercator projection

Transverse Mercator projection, known as Gauss-Krüger projection, is based on projecting the points on the ellipsoidal surface mathematically onto an imaginary transverse cylinder (El-Rabbany, 2002). The cylinder can be either a tangent or a secant to the ellipsoid (Fig. 2.5).
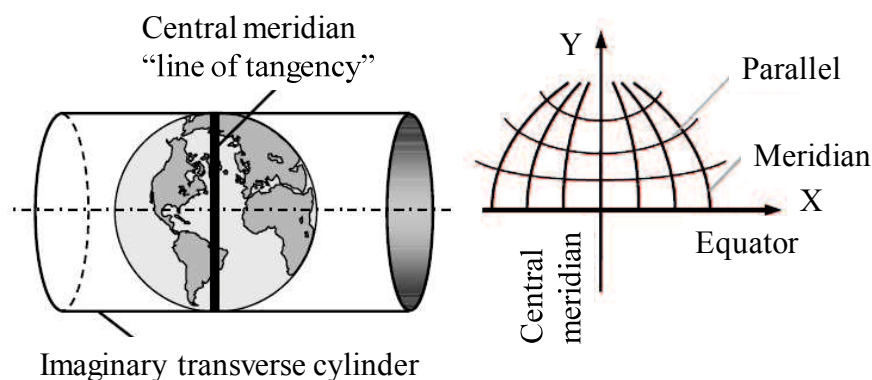
Fig. 2.5. Transverse Mercator map projection (El-Rabbany, 2002).

In Japan, the Japanese Geodetic Datum 2000 (JGD2000) was introduced as the geodetic reference system (Geographical Survey Institute, 2004). The monitoring site

in this research is located in Yamaguchi Prefecture, Japan where the origin of zone 3 in the JGD2000 is selected. To convert the coordinates from WGS84 to Transverse Mercator, Gauss-Krüger, the following equations are employed (Tyuji, 1979):

$$\frac{X}{m_0} = B + (\Delta\lambda)^2 \frac{N}{2} sin\varphi cos\varphi + (\Delta\lambda)^4 \frac{N}{24} sin\varphi cos^3\varphi(5 -$$

$$t^2 + 9\eta^2 + 4\eta^4) + (\Delta\lambda)^6 \frac{N}{720} sin\varphi cos^5\varphi(61 - 58t^2 + t^4) \qquad (2.4)$$

$$\frac{Y}{m_0} = \Delta\lambda N cos\varphi + (\Delta\lambda)^3 \frac{N}{6} cos^3\varphi(1 - t^2 + \eta^2)$$

$$+ (\Delta\lambda)^5 \frac{N}{120} cos^5\varphi(5 - 18t^2 + t^4) \qquad (2.5)$$

where:

X, Y: Northing, Easting

φ, λ: latitude, longitude of a measured point

$m_0 = 0.9999$: scale factor

Latitude of origin, φ_0: 36.0

Central meridian, λ_0: 132.166666666667

Semi-major axis, a: 6378137.0

Semi-minor axis, b: 6356752.314140356

Inverse flattening, f: 298.257222101

$$N = \frac{a}{(1-e^2 sin^2\varphi)^{1/2}} \qquad (2.6)$$

$$e = f(2 - f) \qquad (2.7)$$

$$t = tan\varphi \qquad (2.8)$$

$$e' = \frac{(a^2-b^2)^{1/2}}{b} \qquad (2.9)$$

$$\eta = e' cos\varphi \qquad (2.10)$$

$$B = Md\varphi = a(1 - e^2) \int_{\varphi_1}^{\varphi_2}(1 - e^2 sin^2\varphi)^{-3/2}d\varphi \qquad (2.11)$$

(B: Meridian arc length).

2.3. Chapter summary

In this chapter, conventional and recent monitoring techniques were reviewed. A literature review of GPS application for displacement monitoring was shown. The following conclusions can be drawn:

(1) Conventional monitoring techniques, such as surface extensometers, inclinometers, and tiltmeters, are limited to use in small areas and can measure only one-dimensional displacement. In addition, these conventional techniques are difficult and dangerous to install at large-scale steep slopes.

(2) Recent monitoring techniques, TDR, the DLDM, and DInSAR, also have some drawbacks. The TDR techniques cannot determine the actual magnitude or direction of movement. The DLDM has the disadvantage of taking observations of the displacement in only one-dimension. The photogrammetric technique is affected by weather and seasonal conditions. DInSAR has drawbacks in geometric and temporal decorrelation.

(3) The GPS displacement monitoring system shows the potential to overcome the limitations of the above techniques. The GPS system can continuously monitor three-dimensional displacements in real time over extensive areas. Hence, this research employs the GPS displacement monitoring system.

Chapter 3

PROCEDURE TO ENHANCE THE ACCURACY OF DISPLACEMENT MONITORING WITH GPS

3.1. Introduction

GPS has the potential to measure three-dimensional displacements with mm accuracy for baseline lengths of less than 1 km. On the other hand, GPS measurement results are generally scattered due to various error sources. To guarantee the reliability of the measurement results, some appropriate methods should be applied to reduce and/or eliminate the errors included in the measurement results. In this chapter, a procedure with error-correction methods is proposed to enhance the accuracy of GPS measurement results. The applicability of the procedure is verified through its practical application at a large-scale steep slope. Furthermore, the validity of the procedure is shown in comparison to the results obtained by standard extensometers and the Diffusion Laser Displacement Meter (DLDM) to investigate the performance. This study focuses on baselines (distances between the reference point and monitoring points) which are less than 1 km in length.

3.2. Outline of the system

A GPS displacement monitoring system using the L1 signal (frequency: 1575.42 MHz and wavelength: 19.029 cm) was developed, as illustrated in Fig. 3.1 (Shimizu and Matsuda, 2002; Iwasaki et al., 2003; Masunari et al., 2003). Sensors, composed of an antenna and a terminal box, are set on monitoring points and a reference point. A control box that contains a computer, a data memory, and a network device is connected to the sensors. The sensors receive the data emitted from the satellites and then transfer the data to the control box through cables. The server computer, located in an office away from the monitoring area, automatically controls the entire system to acquire the data from the control box and to analyze them. Then, three-dimensional displacements are obtained for all the monitoring points. The monitoring results are

given to users on the web in real-time. The users only need to access the home page to see the monitoring results.
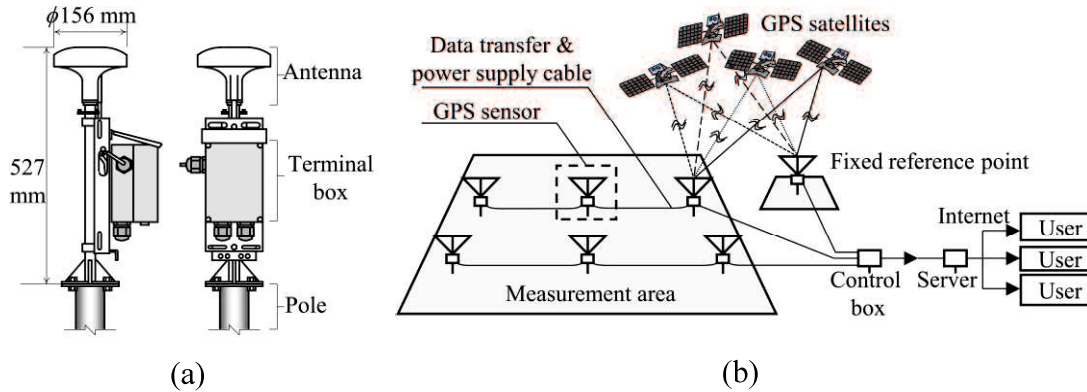
Fig. 3.1. Schematic diagram of GPS displacement monitoring system (adapted from Nakashima et al., 2012b): (a) Sensor and (b) Monitoring system (Shimizu and Matsuda, 2002; Iwasaki et al., 2003; Masunari et al., 2003).

The system employs the static method, which is one method of relative positioning in GPS surveys (Hofmann-Wellenhof et al., 2001; Misra and Enge, 2011). The sensors observe signals (code and phase signals corresponding to all the available GPS satellites) every 30 seconds, a baseline analysis is conducted using one-hour data, and the displacements are monitored every hour. The software, Capwin ver. 3.50, is used for the GPS baseline static processing (Masunari et al., 2003). The present research employed the above GPS system.

3.3. Error sources and correction methods

3.3.1. General concept

GPS measurement results generally include random errors and bias errors. Random errors are brought about by random fluctuations in the measurements. These errors are caused by receiver noise, an operating limit of the receiver (resolution), and other accidental errors. Typical bias errors, on the other hand, are tropospheric delays and other signal disturbances caused by obstructions above the antennas. Since both random and bias errors influence the monitoring quality, they should be corrected by appropriate methods which can reduce and/or eliminate them.

Measurement value y can be expressed by exact value u_0, bias errors ε_p and ε_T, and random error ε_R, as follows (Shimizu et al., 2014):

$$y = u_0 + \varepsilon_p + \varepsilon_T + \varepsilon_R \tag{3.1}$$

where ε_p is an error due to a signal disturbance caused by an obstruction above an antenna, ε_T is an error due to a tropospheric delay, and ε_R is a random error due to receiver noise, etc. Tropospheric delays occur as the refraction of signals from the satellite in the atmosphere due to meteorological conditions (Hofmann-Wellenhof et al., 2001; Misra and Enge, 2011). In this study, a procedure with error-correction methods to enhance the accuracy of the displacement monitored with GPS is proposed and validated to reduce and/or eliminate both bias errors ε_p and ε_T. After removing the bias errors from the measurement values, a stochastic time-series filtering method, namely, *the trend model*, is applied to estimate the exact displacements.

3.3.2. Reduction of signal disturbances due to obstructions above antennas

Obstructions above an antenna may block the antenna signal reception and cause disturbances to the signals; these overhead obstructions become error sources in GPS displacement monitoring. For example, landslide areas are often located among mountainous slopes where the signals from satellites are disturbed by trees and vegetation above one or more of the antennas. Although the antennas ideally should be located in areas with a sufficiently open sky, this is often difficult in practical applications due to the limited amount of open space. When there are unavoidable obstructions above certain antennas, only the data without the signals transmitted from the satellites behind the obstructions are used for analyses (Shimizu et al., 2014). This is called mask processing.

3.3.3. Correction of tropospheric delays due to meteorological conditions

When signals propagate through the troposphere, tropospheric delays may occur as a result of refractive effects due to air density. Air density is a function of the

pressure of dry gases and water vapor. This means that meteorological conditions may influence the measurement results. It is well known that tropospheric delays largely affect the measurement results of GPS.

In order to correct the tropospheric delay effects, an appropriate model, like the modified Hopfield model, the Saastamoinen model, etc., is employed in the baseline analysis (Hofmann-Wellenhof et al., 2001; Misra and Enge, 2011). Usually, the standard atmospheric parameters (e.g., atmospheric pressure of 1013.25 hPa, temperature of 18° Celsius, and humidity of 50%) are used as default values to correct tropospheric delays (Dach et al., 2015).

However, it is known that the above procedure is not sufficient for correcting tropospheric delays for precise displacement monitoring. In particular, when the difference in height between a measurement point and the reference point is large, the amount of errors cannot be ignored. In this study, the modified Hopfield model is employed to estimate the tropospheric delays.

Tropospheric delays are estimated by the following equation:

$$\Delta R^{Trop} = 10^{-6} \int N^{Trop} ds \qquad (3.2)$$

where N^{Trop} is the refractivity.

Hopfield (1969) showed the possibility of separating N^{Trop} into dry and wet components. The results of the dry part are from the dry atmosphere, while those of the wet part are from water vapor. Eq. (3.2) becomes

$$\Delta R^{Trop} = 10^{-6} \int N_d^{Trop} ds + 10^{-6} \int N_w^{Trop} ds \qquad (3.3)$$

Using real data covering the whole earth, Hopfield empirically presented the refractivity of the dry component as a function of height h above the surface.

$$N_d^{Trop} = N_{d,0}^{Trop} (\frac{h_d - h}{h_d})^4 \qquad (3.4)$$

where the height of dry component h_d is assumed to be

$$h_d = 40136 + 148.72(T - 273.16) \qquad [m] \qquad (3.5)$$

where T is the absolute temperature. Similarly, the refractivity of the wet component is assumed to be

$$N_w^{Trop} = N_{w,0}^{Trop} (\frac{h_w - h}{h_w})^4 \qquad (3.6)$$

where the average value, $h_w = 11000$ [m], is used as the height of the wet part.

Models for dry and wet refractivity at the earth's surface have been used. The

corresponding dry and wet components are as follows:

$$N_{d,0}^{Trop} = 77.64 \frac{p}{T} \tag{3.7}$$

$$N_{w,0}^{Trop} = -12.96 \frac{e}{T} + 3.718 \times 10^5 \frac{e}{T^2} \tag{3.8}$$

where p is the atmospheric pressure and e is the partial pressure of the water vapor, namely,

$$e = 6.112 \left(\frac{RH}{100}\right) exp(\frac{17.62T - 4813}{T - 30.03}) \tag{3.9}$$

where RH is the humidity (%).

In order to estimate the tropospheric delays by the above model, the meteorological data along the signal path in the atmosphere are generally required. However, in cases where the baseline length is less than 1 km, like in this study, the delays above the sensor at higher positions can be eliminated in the process of the baseline analysis and only the delays between the reference and the monitoring points need to be estimated. Therefore, the atmospheric pressure, temperature, and humidity are measured near the ground surface.

3.3.4. *Estimation of exact values from measured results with random errors*

After removing bias errors ε_p and ε_T by the above procedure, Eq. (3.1) can be rewritten as follows:

$$y' = y - (\varepsilon_p + \varepsilon_T) = u_0 + \varepsilon_R \tag{3.10}$$

In order to estimate the exact value for u_0 from the corrected measurement result y' with random errors, the *trend model* (Kitagawa and Gersch, 1984; Kitagawa, 1993) is applied (Shimizu, 1999; Shimizu and Matsuda, 2002). This model is composed of an observation equation and a system equation, as follows:

$$y'_n = u_n + \varepsilon_{Rn} \text{ (observation equation)}$$
$$\Delta^k u_n = v_n \text{ (system equation)} \tag{3.11}$$

where u_n indicates the estimates for the exact values of the displacements and y'_n represents the corrected measurement results. The measurement interval is D_t and subscript n denotes progressing time t ($t = nD_t$). Δ is the operator for the finite difference ($\Delta u_n = u_n - u_{n-1}$) and Δ^k means the rank "k" difference. The observation equation is a kind of probability finite difference equation for rank k. v_n is the white noise with an average value of 0 and standard deviation τ. ε_{Rn} is the observation error with standard deviation σ.

3.4. Application of the procedure with the error-correction methods

3.4.1. Monitoring site

The procedure with error-correction methods, described in section 3.3, is applied to the results of GPS monitoring conducted for one month at the large-scale steep slope shown in Fig. 3.2.

The site where the system was installed is a large-scale steep slope along a national route in Yamaguchi Prefecture, Japan (Fig. 3.2). The slope is composed primarily of rhyolite and granite which formed in the Cretaceous period, Mesozoic era, and its surface is partially covered with a colluvial deposit. The vegetation extends over the slope and creates an obstruction above the antennas. In July 1972, the slope collapsed in large areas, deposits flowed, and a railroad and a national road were damaged. In 2010, due to heavy rainfall, failure with a volume of 1600 m^3 was recorded. Similarly, another failure was also recorded in 2011 after heavy rainfall. A check dam was constructed to collect deposits from the top of the slope, and a rock-shed tunnel was built to protect the road.

GPS sensors were first set at reference point K1 and monitoring points G1 and G2, and then later at G3 and G4, as shown in Figs 3.2 and 3.3. The sensors were firmly fixed at the monitoring points on the ground surface by a tripod/pillar and anchors. The displacement of each monitoring point is assumed to coincide with one of the sensors. A plan view of the monitoring area and the vertical sections are shown in Fig. 3.4. The height differences between monitoring points G1, G2, G3, and G4 and

reference point K1 are 103 m, 112 m, 103 m, and 94 m, respectively. BV5 is the location of the borehole which was used to monitor the groundwater level in the ground.
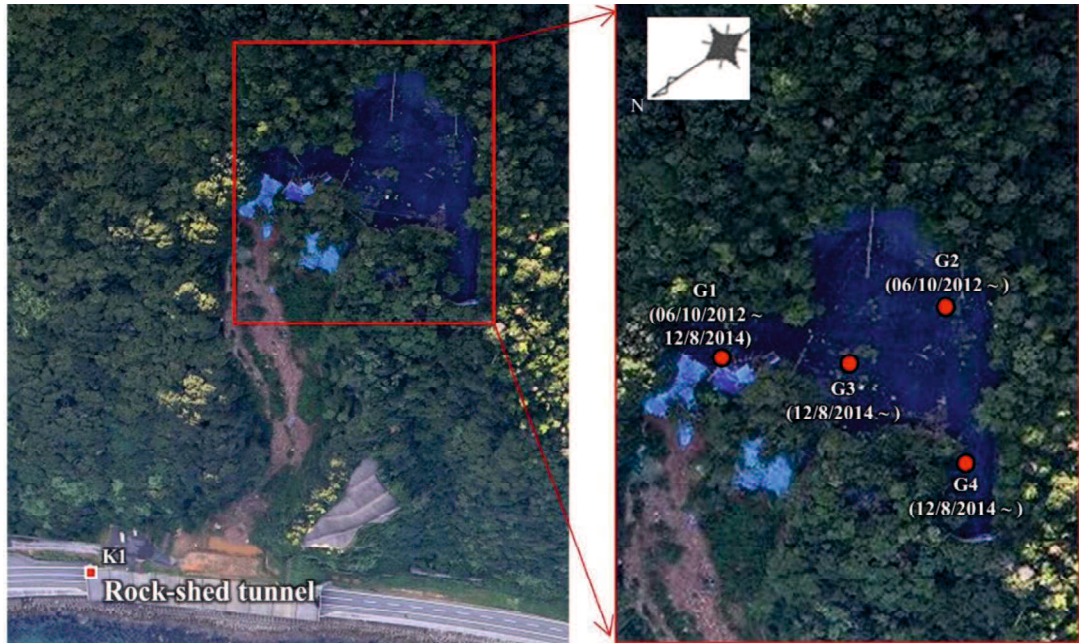
Fig. 3.2. Monitoring site and locations of GPS sensors (the dates below the GPS points indicate the monitoring period of the equivalent monitoring points).
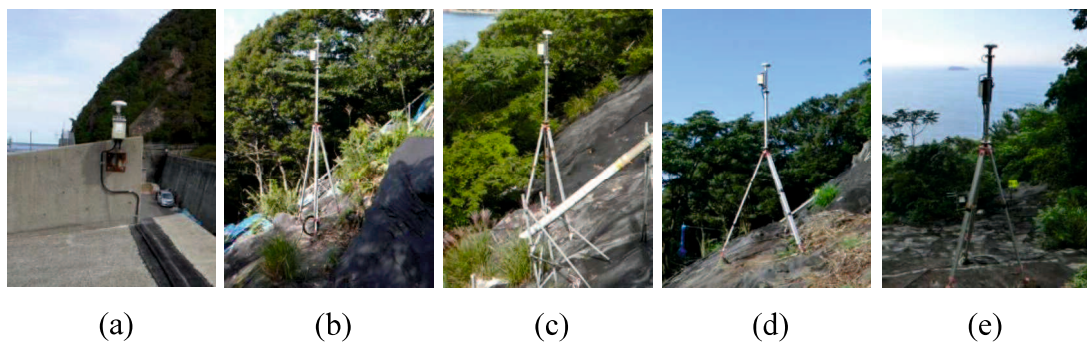
Fig. 3.3. Reference point K1 (a) and monitoring points G1 (b), G2 (c), G3 (d), and G4 (e).
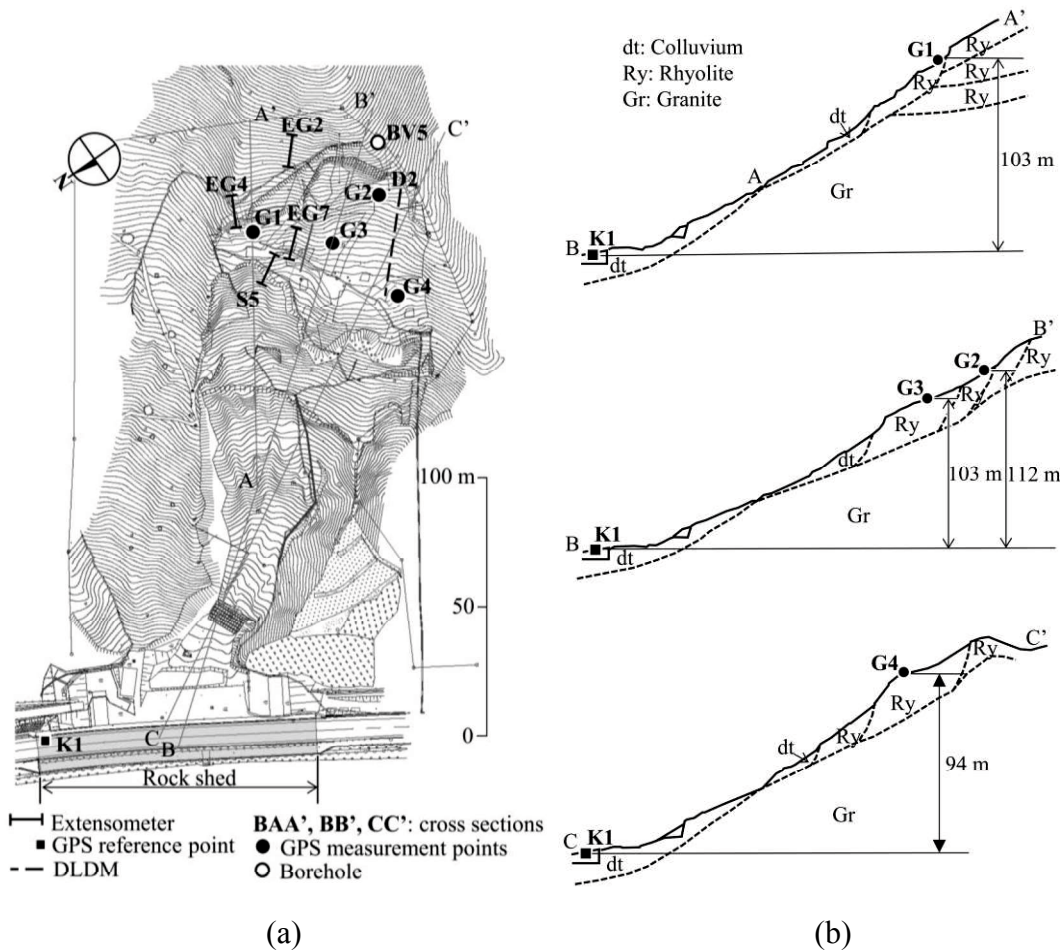
Fig. 3.4. Layout of locations of GPS sensors and extensometers on slope: (a) Plan view and (b) Vertical sections.

3.4.2. Original results

Fig. 3.5a shows the originally measured three-dimensional GPS displacements at G1 for a period of one month obtained by the normal baseline analysis of the static method without error correction. The baseline length and the height difference between G1 and reference point K1 were about 221 m and 103 m, respectively. The epoch interval (measurement interval of the carrier phase of the signal from the satellites) and the session length (the observing duration of the carrier phase measurements) were 30 seconds and 1 hour, respectively. The standard deviations of the measured displacements by G1 (denoted by σ in Fig. 3.5a) were 2.4 mm, 4.5 mm, and 7.1 mm in the directions of latitude, longitude, and height, respectively. The GPS measurement results were rather wavy and scattered (Fig. 3.5a), although the slope might not have

moved at all during this period, as shown in the measurement results by extensometers (Fig. 3.5b).

3.4.3. Effect of error correction for obstructions

Fig. 3.5c presents the monitoring results at G1, for a period of 5 days, extracted from Fig. 3.5a. The red bullets represent an example of the periodically scattered values. The red lines in Fig. 3.6a represent the satellite paths above antenna G1 for the period represented by the red bullets in which the monitoring results were largely scattered (16:00 to 17:00 on 07 November 2012). The numerals represent the satellite numbers. Satellites 2, 4, 5, and 10 moved in the open sky, while satellite 13 moved behind trees.

(a)

(b)

31
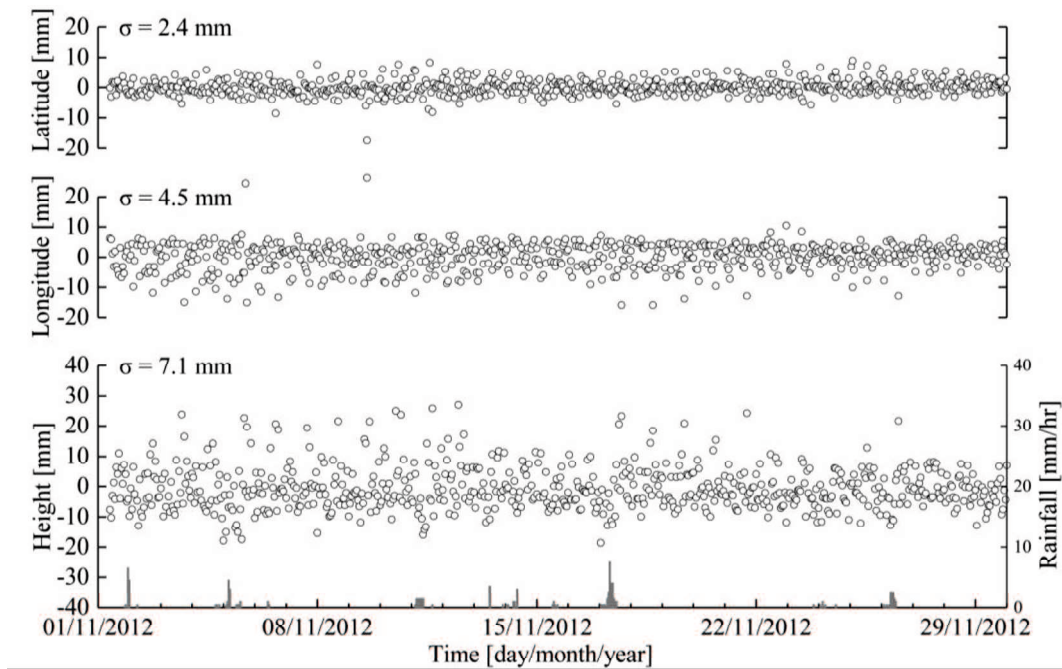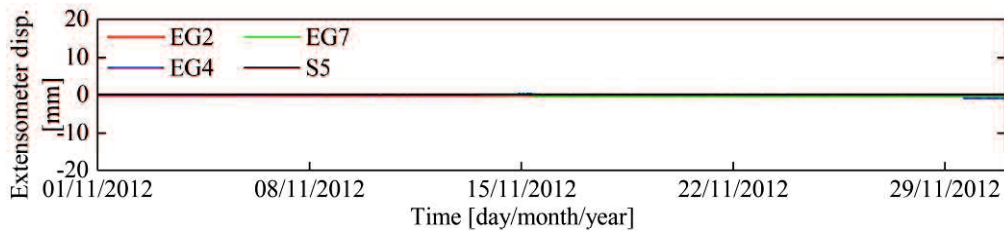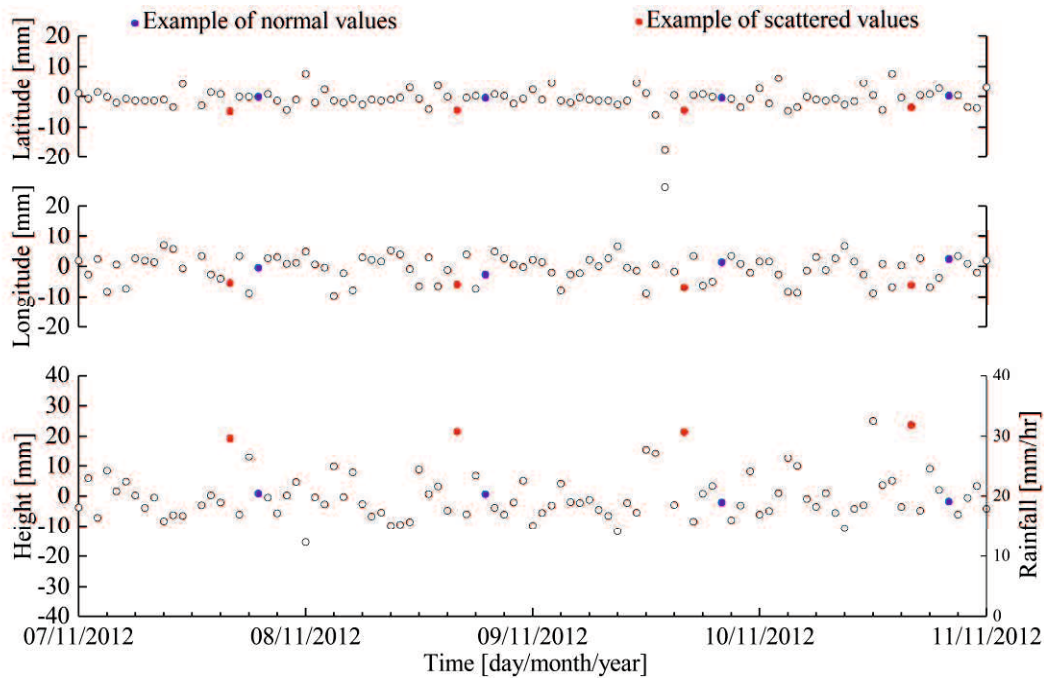
(c)

Fig. 3.5. Monitoring results at: (a) GPS (G1) without error correction from 1 November 2012 to 30 November 2012, (b) Extensometers (EG2, EG4, EG7, and S5) from 1 November 2012 to 30 November 2012, and (c) GPS (G1) without error correction from 7 November 2012 to 10 November 2012.

Figs. 3.7a and 3.7b show the residual errors in the distance between sensor G1 and satellites 13 and 2, respectively. The residuals for satellite 13 are wavy and interrupted in the middle after 16:40, while those for satellite 2 are continuously stable. It is found that the signal from satellite 13 was disturbed; this was the cause of the measurement errors.

On the other hand, an example of normal results, obtained when no satellites moved behind obstacles, is shown by the blue bullets in Fig. 3.5c for the satellite paths during the period given in Fig. 3.6b. All these satellites moved in the open sky, and thus, there were no signal disturbances.
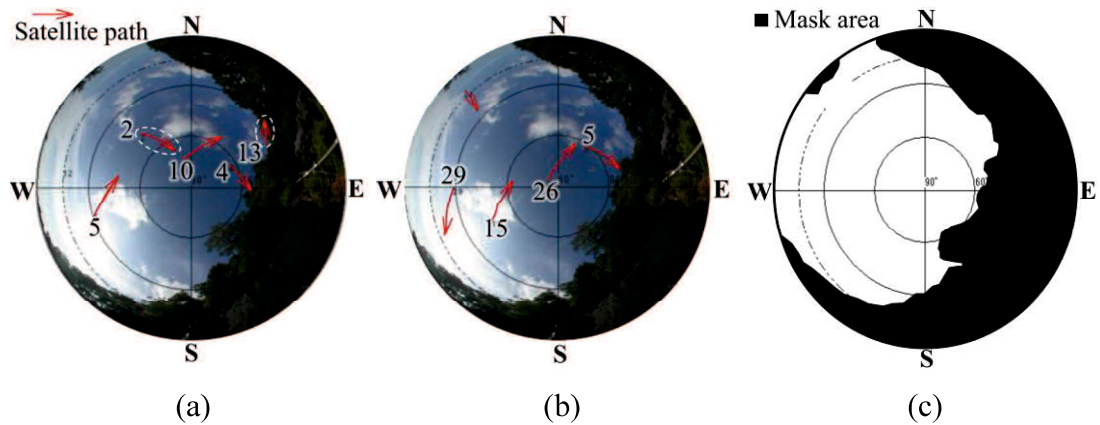
Fig. 3.6. Sky views and trace of satellite orbits above antenna at G1: (a) Period of scattered values (16:00 – 17:00 on 7 November 2012), (b) Period of normal values (19:00 – 20:00 on 7 November 2012), and (c) Mask area.
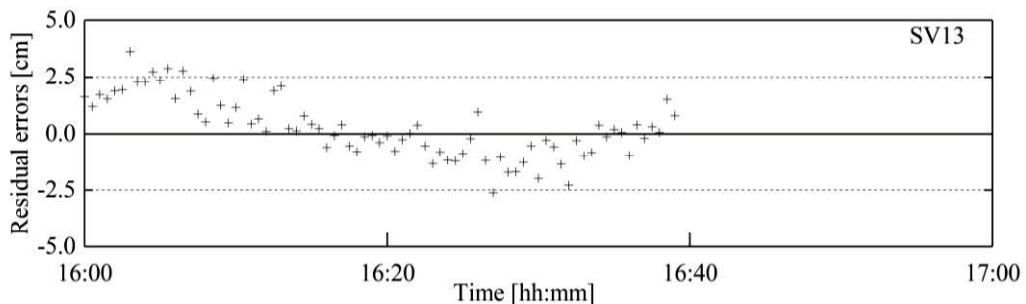
(a)
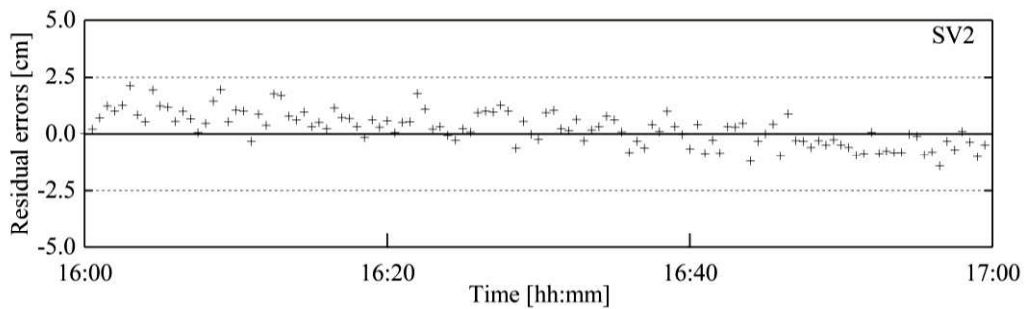
(b)

Fig. 3.7. Transition of residuals at G1 (16:00 - 17:00 on 07 November 2012): (a) Satellite 13 and (b) Satellite 2.

In order to reduce the errors appearing in Fig. 3.5, caused by the signal disturbances brought about by obstructions above the antenna, mask processing is applied (Masunari et al., 2008; Shimizu, 2009; Shimizu et al., 2011, 2014). Mask processing is a procedure for the baseline analysis which does not use the signals from the satellites behind obstructions. The mask area is shown on the sky photo in Fig. 3.6c.

The mask area here is the same as the range in vegetation and the slope surface appearing in the photo above the antenna.

The measurement results after applying mask processing are shown in Fig. 3.8. Comparing Fig. 3.5 and Fig. 3.8, it is seen that the periodical largely scattered results have been greatly reduced. The standard deviations in the directions of latitude, longitude, and height were improved to 1.7 mm, 2.0 mm, and 3.1 mm from 2.4 mm, 4.5 mm, and 7.1 mm, respectively (Table 3.1).

Table 3.1. Standard deviations.

	Latitude (mm)	Longitude (mm)	Height (mm)
Without error correction	2.4	4.5	7.1
After mask processing	1.7	2.0	3.1
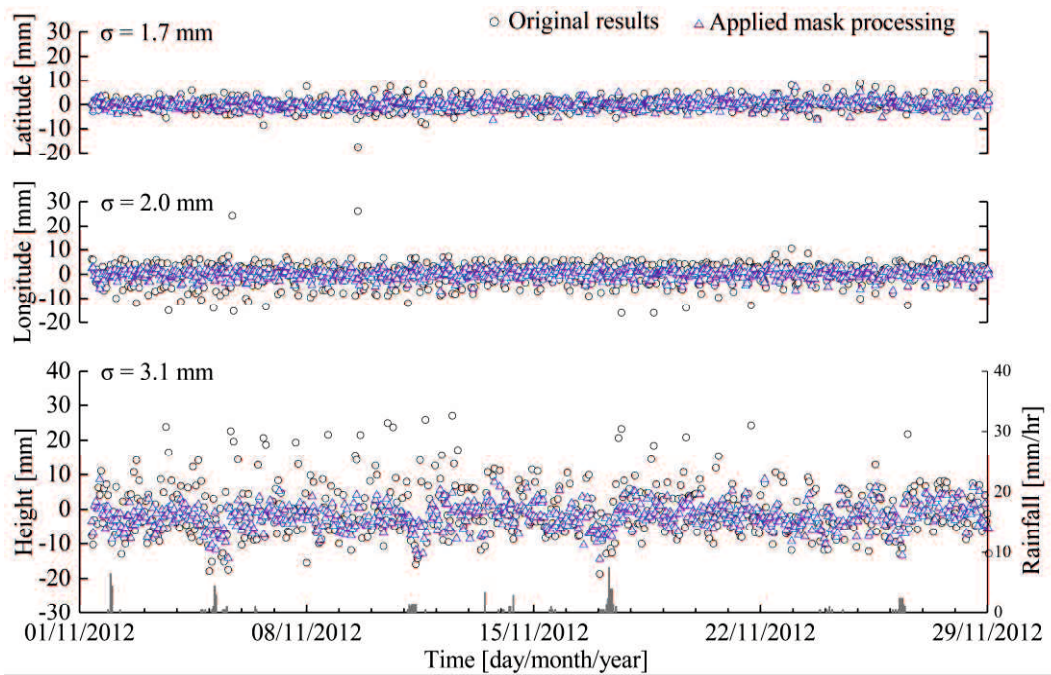
Fig. 3.8. Monitoring results at G1 after error correction by mask processing.

Fig. 3.9 shows the errors due to signal disturbances caused by obstructions above the antenna, ε_p. It can be clearly seen that the errors in this figure caused the wavy and scattered results seen in Fig. 3.5a.
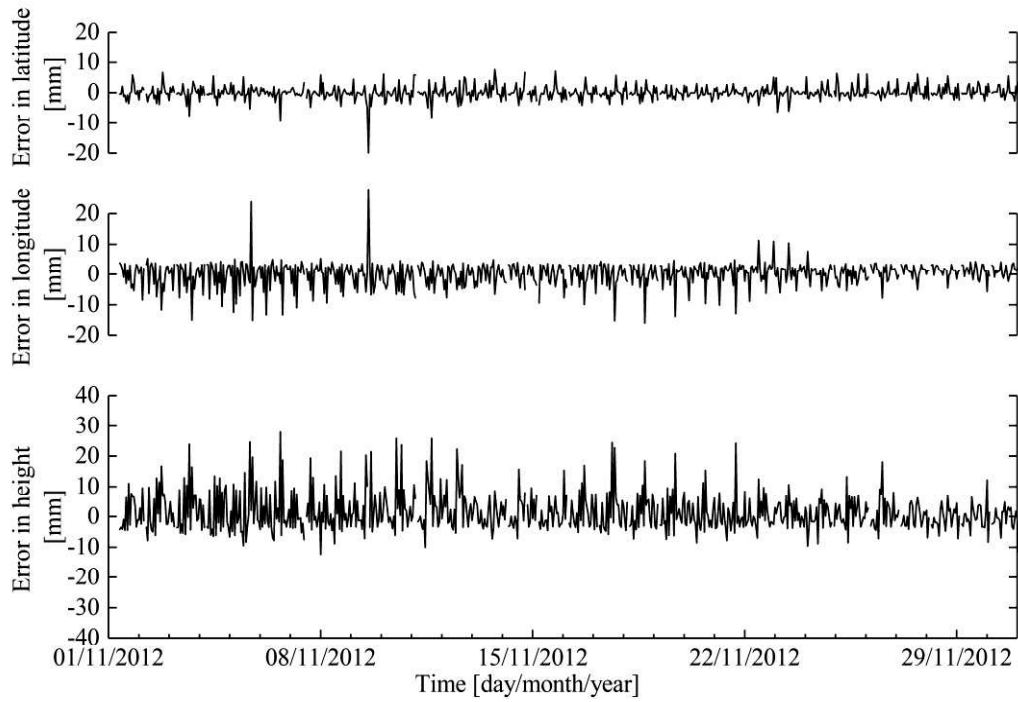
Fig. 3.9. Errors due to signal disturbances caused by obstructions above antenna, ε_p.

3.4.4. Effect of error correction for tropospheric delays

Periodical wavy behavior still remains in the displacement in the direction of height after applying mask processing (see Fig. 3.8). This phenomenon can usually be seen as a consequence of refractive effects, due to air density, when signals propagate through the troposphere. On the other hand, when there is a large difference in height between the reference and the monitoring points, it may not be possible to ignore the bias of the tropospheric delay in precise monitoring (Shimizu et al., 2014). Then, the method of tropospheric delay correction, described in section 3.3.3, is applied.

Fig. 3.10 shows the meteorological data, namely, (a) temperature, (b) relative humidity, and (c) atmospheric pressure, which were observed at the national meteorological observation station (18 km away from the monitoring site). The partial pressure of the water vapor and the zenith tropospheric delay are estimated by Eqs. (3.9) and (3.3), respectively, as shown in Figs. 3.10d and 3.10e.

The corrected results are shown in Fig. 3.11. The periodic wavy behavior in the direction of height, appearing in Fig. 3.8, has been reduced.

35
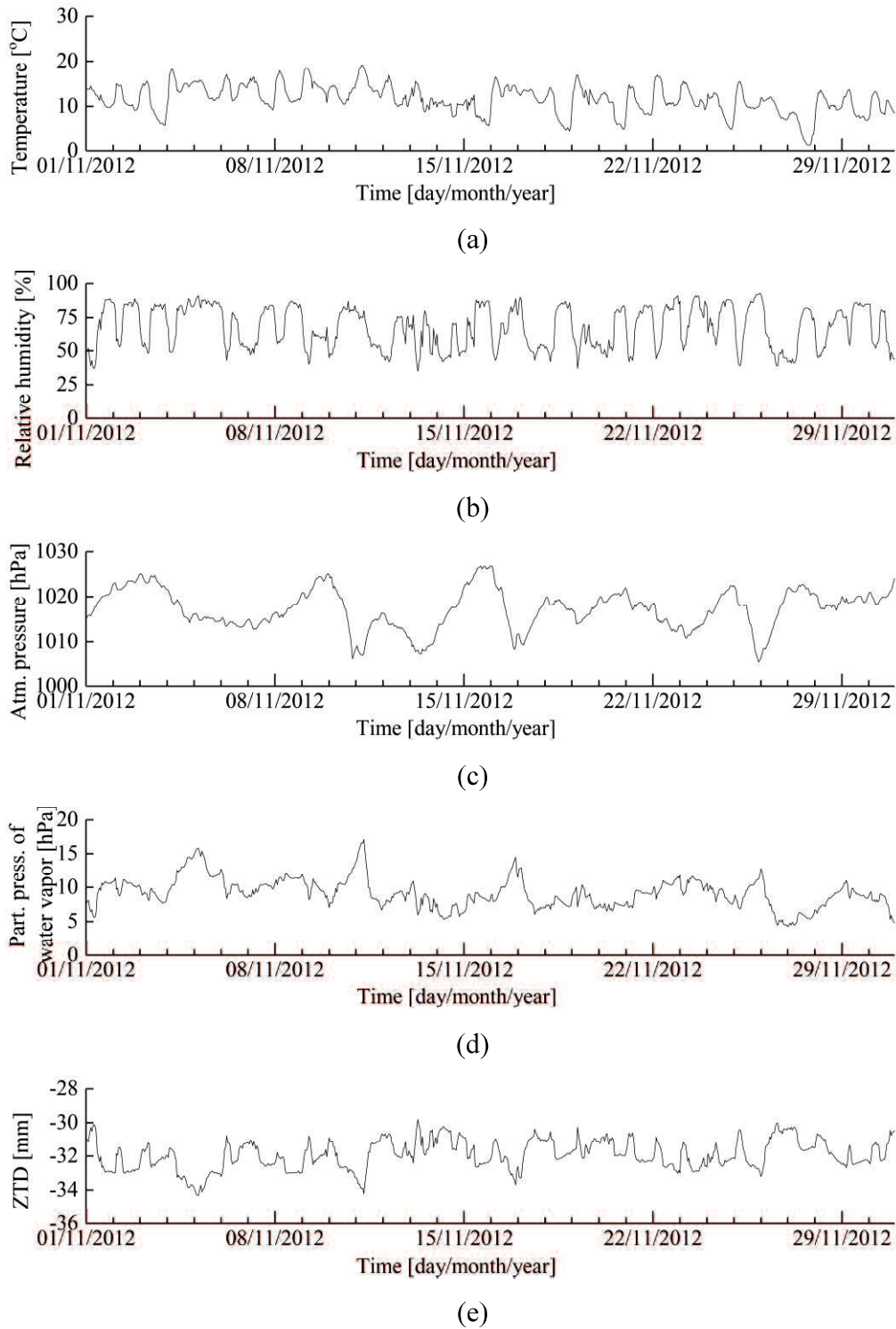
Fig. 3.10. Meteorological data and estimated tropospheric delays (01 November 2012 – 30 November 2012): (a) Temperature, (b) Relative humidity, (c) Atmospheric pressure, (d) Partial pressure of water vapor estimated by Eq. (3.9), and (e) Zenith tropospheric delay (ZTD) estimated by modified Hopfield model.

36
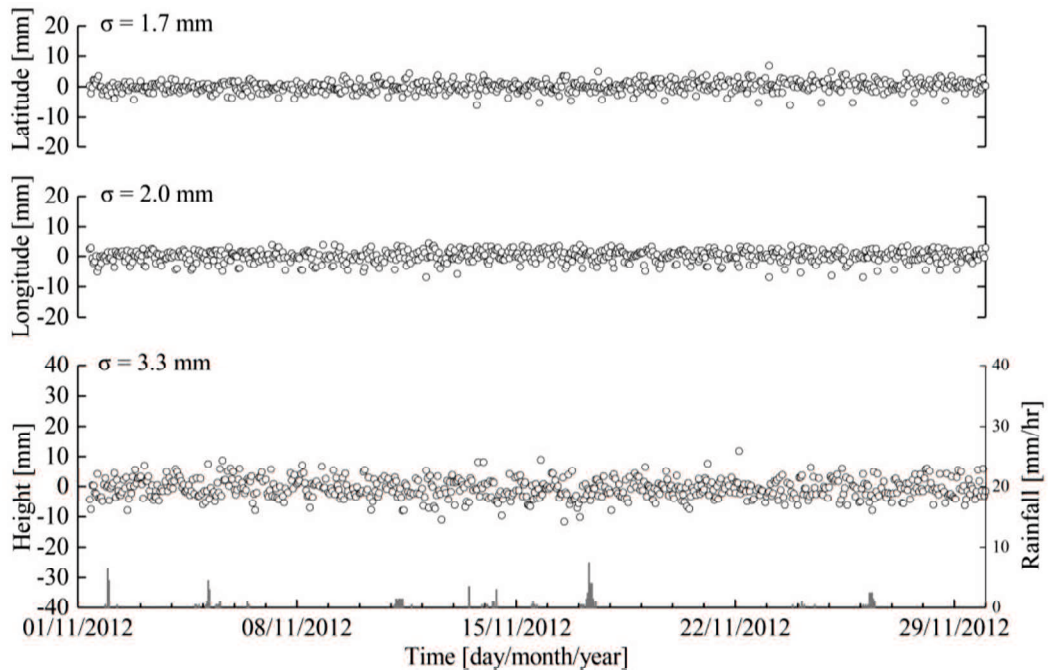
Fig. 3.11. Monitoring results at G1 after error correction by mask processing and tropospheric delay correction.
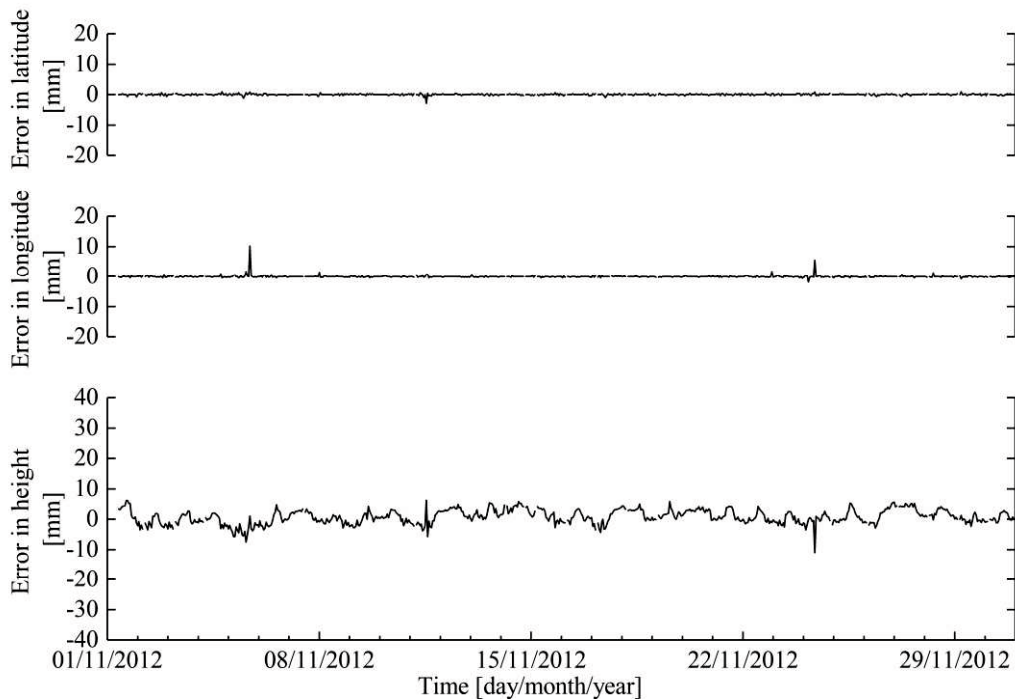
Fig. 3.12. Errors due to tropospheric delays, ε_T.

Fig. 3.12 shows the errors due to tropospheric delays, ε_T. It is found that even when monitoring for a short period, such as one-month, tropospheric delays still affect

the results, especially in the height direction. The validity of tropospheric delay correction in long-term monitoring will be clearly shown in Chapter 4.

3.4.5. Final results

After removing the bias errors, the trend model was applied to estimate the exact displacements among the results with random errors. The final results are shown in Fig. 3.13. Fig. 3.14 shows the random errors, ε_R. It can be seen that these errors are also wavy and scattered; they caused a similar pattern in the results shown in Fig. 3.5. By comparing the final results with the original baseline analysis results given in Fig. 3.5, it is verified that the procedure with error-correction methods, described in section 3.3, was able to improve the original results.
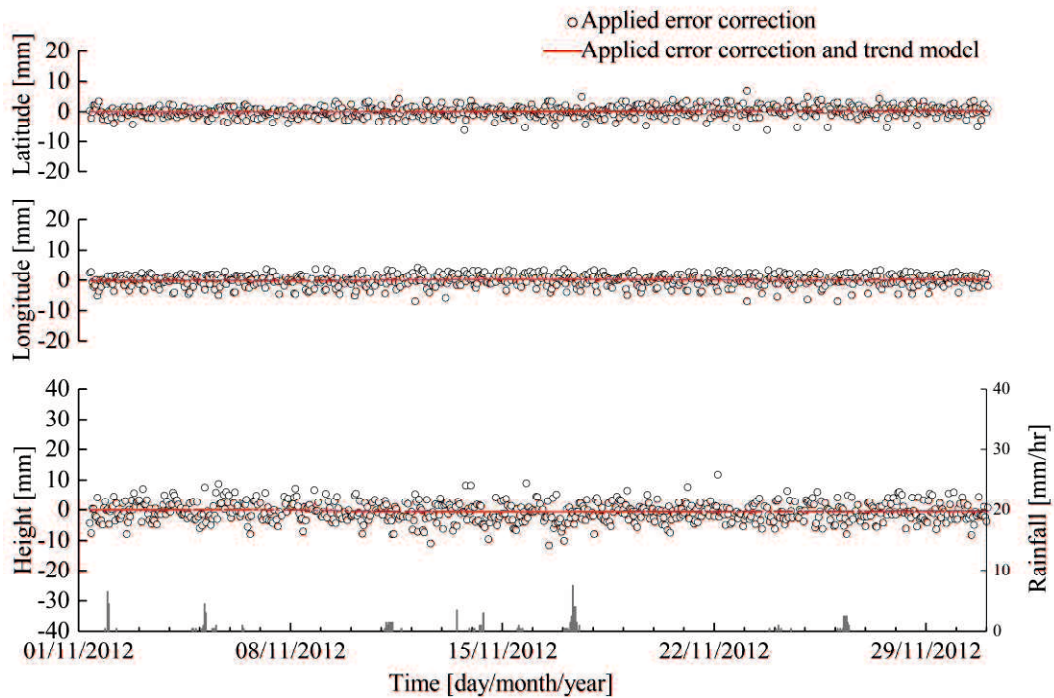
Fig. 3.13. Monitoring results at G1 after applying the trend model with mask processing and tropospheric delay correction.
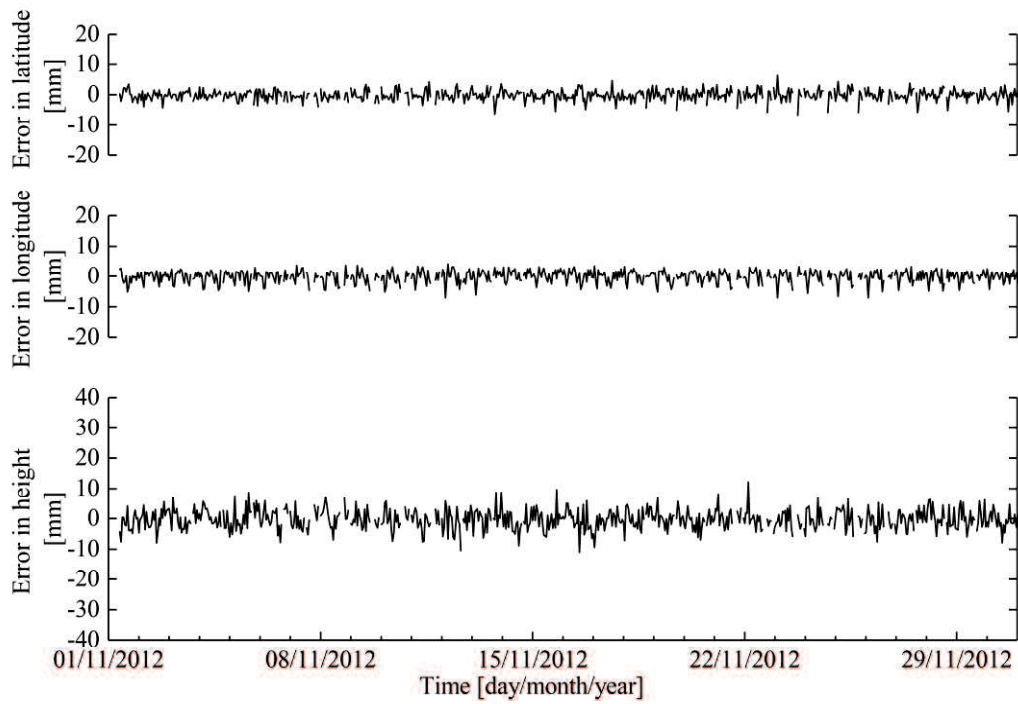
Fig. 3.14. Random errors, ε_R.

Fig. 3.15 shows the Fourier spectrum of the height displacement obtained without any error correction, obtained with mask processing, obtained with mask processing and tropospheric delay correction, and obtained with all the corrections. It can be seen that the periodic behavior has been significantly reduced in the final results. Thus, the procedure with error-correction methods proposed in this study is effective for reducing both bias and random errors.

39
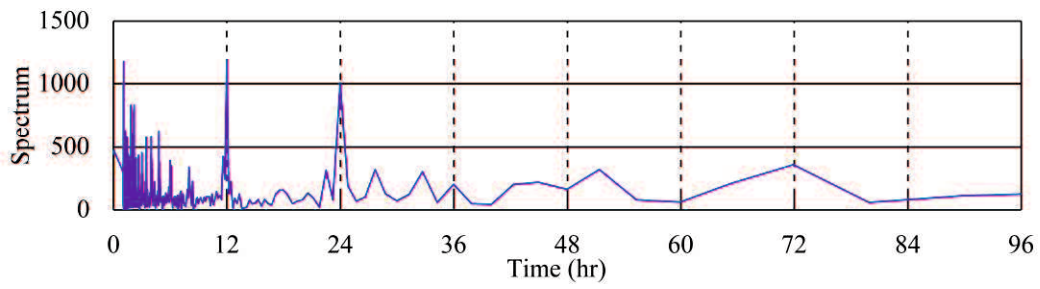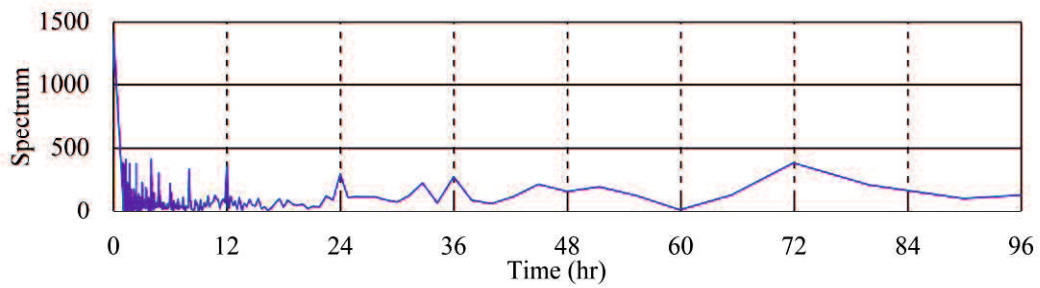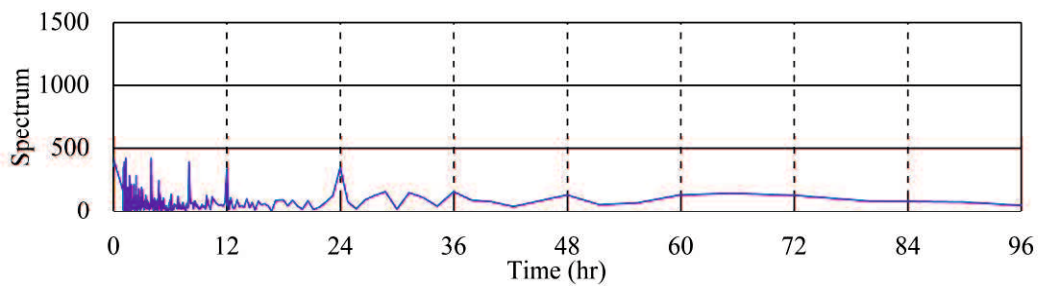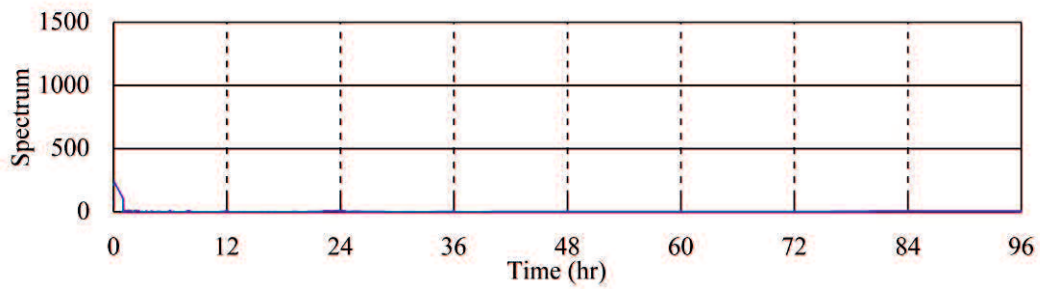
Fig. 3.15. Fourier spectrum of height displacements at G1: (a) Without error correction, (b) With mask processing, (c) With mask processing and tropospheric delay correction, and (d) Applying the trend model with mask processing and tropospheric delay correction.

3.5. Comparison with displacements by surface extensometer and Diffusion Laser Displacement Meter

In order to verify the performance of the GPS monitoring system and the procedure with error-correction methods, the monitoring results are compared with the displacements obtained by a conventional surface extensometer and the Diffusion Laser Displacement Meter (DLDM) (Naya et al., 2008).

3.5.1. Surface extensometer

Fig. 3.16 shows an extensometer, denoted as EG-4, which was also presented in Fig. 3.4. It is a fixed wire extensometer with a precision of 0.3 mm per 30-m baseline (Gili et al., 2000). It was installed in the vicinity of G1. A comparison of the resultant displacements monitored by GPS and those obtained by the extensometer is shown in Fig. 3.17. It is clear in the figure that the displacements monitored by GPS are larger than those obtained by the extensometer. This is because GPS monitoring provides three-dimensional displacements and the absolute magnitude of the displacement vector, including all the components, while the extensometer measurements are one-dimensional. The tendencies of the time-evolution of the displacements monitored by both methods almost coincide. GPS was able to detect increases in displacements due to rainfall, as was the extensometer.

Fig. 3.18 focuses on the behavior in the initial period when the displacements began to increase. The GPS monitoring was able to detect small increases in the displacement at every rainfall occurrence, while the extensometer was not able to detect such increases during the initial period. The inability to detect these increases might have been caused by the friction of a mechanical device in the extensometer.

Although it is generally recognized that the accuracy of GPS displacement monitoring is not as good as that of the extensometer, Figs. 3.17 and 3.18 show that GPS displacement monitoring is almost equivalent in sensitivity to the extensometer or even more sensitive than the extensometer.
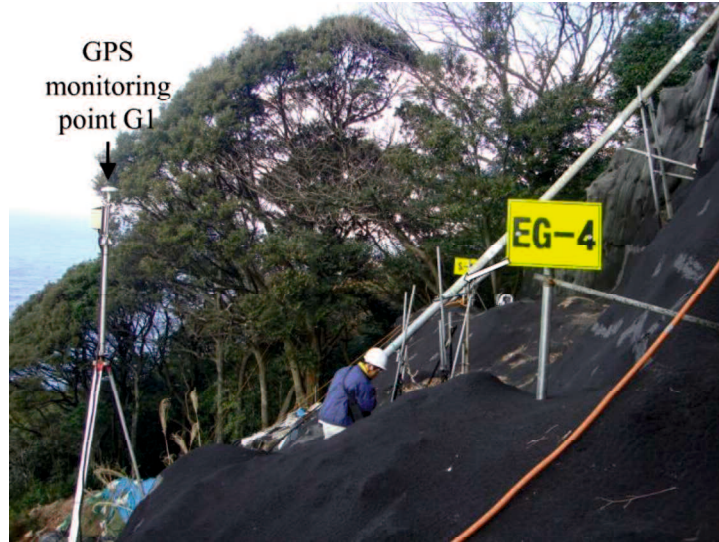
Fig. 3.16. Extensometer measurement EG-4 and GPS sensor at G1 (see Fig. 3.4).
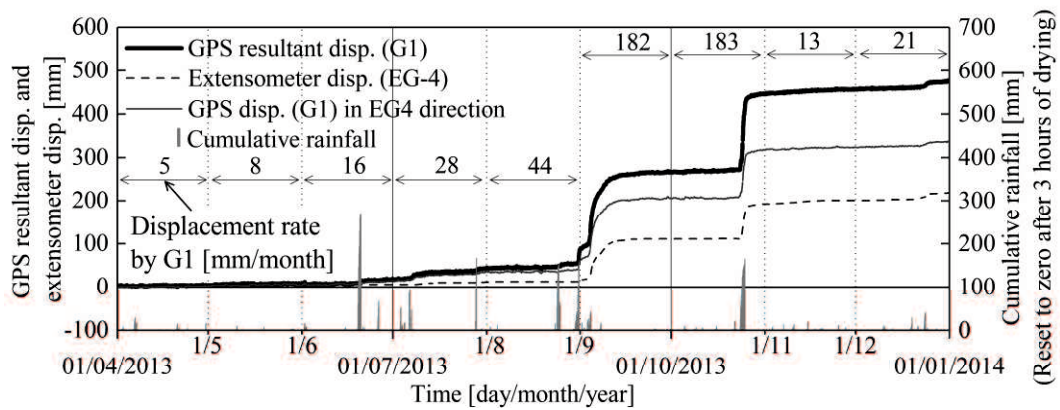
Fig. 3.17. Comparison of displacements monitored by GPS and extensometer EG-4 (01 April 2013 – 01 January 2014).
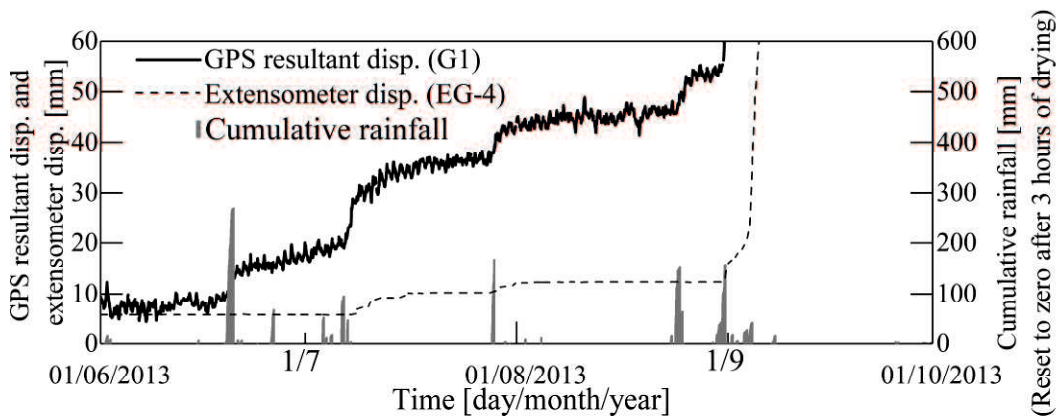
Fig. 3.18. Comparison of displacements monitored by GPS and extensometer EG-4 at beginning of movement (01 June – 01 October 2013).

42

3.5.2. *Diffusion Laser Displacement Meter (DLDM)*

The Diffusion Laser Displacement Meter (DLDM) is a non-contact measurement device employed to measure the distance between the device and a reflector. It was designed to monitor ground movement by a laser meter with the precision of 0.2 mm under ideal environmental conditions (Naya et al., 2008). The DLDM (denoted by D2 in Fig. 3.4) was installed outside of the landslide block, which is the fixed point, and the reflector was set near G4 (see Figs. 3.4 and 3.19). Therefore, the measurement results by the DLDM (D2) and the displacement at G4 by GPS can be compared.

(a)   (b)

Fig. 3.19. Diffusion Laser Displacement Meter (DLDM, see Fig. 3.4): (a) DLDM and (b) Reflector.
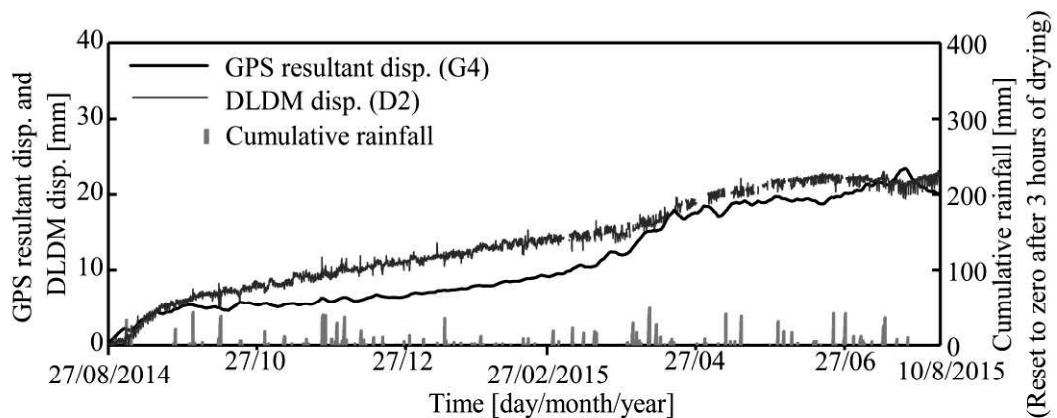
Fig. 3.20. Comparison of displacements monitored by GPS at G4 and DLDM (D2).

Fig. 3.20 shows a comparison of the displacements at G4 by DLDM (D2) and GPS (G4) for one year. The results agree well, namely, with a difference of a few mm. In this study, GPS was able to perform almost equally to the DLDM.

3.6. Chapter summary

In this chapter, a procedure with error-correction methods was proposed and applied to GPS displacement monitoring at a large-scale steep slope to reduce the errors caused by obstructions above the antennas and by tropospheric delays, and to estimate the exact displacements through the use of a filtering method. The validity of the procedure was verified by a practical application. The following conclusions can be drawn:

(1) The procedure to enhance the accuracy of the displacement measured with GPS has two steps. The first step is to apply mask processing and tropospheric delay correction at the same time to reduce and/or eliminate bias errors from the measurement results. Mask processing is an analysis performed without the use of the signals transmitted from the satellites located behind obstructions above certain antennas in order to reduce the signal disturbance due to the obstructions. Tropospheric delay correction uses the modified Hopfield model together with the meteorological conditions. The second step is to apply the trend model, a time-series filtering, to estimate the exact values from the measured results with random errors.

(2) The procedure was applied to the monitoring results obtained every hour for one month at a large unstable steep slope with a height difference of more than 100 m. Although the original results were wavy and scattered, due to the effects of obstructions above certain antennas and tropospheric delays, the wavy and largely scattered errors were removed, and the final results were smoothed with only small standard deviations, i.e., 1-2 mm in the horizontal direction and 3-4 mm in the vertical direction. It was proven that the above procedure was able to improve the original scattered monitoring results.

(3) In order to investigate the performance of the GPS displacement monitoring system, it was compared with a standard extensometer and a Diffusion Laser

Displacement Meter. It was found that the measurement sensitivity of the GPS displacement monitoring system was almost equivalent to that of the extensometer and the Diffusion Laser Displacement Meter.

Chapter 4
LONG-TERM CONTINUOUS MONITORING OF GROUND SURFACE
DISPLACEMENT AT A LARGE-SCALE STEEP SLOPE

4.1. Introduction

Knowledge of the mechanism of the displacement behavior of a slope is essential for assessing the stability of the slope, for predicting its future behavior, and for designing countermeasures. Monitoring the real behavior is important to investigating this mechanism.

This chapter discusses continuous displacement monitoring at a large-scale steep slope using the GPS displacement monitoring system and the proposed procedure, as described in Chapter 3. Based on long-term monitoring results, it is seen that local collapses have occurred in some areas of the slope due to the increase in the groundwater level after rainfalls. Hence, the mechanism of the occurrence of large displacements of the slope due to the increase in the groundwater level is investigated by considering both field measurements and numerical simulations. The displacement behavior of the slope seems to be dominated by discontinuities, namely, joints and bedding planes, etc. The Universal Distinct Element Code (UDEC) (Itasca, 2004) is employed as the numerical code. Changes in the groundwater level (GWL) are also taken into account.

4.2. Continuous displacement monitoring

4.2.1. Site and monitoring points

In order to investigate the applicability of the procedure to enhance the accuracy of the displacement monitored with GPS and to establish an early warning system, continuous displacement monitoring was conducted at the slope, as described in section 3.4.1. Continuous displacement monitoring began at the slope on 11 March 2013 with the application of the proposed procedure. All the processes of the data acquisition, the baseline analysis, the error correction, and the providing of the three-

dimensional displacements were automatically conducted. The monitoring conditions for each monitoring point are given in Table 4.1.

Table 4.1. Monitoring conditions.

Monitoring points	Baseline length (m)	Height difference from K1 (m)	Monitoring period (date/month/year)
G1	221	103	11/03/2013 − 12/08/2014
G2	258	112	11/03/2013 − 26/01/2018
G3	233	103	12/08/2014 − 26/01/2018
G4	230	94	12/08/2014 − 26/01/2018

The locations of the GPS sensors are shown in Figs. 3.2, 3.3, and 3.4. Monitoring was conducted in two periods: (1) from March 2013 to August 2014 and (2) from August 2014 to January 2018. Two monitoring points, G1 and G2, and three monitoring points, G2, G3, and G4, were used for the first and second periods, respectively. The sky views at monitoring points G2, G3, and G4 are presented in Fig. 4.1.

| (a) | (b) | (c) |
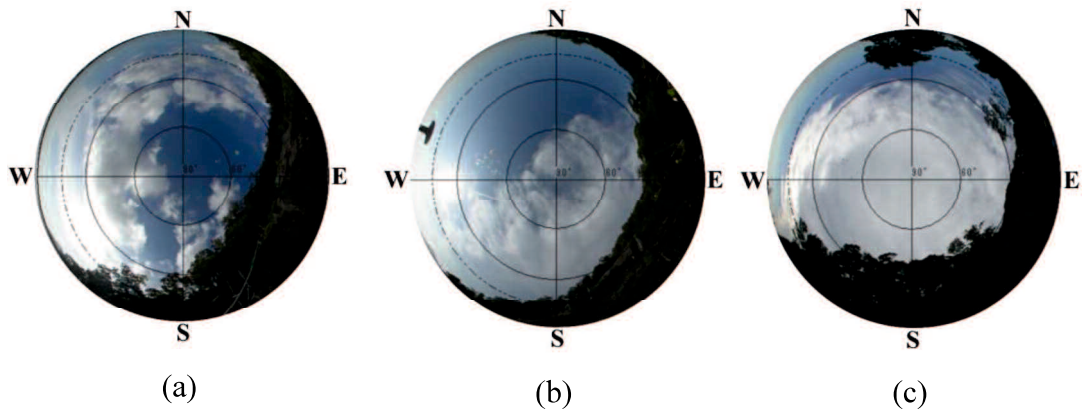
Fig. 4.1. Sky views above GPS antennas at: (a) G2, (b) G3, and (c) G4.

4.2.2. Monitoring results

4.2.2.1. March 2013 to August 2014

Fig. 4.2 shows the monitoring displacements in the directions of latitude, longitude, and height at G1 and G2 from 11 March 2013 to 12 August 2014. The three-

dimensional displacements were continuously obtained every hour without missing any data, except during the maintenance period.

The standard deviations of each component are 1.6 mm, 2.0 mm, and 4.5 mm at G1, and 1.9 mm, 1.6 mm, and 3.6 mm at G2, respectively (Table 4.2). Those values are better than the standard deviations obtained by a conventional GPS survey. The resultant displacement in Fig. 4.2 indicates the absolute magnitude of the displacement vector. The cumulative rainfall and the groundwater level from the ground surface at BV5 (see Fig. 3.4) are also shown in Fig. 4.2.
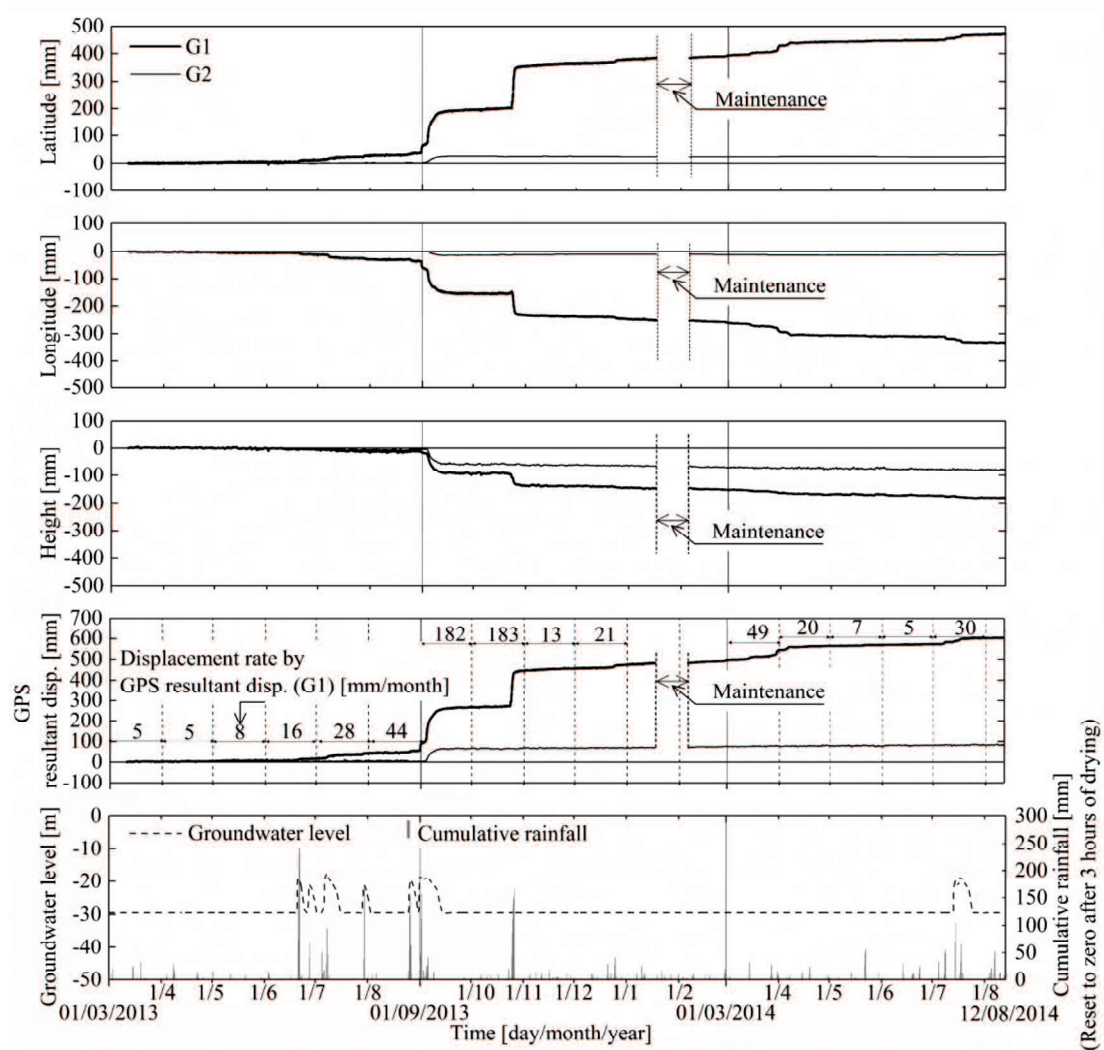
Fig. 4.2. Continuous three-dimensional displacement monitoring results (11 March 2013 to 12 August 2014).

From March to the middle of June (dry period), the displacements at both G1 and G2 were small, and they increased at a rate of less than several millimeters per

48

month. After a heavy rainfall in the middle of June, with a cumulative amount of 270 mm, the displacement at G1 clearly increased with every rainfall having a cumulative amount of more than 50 mm. The resultant displacement velocity became 44 mm/month.

Other heavy rainfalls, with cumulative amounts of 153 mm on 24 August and 157 mm on 31 August, brought about a quick and large displacement at G1. Then, by 10 September, the displacement had increased up to 185 mm in the north direction, 145 mm in the west direction, and 85 mm in settlement.
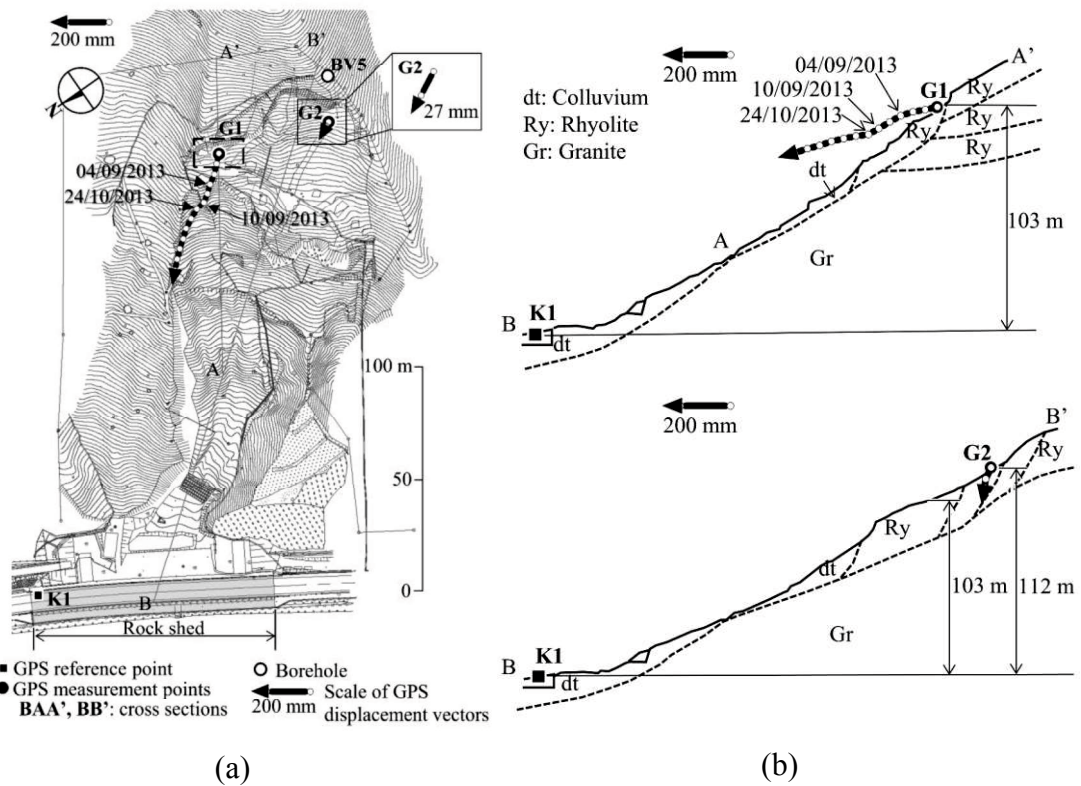
Fig. 4.3. Displacement vectors at G1 and G2 (11 March 2013 to 12 August 2014 – every 50 mm of the resultant displacement denoted by ○ in the vectors): (a) Plan view and (b) Vertical sections.

Fig. 4.3 shows the time-evolution of the displacement vectors in the plan view and the vertical sections. The direction of the displacement at G1 was dominantly horizontal until 4 September, after which it became parallel to the boundary between the rhyolite and the granite. This indicates that a slip might have occurred along the boundary. Actually, a local failure occurred just below G1, as shown in Fig. 4.4, and one lane of the road beneath the slope was closed on 30 August and both lanes of the

road were closed on 04 September based on the monitoring results. The displacement at G1 continued to increase with a quick and large displacement of 183 mm in one month due to heavy rainfall on 24 October.

On the other hand, no remarkable displacement was monitored at G2 except in early September. The direction of the displacement at G2 was dominantly subsidence, and it was parallel to the main scarp behind G2.

As seen in Figs. 4.2 and 4.3, the three-dimensional displacements monitored by GPS provided important information for assessing the stability evolution of the slope.

(a)   (b)

Fig. 4.4. Local failure around G1: (a) Situation on 28 January 2013 and (b) Situation on 31 August 2013 (adapted from Naya et al., 2014).

Table 4.2. Standard deviations (11 March 2013 to 12 August 2014).

Monitoring points	Latitude (mm)	Longitude (mm)	Height (mm)
G1	1.6	2.0	4.5
G2	1.9	1.6	3.6

4.2.2.2. August 2014 to January 2018

The local failure that occurred beneath G1 finally approached monitoring point G1. Since countermeasure work was performed to keep the road safe, even though the landslide block around G1 was about to collapse, the sensor at G1 was removed on August 2014. In order to monitor the right-hand side (southwest side) of the slope, two new monitoring points, G3 and G4, were installed in addition to G2 (see Fig. 3.2).

Fig. 4.5 shows the monitoring displacements at G2, G3, and G4 from 12 August 2014 to 26 January 2018. The standard deviations in the direction of latitude, longitude, and height are 1.7 mm, 1.7 mm, and 4.0 mm at G2, 2.4 mm, 1.7 mm, and 3.7 mm at

G3, and 2.4 mm, 1.6 mm, and 3.8 mm at G4, respectively (Table 4.3). Continuous three-dimensional displacement monitoring was performed for three and a half years without missing any data, except during the maintenance period.

Table 4.3. Standard deviations (12 August 2014 to 26 January 2018).

Monitoring points	Latitude (mm)	Longitude (mm)	Height (mm)
G2	1.7	1.7	4.0
G3	2.4	1.7	3.7
G4	2.4	1.6	3.8
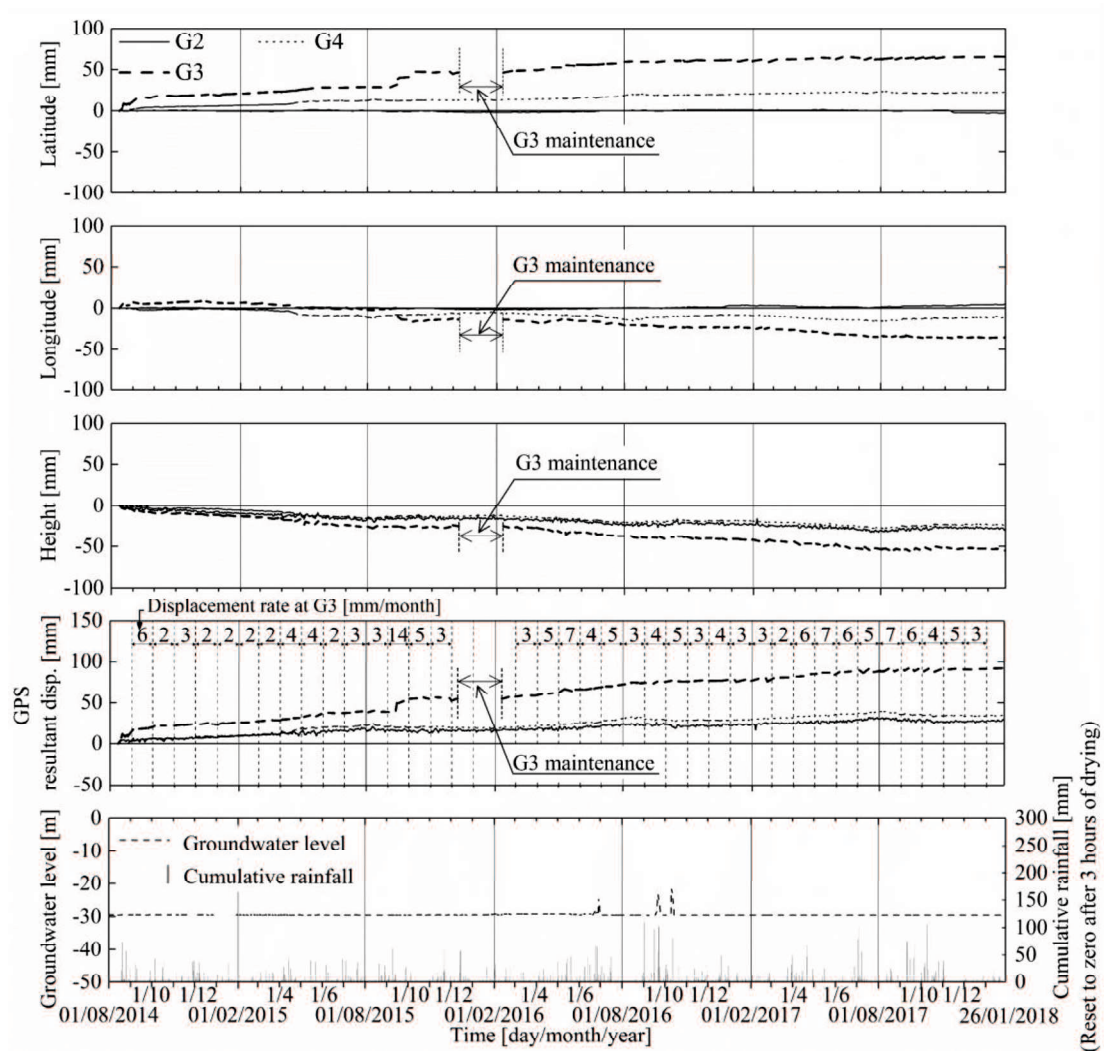
Fig. 4.5. Continuous three-dimensional displacement monitoring results (12 August 2014 to 26 January 2018).

51

During this period, there were no heavy rainfalls, and the resultant displacements at G2, G3, and G4 were small with an average velocity of less than 2 to 7 mm per month. Therefore, it is seen that the slope is stable at present. However, those displacements are still increasing even now, and thus, monitoring should be continued.

Fig. 4.6 shows the displacement vectors in the plan view and in the vertical sections. In the plan view, the directions of the displacements at G3 and G4 are different until 13 December 2014. However, the displacements in these two directions begin to coincide after that time. In the vertical sections, the directions of the displacements at G3 and G4 are almost parallel to the slip surfaces and the boundary between the rhyolite and the granite. In addition, the direction of the displacement at G2 was slightly behind and below the others. Those at G2, G3, and G4 represent typical landslide behavior. It is seen that three-dimensional monitoring by GPS has the potential to demonstrate the detailed behavior of the slope.

(a)   (b)
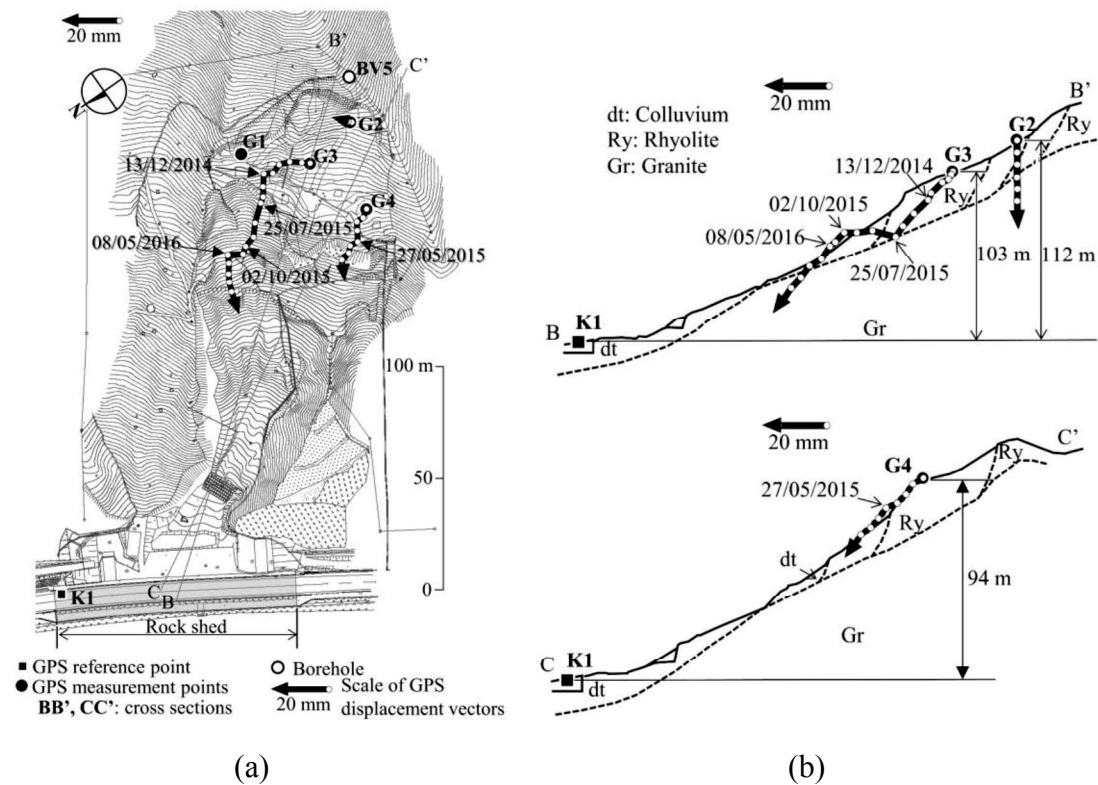
Fig. 4.6. Displacement vectors at G2, G3, and G4 (12 August 2014 to 26 January 2018 – every 5 mm of resultant displacement denoted by ○ in the vectors): (a) Plan view and (b) Vertical sections.
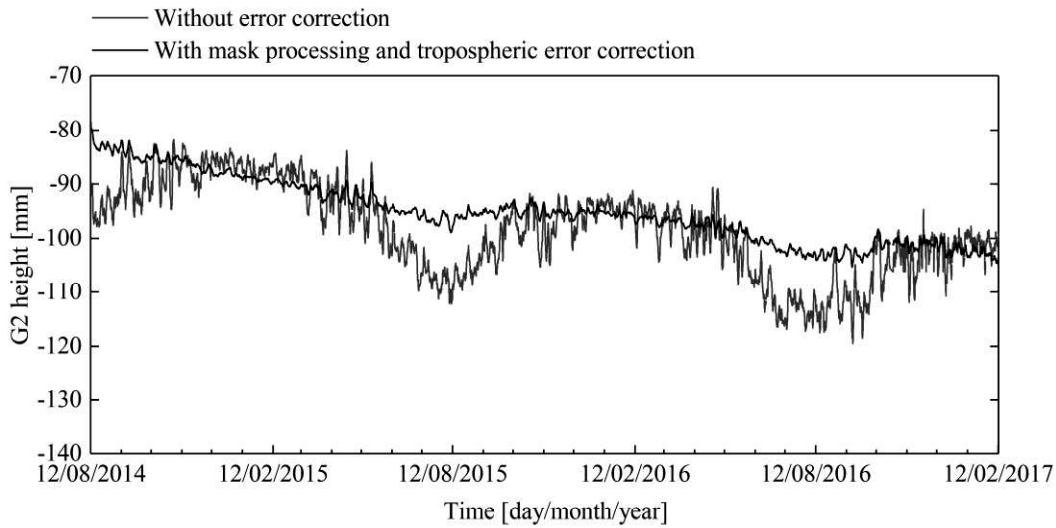
Fig. 4.7. Displacement in direction of height at G2 with and without correction of mask processing and tropospheric delay correction.

Fig. 4.7 shows a comparison between the displacements in the direction of height with and without tropospheric delay correction and mask processing for two and a half years. The results without correction are wavy, not only during short periods, but also over the annual period. On the other hand, such a phenomenon is not seen in the results for which tropospheric delay correction and mask processing were applied. It is confirmed that the procedure with error-correction methods is effective for reducing and/or eliminating the errors. It is worth applying tropospheric delay correction and mask processing for precise monitoring when using GPS.

4.3. Mechanism of occurrence of large displacement at heavy rainfall

4.3.1. Problem setting

As discussed in section 4.2, long-term monitoring using the GPS displacement monitoring system was conducted at the slope to predict future failures. Fig. 4.8 shows the displacements at GPS monitoring points G1, G2, and extensometer EG4 from May to October 2013 extracted from Fig. 4.2.

There were no remarkable displacements in the dry season until the middle of June 2013, as shown in Fig. 4.8. The GWL at wells W2, BV1, and B5' was almost stable during this period, from May to October 2013. When the cumulative rainfall

reached 270 mm a day on 20 June and the GWL at well BV5 rose to a depth of -19 m from the ground surface, the resultant displacement at G1 had increased by 7 mm. With each further incident of heavy rainfall, on 26 June, 6 July, 28 July, and 25 August, the GWL at well BV5 rose to approximately -20 m. Consequently, the resultant displacement gradually increased up to 50 mm, as shown in Fig. 4.8.

On 31 August, heavy rainfall struck the slope for the 6th time that year. The GWL at BV5 rose to a depth of -18.5 m and the resultant displacement at G1 suddenly increased by 40 mm. After a light rain, the GWL at BV5 continued to a depth of around -20 m, and a large resultant displacement of more than 200 mm was recorded. During the same period, the resultant displacement at G2 increased by 60 mm, although it was very small until 3 September. A strong relationship was clearly found between the large increase in displacement and the GWL.
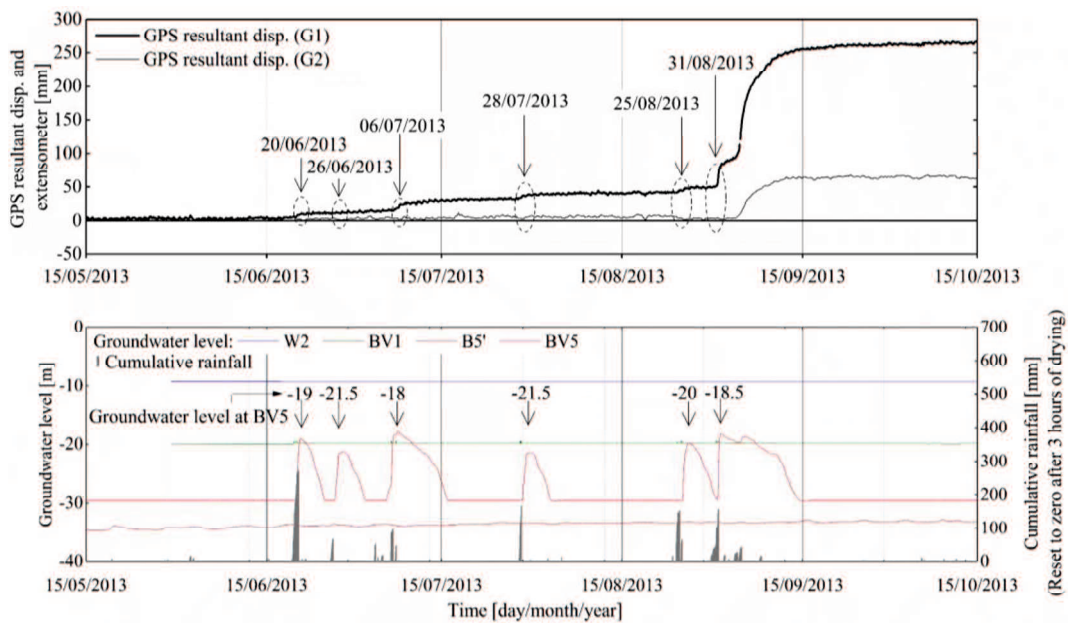
Fig. 4.8. Continuous three-dimensional displacement monitoring results (May to October 2013).

Fig. 4.9 shows the displacement vectors at G1 and G2 in the plan view and the vertical sections from May to October 2013. The directions of the displacement vectors are toward the downward slope in the plan view. In vertical section BAA', the displacement vector at G1 was almost parallel in the assumed slip surface (i.e., the boundary between the rhyolite and the granite), while the displacement at G2 was

mainly subsidence or in a similar direction to the slope scarp in section BB' (see Fig. 4.9b). From these displacement behaviors, it seems that the upper block of the slope, including measurement points G1 and G2, became unstable.

Fig. 4.9. Displacement vectors at G1 and G2 (May to October 2013 – every 50 mm of the resultant displacement denoted by ○ in the vectors): (a) Plan view and (b) Vertical sections.

4.3.2. Numerical simulations

The question as to why the rise in the GWL caused unstable displacement behavior emerges. The mechanism of the occurrence of large displacements due to the increase in the groundwater level will be discussed by means of numerical simulations.

Since the slope is comprised of discontinuities, Distinct Element Methods (DEM) are the most appropriate tools for the simulation of jointed rock slopes. The UDEC was employed to investigate the mechanism of the displacement behavior. The mechnical properties are given in Table 4.4.

.

55

Table 4.4. Mechanical properties of rock at studied slope.

Parameter	Colluvium	Rhyolite	Granite
Density (kg/m^3)	2500	2500	2500
Elastic modulus (MPa)	580	1200	9100
Poisson's ratio	0.31	0.29	0.20

Discontinuity						
Normal stiffness, j_{kn} (MPa/m)	Shear stiffness, j_{ks} (MPa/m)	Friction angle, j_{fric} (degree)	Cohesion, j_{coh} (MPa)	Permeability factor, j_{perm} (1/MPa. sec)	Residual hydraulic aperture, a_{res} (m)	Aperture at zero normal stress, a_{zero} (m)
1.0×10^3	1.0×10^3	20	0.1	1.0×10^8	2.0×10^{-4}	5.0×10^{-4}

Section BB', shown in Fig. 4.9b, was chosen as a section for simulation. Fig. 4.10 shows a UDEC model for this analysis. The model includes several blocks composed of granite, rhyolite, and colluvium. The main discontinuities exist along the three boundaries between the granite and the rhyolite, the granite and the colluvium, and the rhyolite and the colluvium. In addition, there are a few discontinuites in the rhyolite. The GWL is shown in Fig. 4.10 for the two cases studied here: $h_w = 127.5$ m in Case 1 and $h_w = h_d = 127.6$ m in Case 2. h_w and h_d are the groundwater height and the discontinuity height, respectively, measured from the level of the slope toe on the right-hand side. In Case 2, the groundwater rises up to the discontinuity level on the right-hand side (at point D in Fig. 4.10). The left and right boundaries of the region are fixed in the horizontal direction. The bottom boundary of the region is fixed in both vertical and horizontal directions.
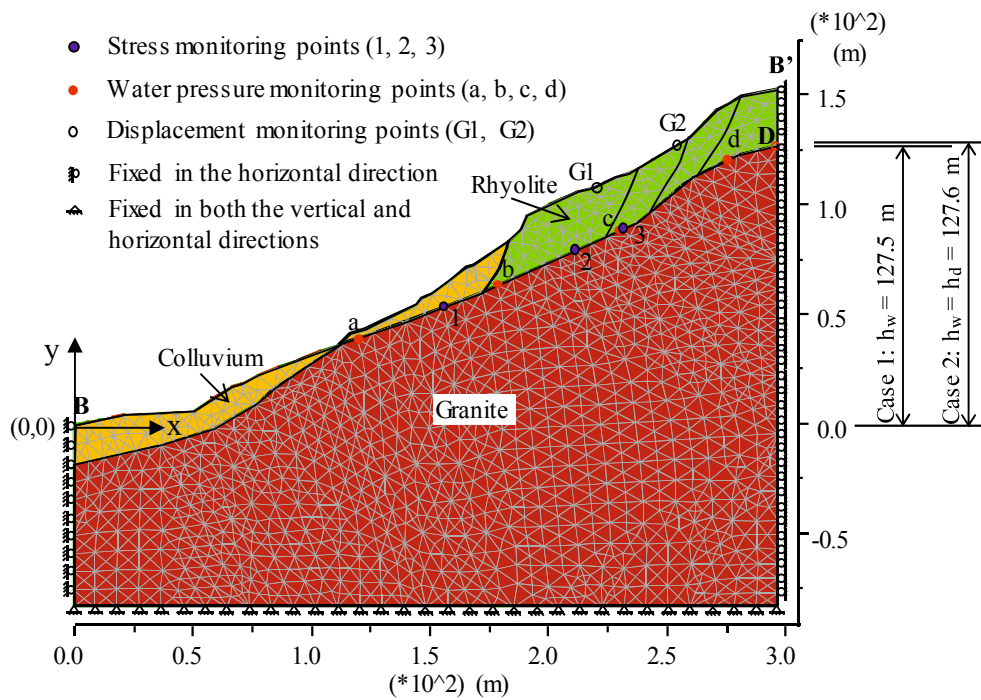
Fig. 4.10. UDEC model.

The procedure of the analysis is as follows: (1) the initial model is assumed as shown in Fig. 4.10; (2) gravity is applied; and (3) the GWL is assumed to rise up at point D on the discontinuity (see the right-hand boundary of the model in Fig. 4.10). As mentioned above, two cases of water level are considered: Case 1 is $h_w = 127.5$ m (10 cm below discontinuity point D) and Case 2 is $h_w = h_d = 127.6$ m (at point D).

The stresses on the discontinuity are calculated at points 1, 2, and 3 during the changes in water pressure. The water pressure is also calculated at points a, b, c, and d. Displacements are obtained at two points, G1 and G2.

4.3.3. Results and discussions

Firstly, the initial force equilibrium status is calculated. Fig. 4.11 shows the unbalanced force of the slope. At the beginning, the unbalanced force increases very quickly; then it decreases gradually and stabilizes to the value of zero after 2314 cycles (Fig. 4.11a). Therefore, an equilibrium state is reached.

57
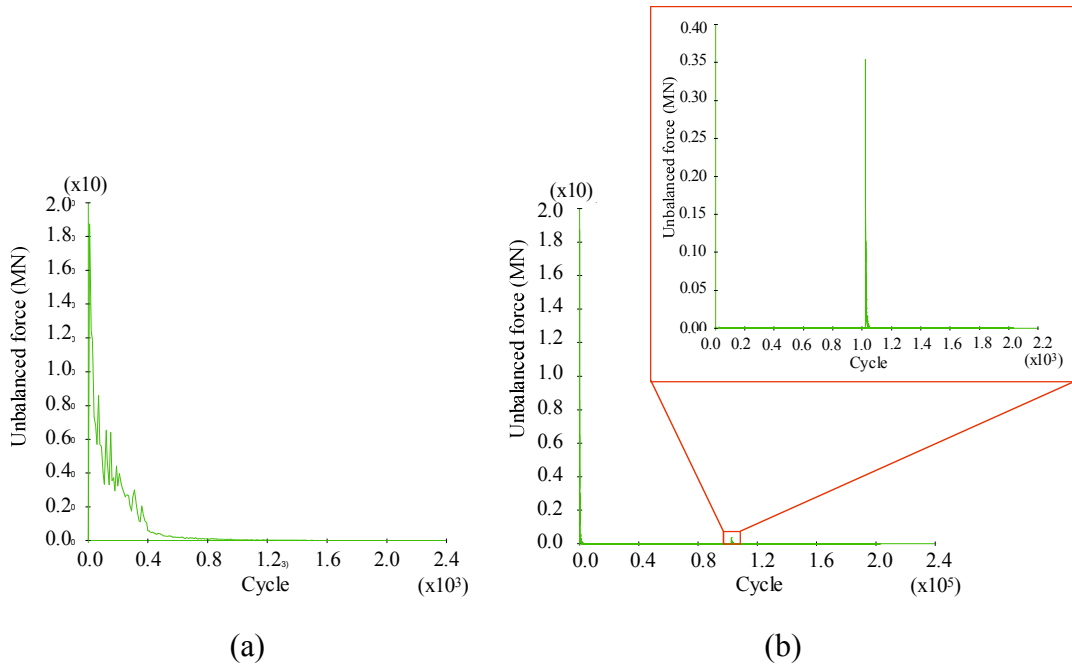
Fig. 4.11. Unbalanced force: (a) Initial equilibrium and (b) After the water level reaches point D.
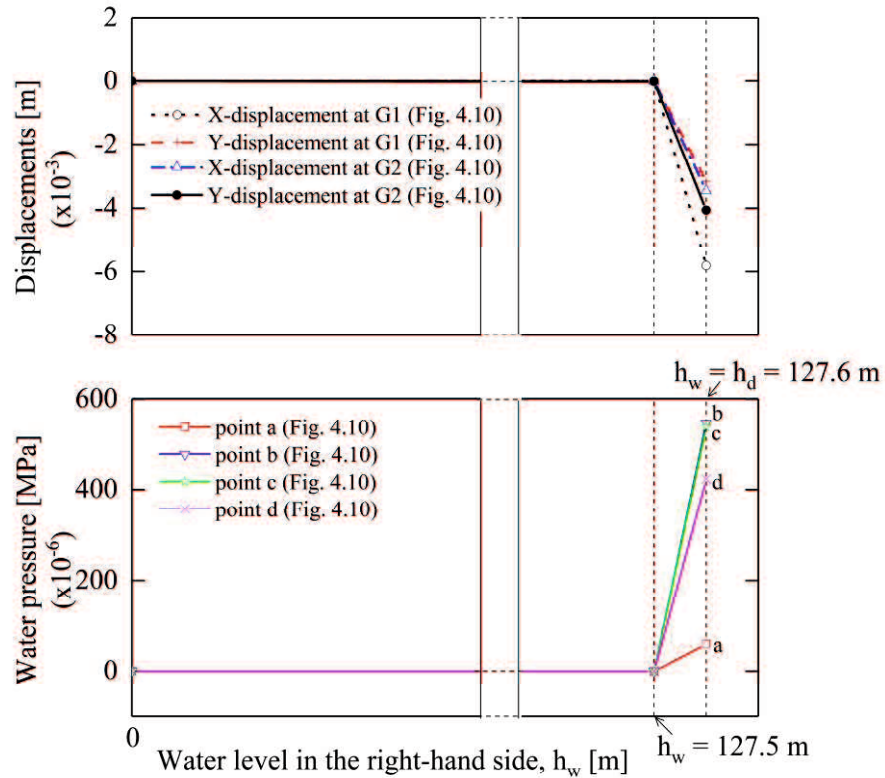
Fig. 4.12. Relationship between changes in water pressure and displacements.

Then, the water level is introduced as reaching point D on the discontinuity (Case 2 in Fig. 4.10). Under such a condition, the unbalanced force rapidly increases, as shown in Fig. 4.11b. This indicates that the slope is unstable and movement might occur.

Fig. 4.12 shows the relationship between the changes in water pressure in the discontinuities and the displacements at G1 and G2. In the case for which the water level is lower than discontinuity point D (Case 1 in Fig. 4.10), the water pressure is zero at all points. When the water level reaches point D on the discontinuity (Case 2 in Fig. 4.10), the water pressure significantly increases at all points, i.e., a, b, c, and d. Small displacements are generated at G1 and G2 in Case 1. The displacements increase drastically in Case 2. In Case 2, the displacement at G1 increases about 6.0 mm in the horizontal direction and 3.0 mm in the vertical direction. Similarly, the displacement at G2 increases about 4.0 mm in both directions (Fig. 4.12). It is found that the increase in water pressure in the discontinuity causes the displacement of the slope to increase.
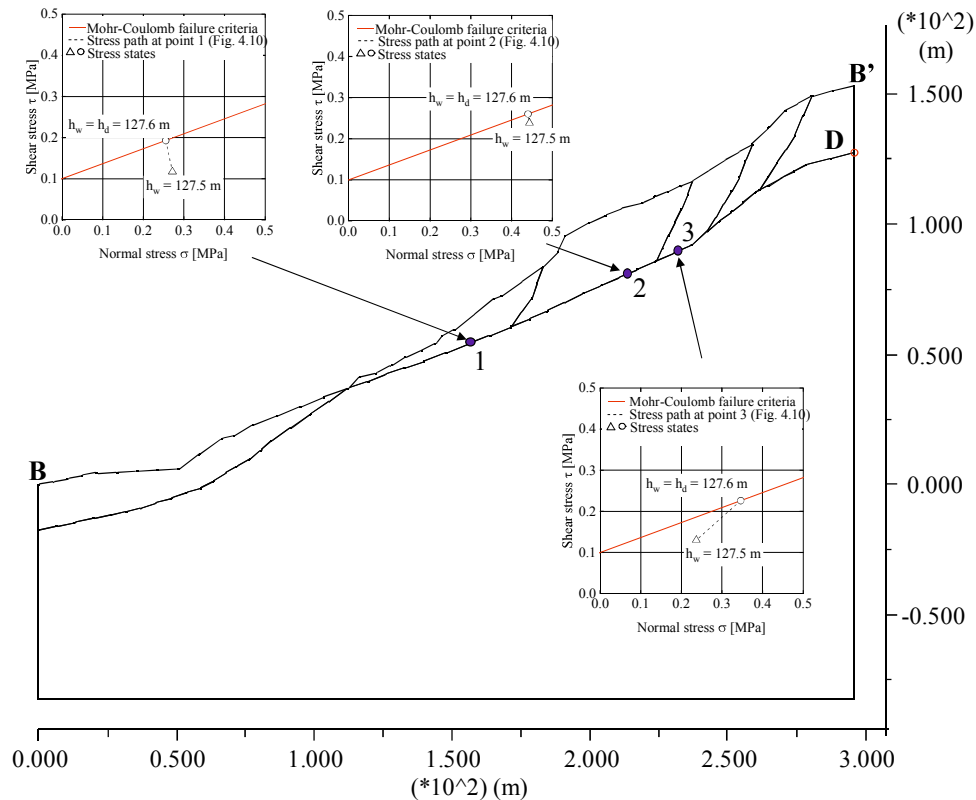
Fig. 4.13. Stress path at points 1, 2, and 3 on boundary between rhyolite and granite.

Fig. 4.13 shows the stress path at points 1, 2, and 3. The stress states at all points stay within the Mohr – Coulomb failure criteria and do not reach them when the water level on the right-hand side is lower than discontinuity point D (Case 1). The water level on the right-hand side rises up to discontinuity point D (Case 2), and the stress levels at points 1, 2, and 3 reach the Mohr – Coulomb failure criteria.

Fig. 4.14 shows the displacements and joint states in Cases 1 and 2. The light magenta line represents part of the slipped discontinuity, which is located on the boundary between the granite and the rhyolite. In Case 2, the slope above the discontinuity moves downward, and large displacement develops on the upper block (Fig. 4.14).

(a)   (b)
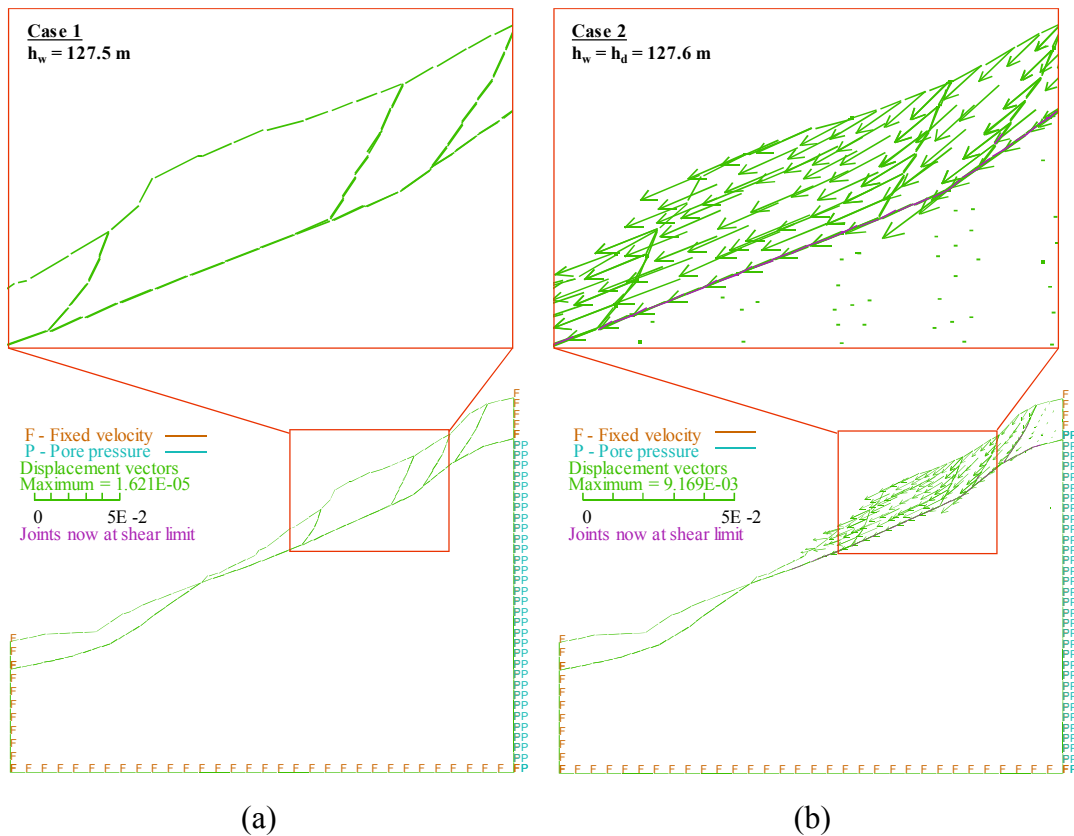
Fig. 4.14. Displacement distribution: (a) Case 1: h_w = 127.5 m and (b) Case 2: h_w = h_d = 127.6 m.

Similarly, Fig. 4.15 represents the velocity vectors and joint states in Cases 1 and 2. In Case 1, small movements were generated with the maximum of the velocity vectors by 3.175 x 10^{-5} m/s (Fig. 4.15a). However, the magnitude of the velocity

60

vectors increased significantly. The maximum of the velocity vectors is approximately 10 times higher than that in Case 1 (Fig. 4.15b).

Fig. 4.16 shows the displacement contours in Case 2. It can be clearly seen that large displacements distribute on the upper block in both horizontal and vertical directions.

From the numerical simulation, it is found that the water pressure in the discontinuity increases after the heavy rainfall, the stress on it reaches the Mohr – Coulomb failure criteria, some parts of the discontinuity slip, and finally the surface displacement of the slope significantly increases.

(a)   (b)
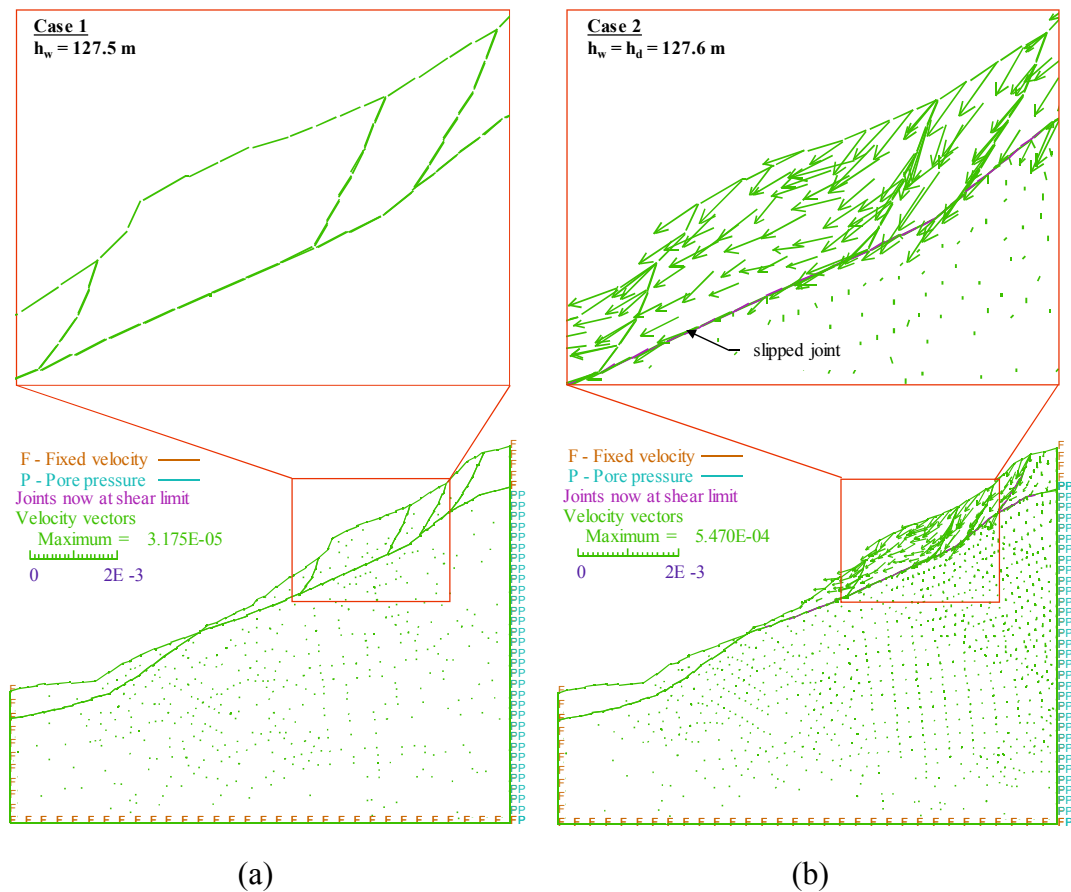
Fig. 4.15. Velocity vectors: (a) Case 1: $h_w = 127.5$ m and (b) Case 2: $h_w = h_d = 127.6$ m.
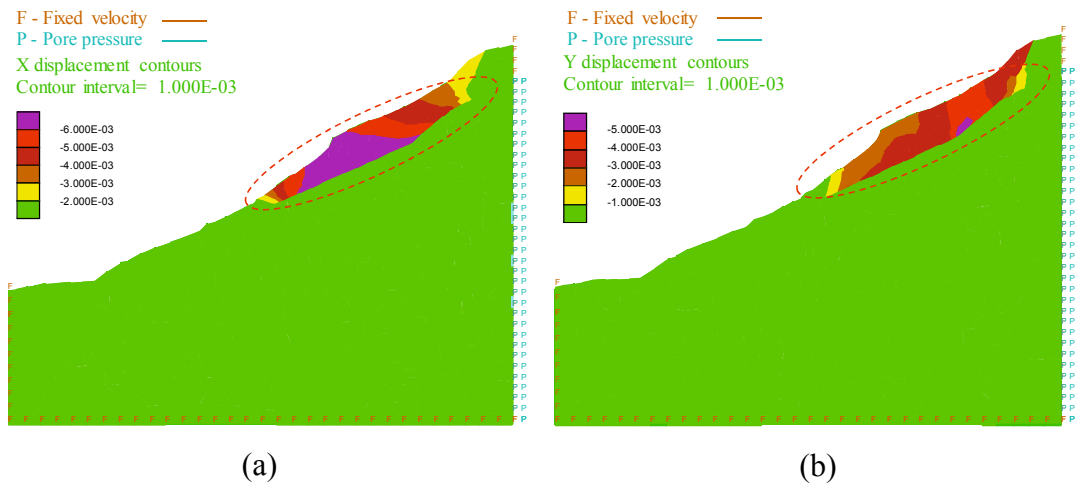
Fig. 4.16. Displacement contours in Case 2: (a) X (horizontal) displacement and (b) Y (vertical) displacement.

4.4. Chapter summary

In this chapter, continuous displacement monitoring was conducted at a large-scale steep slope by using the GPS displacement monitoring system and the proposed procedure to enhance the accuracy, as described in Chapter 3. Then, the mechanism of the displacement behavior was discussed by considering the monitoring results and the groundwater level. The following conclusions can be drawn:

(1) Three-dimensional displacements were continuously monitored every hour without missing any data for a period of 5 years using the proposed procedure to enhance the accuracy of the displacement monitoring, as described in Chapter 3. The GPS displacement monitoring system was able to detect small gradual increases in displacement with average velocities of 2-7 mm per month and a quick and large displacement of 183 mm occurring in one month due to heavy rainfall. In addition, changes in the direction of the displacement vector could be clearly found. This was useful information for assessing the stability evolution of the slope.

(2) A correlation between the increase in the GWL after rainfall and the occurrence of large displacements was recognized through long-term monitoring results. The mechanism of the displacement behavior due to the increase in the groundwater level was discussed using the monitoring results and the numerical simulations. The numerical analysis was successfully

conducted to reveal the possibility of the occurrence of large displacement due to the increase in the groundwater level.

(3) It was found that a rise in the GWL is a trigger to the occurrence of large slope displacements. In other words, when the groundwater level increases, the water pressure rises, the stress levels reach the failure criteria, and then large slope displacements occur.

Chapter 5

INVESTIGATION OF THE MEASUREMENT PERFORMANCE OF
THE NEW GPS SENSORS

5.1. Introduction

In order to conduct GPS monitoring more effectively, a sensor should be installed at many points, and it should be able to monitor displacement at any interval. New GPS sensors (prototypes) have been developed through a collaboration of the Shimizu Lab. (Yamaguchi University) and a manufacturer. In this chapter, the measurement performance of the new GPS sensors is investigated, and the kinematic method is employed to reduce the measurement interval. Fundamental and field experiments are conducted to obtain the standard deviation of the sensors.

5.2. New sensors

Fig. 5.1 shows the GPS sensors for displacement monitoring. The current sensor, MG31 (Furuno Electric Co. Ltd), with a flat antenna (Fig. 5.1a) (Masunari et al., 2003), was employed in the study described in Chapters 3 and 4. It is often used to monitor displacement, and has the accuracy of 1–2 mm in the horizontal direction and 3–4 mm in the vertical one (Shimizu et al., 2011; Shimizu and Nakashima, 2017). The price of the sensor and the monitoring system are still expensive compared to standard geotechnical instruments (e.g., extensometers).

New sensors (prototypes), SB-50S and SB-35, are being developed by a collaboration of Shimizu Lab. and a manufacturer (see Figs. 5.1b and 5.1c). It is expected that the price of the new sensors will be lower compared to MG31. On the other hand, since the sensors use a GPS module, which is often used for navigation and differential GPS, the accuracy is not clear for precise displacement monitoring. Table 5.1 shows the specifications of the new sensors. Basically, these two sensors are the same in that they use a U-blox GPS module with the L1 frequency of 1575.42 MHz and an update rate of 1 Hz. The difference between them is that SB-35 allows for the performance of the real-time kinematic method by a radio link of 920 MHz, while SB-

50S uses the post-kinematic method. To conduct real-time kinematic monitoring, the measurement data from the reference point are transmitted to the observation point in real-time.

In order to investigate the standard deviations of the new GPS sensors for displacement monitoring, experiments were conducted, as shown in Fig. 5.2. The experiment cases are shown in Table 5.2.
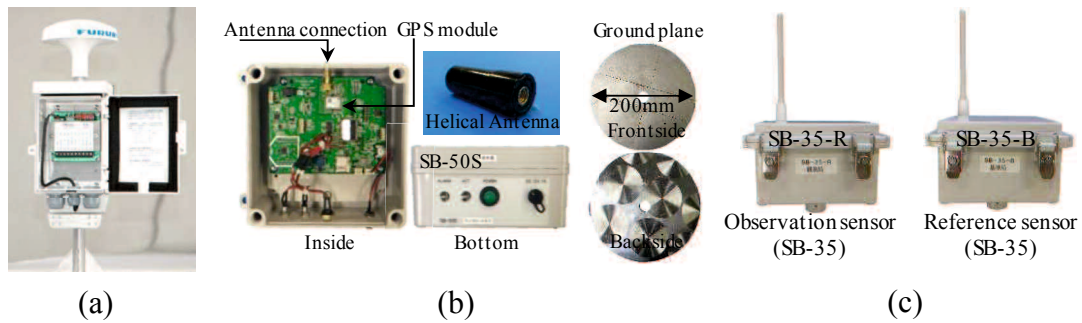
Fig. 5.1. GPS sensors: (a) MG31 with flat antenna, (b) SB-50S with helical antenna and ground plane (Terada, 2017), and (c) SB-35 with Tallysman TW-1421 and 920 Mhz radio link.

Table 5.1. Specifications of new sensors.

	SB-50S	SB-35
Antenna	Helical antenna and ground plane	Tallysman TW-1421
GPS module	U-blox NEO-6T-0	U-blox NEO-M8T
Frequency	L1, 1575.42 MHz	L1, 1575.42 MHz
Update rate	1 Hz	1 Hz
Power supply	DC 5V ~ 30V	DC 5V ~ 30V
Radio link	None	920 Mhz
Data acquisition	SD card (max.: 32 GB)	SD card (max.: 32 GB)
Dimensions (l x w x h)	150 x 150 x 75 (mm)	150 x 150 x 123 (mm)
Working temperature	-20ºC ~ 70ºC	-20ºC ~ 70ºC
Weight (approx.)	500 g	500 g
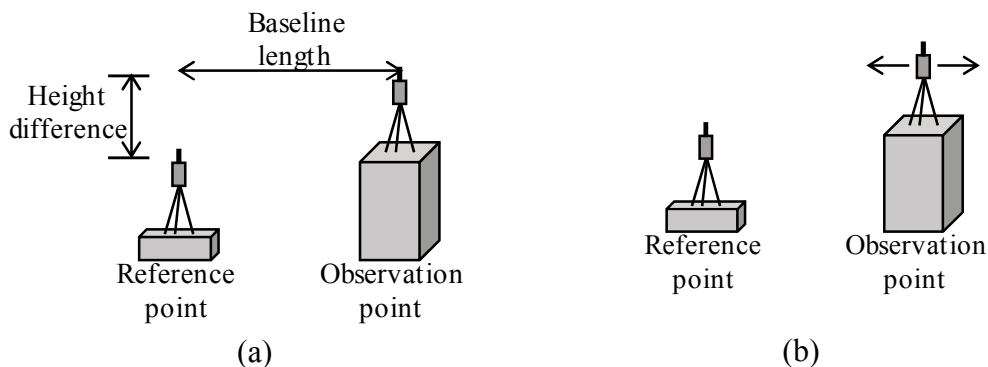
Fig. 5.2. Schematic of experiments using SB-50S and SB-35 (adapted from Terada, 2017): (a) Fundamental experiments and (b) Experiment for detecting displacement.

Table 5.2. Experiment cases.

Experiments		Baseline length (m)	Height difference (m)	Sensor	Duration
Fundamental experiments	Case 1	10	0	SB-50S	7 hours
	Case 2	200	30	SB-35	3 hours
Experiments for detecting displacement		10	0	SB-50S	4 hours
				SB-35	4 hours

Note: Baseline length and height difference are approximate values.

5.3. Fundamental experiments

Experiments were conducted for two cases using the new GPS sensors, SB-50S and SB-35 (Fig. 5.3). In Case 1, the baseline length between the reference point and the monitoring point is 10 m, and the difference in height is approximately 0 m. In Case 2, the baseline length is 200 m, and difference in height is approximately 30 m. The experiments were conducted using the same pair of sensors at the Tokiwa Campus of Yamaguchi University without any obstacles above the antennas.

(a)   (b)

Fig. 5.3. GPS sensors: (a) SB-50S and (b) SB-35.

5.3.1. Baseline length: 10 m, height difference: 0 m

Figs. 5.4 and 5.5 show the measurement results in Case 1 (a 10-m baseline length and an approximately 0-m height difference) by SB-50S and SB-35, respectively. The standard deviations of the kinematic analysis with the 1-second measurement interval are 3-4 mm in the horizontal direction and 7-8 mm in the vertical one, while those of the static analysis with the 1-hour interval are about 1-2 mm in the horizontal direction and 2-3 mm in the vertical one. The results of the kinematic analysis are too poor to precisely monitor displacements. This shortcoming is well known fact (Shimizu et al., 1997).

In order to improve the accuracy, the arithmetic average of the kinematic results is calculated. The average periods are 1 minute, and 5, 10, 20, 30, and 60 minutes. The average results are shown in Figs. 5.4b-g and 5.5b-g. The standard deviations of the 60-minute average results are almost the same as those of the 1-hour static results. When the 10-20-minute average is taken, the standard deviations become half of those of the 1-second kinematic results. It is found that the standard deviations are improved by taking the average of the kinematic results.
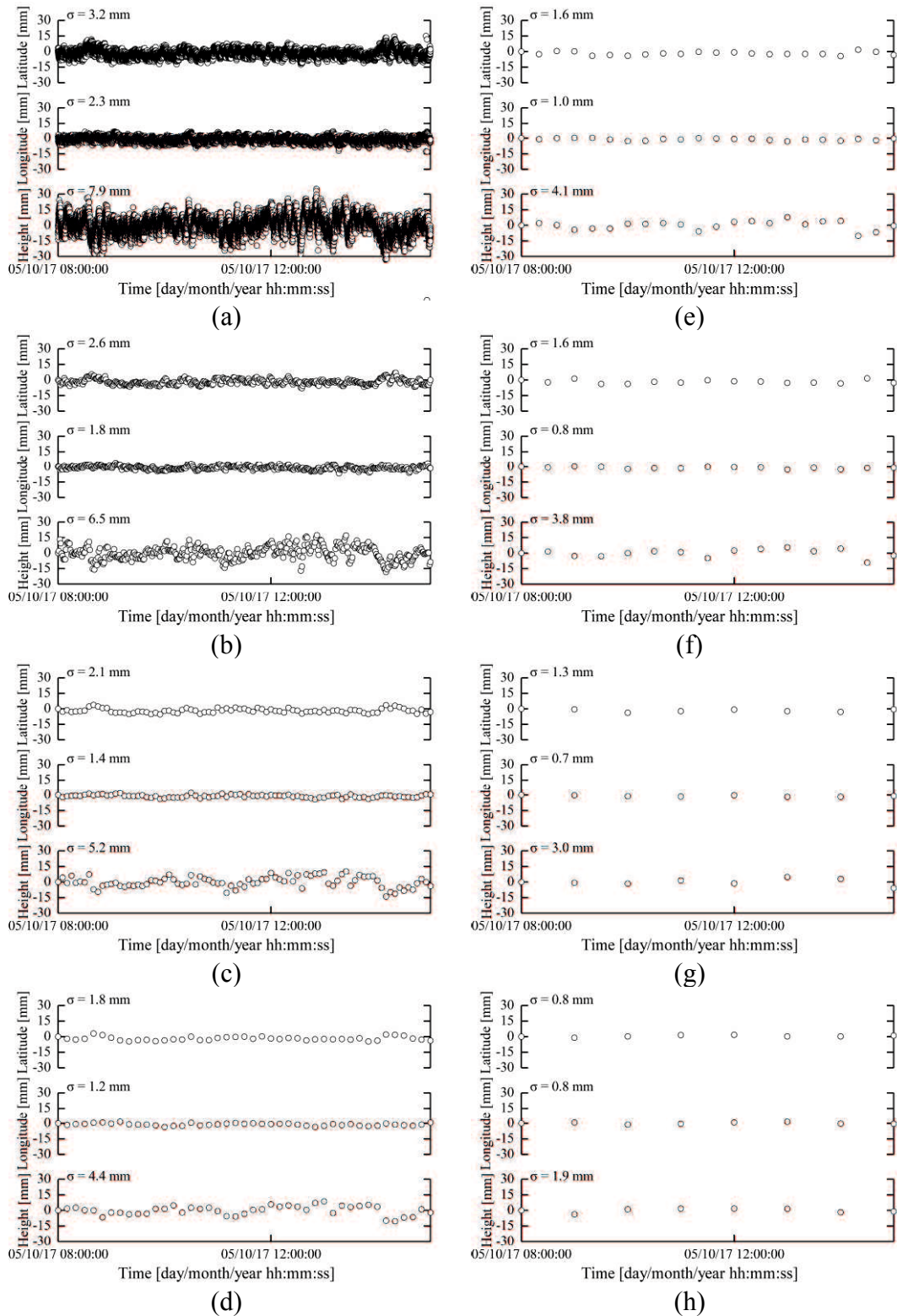
Fig. 5.4. Measurement results by SB-50S (baseline length: 10 m, height difference: 0 m): (a) Post kinematic results with measurement interval of 1 second, (b) 1-minute average of kinematic results, (c) 5-minute average of kinematic results, (d) 10-minute average of kinematic results, (e) 20-minute average of kinematic results, (f) 30-minute average of kinematic results, (g) 60-minute average of kinematic results, and (h) Static analysis with 1-hour observation.
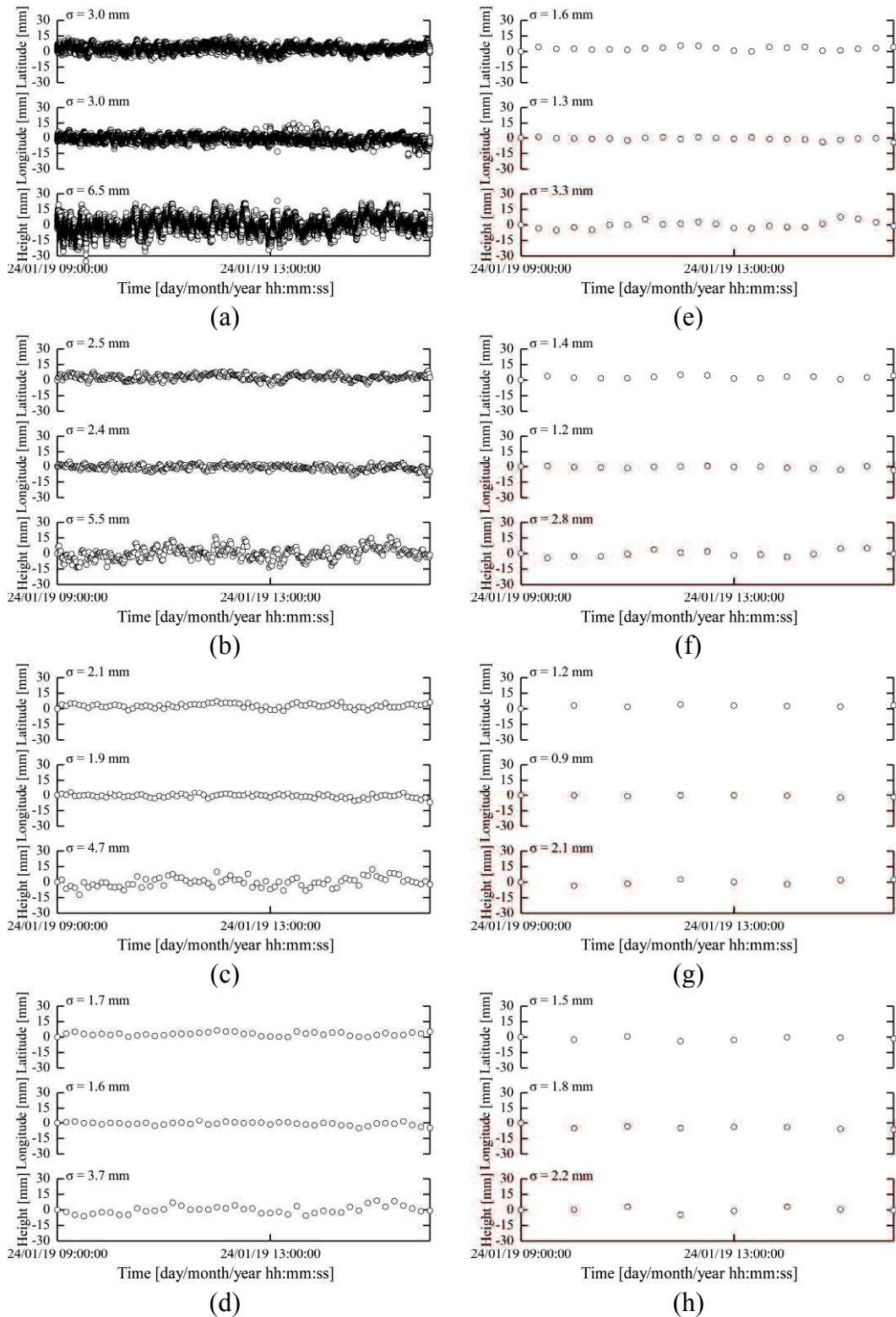
Fig. 5.5. Measurement results by SB-35 (baseline length: 10 m, height difference: 0 m): (a) Real-time kinematic results with measurement interval of 1 second, (b) 1-minute average of kinematic results, (c) 5-minute average of kinematic results, (d) 10-minute average of kinematic results, (e) 20-minute average of kinematic results, (f) 30-minute average of kinematic results, (g) 60-minute average of kinematic results, and (h) Static analysis with 1-hour observation.

5.3.2. Baseline length: 200 m, height difference: 30 m

Figs. 5.6 and 5.7 show the measurement results in Case 2 (a 200-m baseline length and an approximately 30-m height difference) by SB-50S and SB-35, respectively. The standard deviations of the kinematic analysis with the 1-second measurement interval are 3-4 mm in the horizontal direction and 8-9 mm in the vertical one, while those of the static analysis with the 1-hour interval are about 1-2 mm in the horizontal direction and 2-3 mm in the vertical one. The same arithmetic average of the kinematic results, as described in section 5.3.1, is also calculated. The average results are shown in Figs. 5.6b-g and 5.7b-g. The standard deviations of the 60-minute average results are almost the same as those of the 1-hour static results. Similar improvements, as discussed in section 5.3.1, are found in the standard deviations.

Table 5.3 summarizes the standard deviations obtained by SB-50S and SB-35 in the fundamental experiments. Figs. 5.8 and 5.9 show the relationship between the average periods and the standard deviations in the fundamental experiments. It can be seen that the new sensors were able to obtain certain standard deviations, 1-2 mm in the horizontal direction and 2-3 mm in the vertical one, using the static analysis with the 1-hour interval or taking the average over 60 minutes of the kinematic results. If a lower accuracy (standard deviations) is acceptable for monitoring, the interval can be shortened by taking the average of the kinematic results over 10-30 minutes.
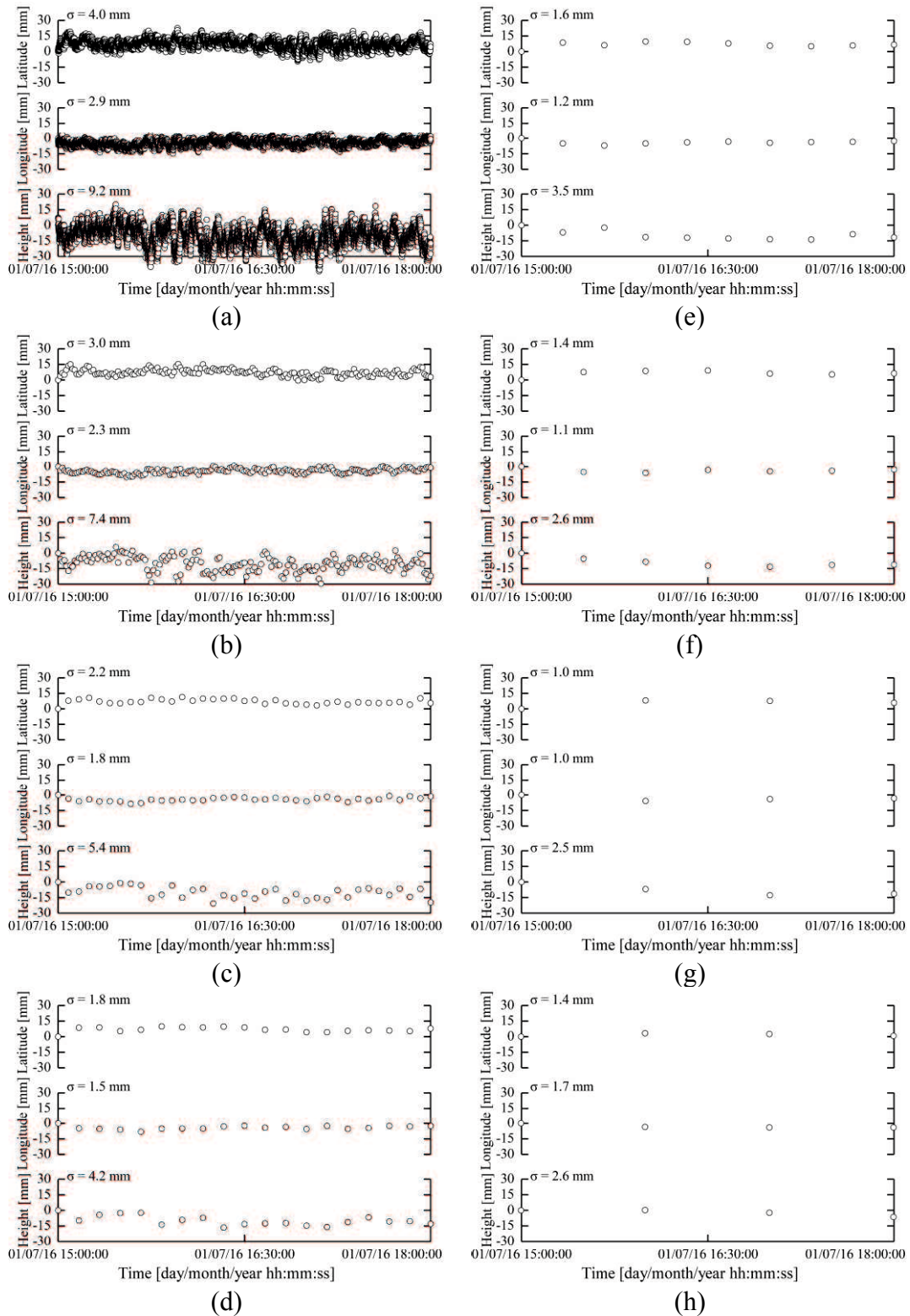
Fig. 5.6. Measurement results by SB-50S (baseline length: 200 m, height difference: 30 m): (a) Post kinematic results with measurement interval of 1 second, (b) 1-minute average of kinematic results, (c) 5-minute average of kinematic results, (d) 10-minute average of kinematic results, (e) 20-minute average of kinematic results, (f) 30-minute average of kinematic results, (g) 60-minute average of kinematic results, and (h) Static analysis with 1-hour observation.
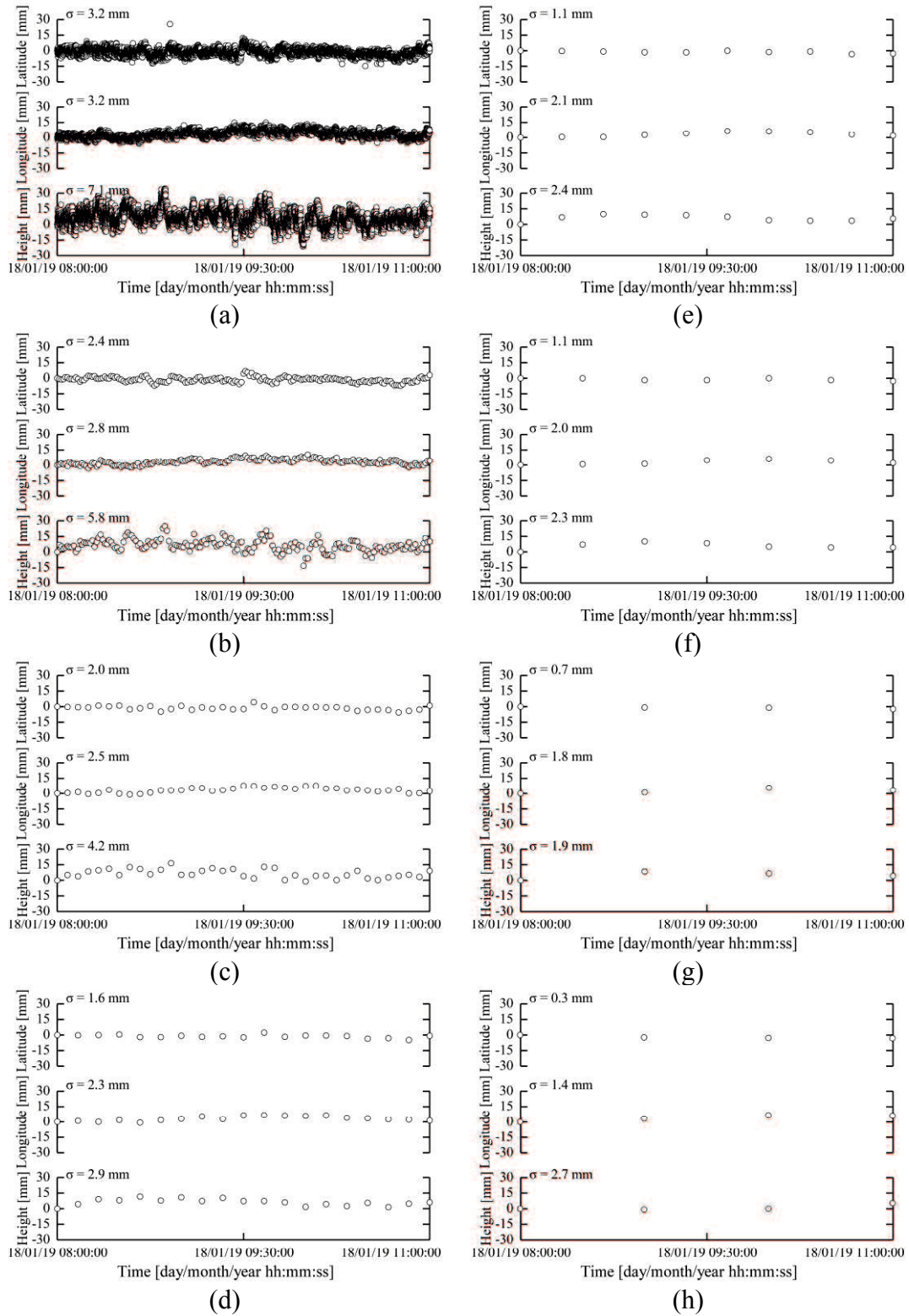
Fig. 5.7. Measurement results by SB-35 (baseline length: 200 m, height difference: 30 m): (a) Real-time kinematic results with measurement interval of 1 second, (b) 1-minute average of kinematic results, (c) 5-minute average of kinematic results, (d) 10-minute average of kinematic results, (e) 20-minute average of kinematic results, (f) 30-minute average of kinematic results, (g) 60-minute average of kinematic results, and (h) Static analysis with 1-hour observation.

Table 5.3. Standard deviations (fundamental experiments).

Baseline length (m)	Height difference (m)	Sensor	Direction	Standard deviations by static analysis (mm)	Standard deviations of kinematic result with measurement interval 1 second, and 1, 5, 10, 20, 30, 60 minutes average of kinematic result (mm)						
					1 second	1 minute	5 minutes	10 minutes	20 minutes	30 minutes	60 minutes
10	0	SB-50S	Latitude	0.8	3.2	2.6	2.1	1.8	1.6	1.6	1.3
			Longitude	0.8	2.3	1.8	1.4	1.2	1.0	0.8	0.7
			Height	1.9	7.9	6.5	5.2	4.4	4.1	3.8	3.0
		SB-35	Latitude	1.5	3.0	2.5	2.1	1.7	1.6	1.4	1.2
			Longitude	1.8	3.0	2.4	1.9	1.6	1.3	1.2	0.9
			Height	2.2	6.5	5.5	4.7	3.7	3.3	2.8	2.1
200	30	SB-50S	Latitude	1.4	4.0	3.0	2.2	1.8	1.6	1.4	1.0
			Longitude	1.7	2.9	2.3	1.8	1.5	1.2	1.1	1.0
			Height	2.6	9.2	7.4	5.4	4.2	3.5	2.6	2.5
		SB-35	Latitude	0.3	3.2	2.4	2.0	1.6	1.1	1.1	0.7
			Longitude	1.4	3.2	2.8	2.5	2.3	2.1	2.0	1.8
			Height	2.7	7.1	5.8	4.2	2.9	2.4	2.3	1.9

(a)
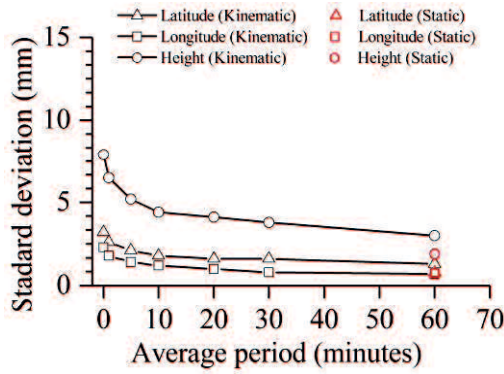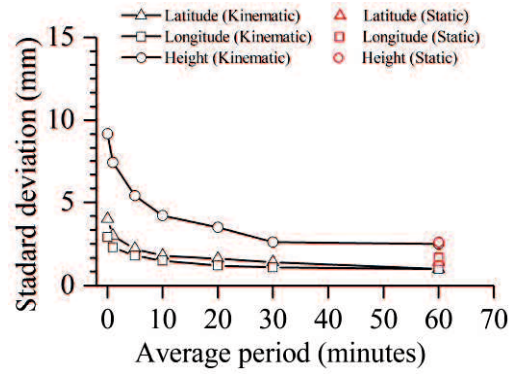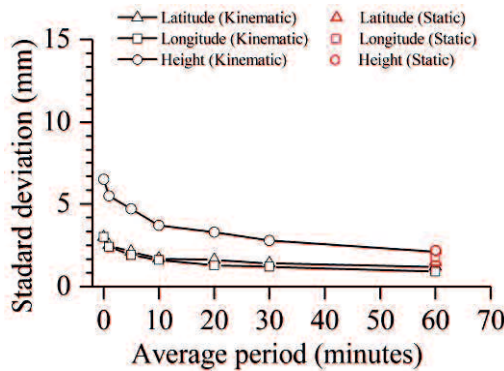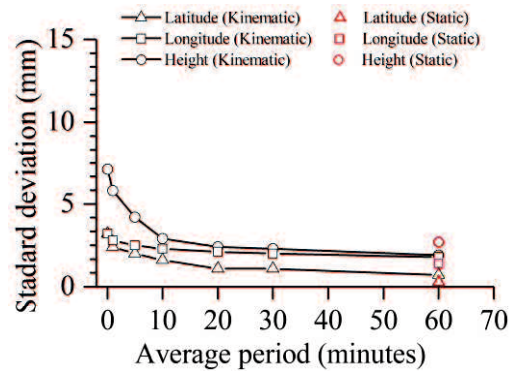
(b)

Fig. 5.8. Relationship between average periods and standard deviations (baseline length: 10 m, height difference: 0 m): (a) SB-50S and (b) SB-35.

(a)

(b)

Fig. 5.9. Relationship between average periods and standard deviations (baseline length: 200 m, height difference: 30 m): (a) SB-50S and (b) SB-35.

73

5.4. Experiments for detecting displacements

In order to verify the reliability of the new GPS sensors, experiments for detecting displacements were performed by applying given displacements to the sensors. Fig. 5.10 shows the slider that was used to cause displacements by rotating a screw to move the sensor. The baseline length and the height difference were about 10 m and 0 m, respectively.
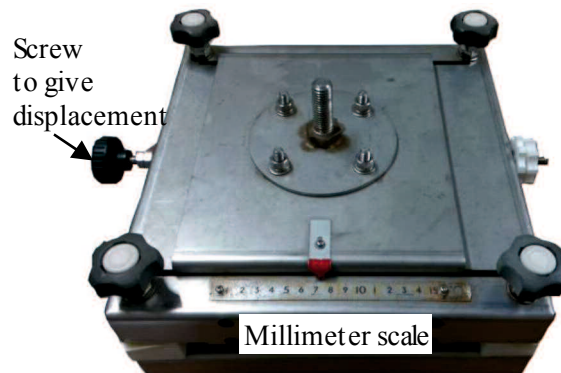
Fig. 5.10. Slider to simulate displacement.

5.4.1. New GPS sensor SB-50S

Figs. 5.11 and 5.12 show the measurement results for the cases of given displacements of 10 mm and 5 mm in the latitude direction, respectively. According to section 5.3, standard deviations are improved to half of those of the 1-second kinematic results when taking the average over 10-20 minutes, and almost the same as those of the 1-hour static results when taking the average over 60 minutes. The average for the 1-second kinematic results are taken for periods of 10, 20, 30, and 60 minutes. The average results are shown in Figs. 5.11b-e and 5.12b-e.

Table 5.4 shows the results for the detection of displacements by SB-50S. Although there are discrepancies of 0.1-1.8 mm between the detected and the given displacements, SB-50S allows for the detection of the 10-mm given displacement at shorter intervals, namely, 10, 20, and 30 minutes, as compared to 60 minutes. In the case of the given displacement of 5 mm, the maximum discrepancy is 2.0 mm. Therefore, it is not effective to detect such a small displacement as 5 mm with this sensor.
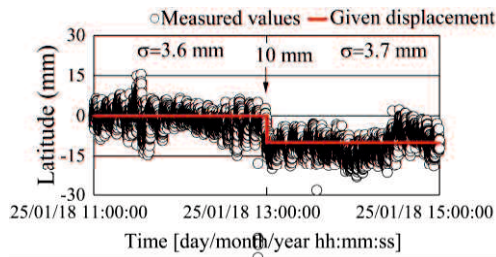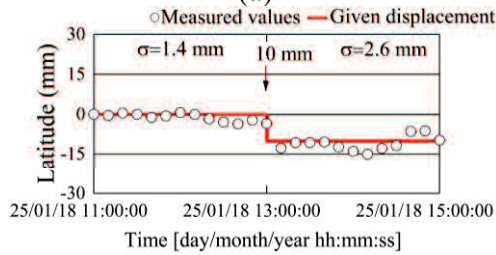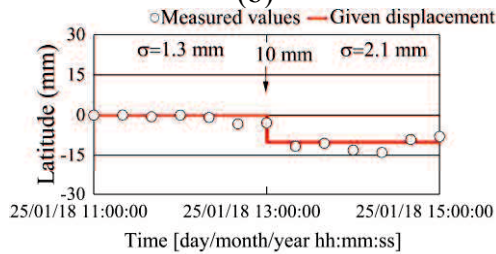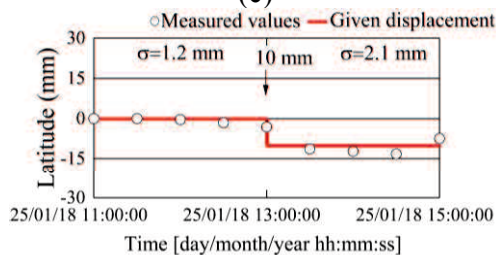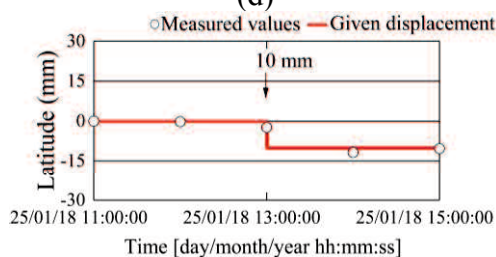
Fig. 5.11. Measurement results by SB-50S (10-mm given displacement in latitude): (a) Post kinematic results with measurement interval of 1 second, (b) 10-minute average of kinematic results, (c) 20-minute average of kinematic results, (d) 30-minute average of kinematic results, and (e) 60-minute average of kinematic results.
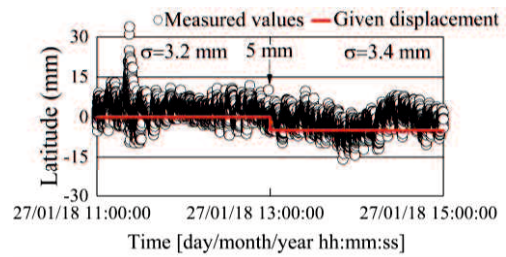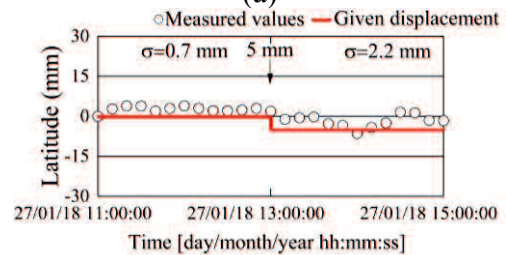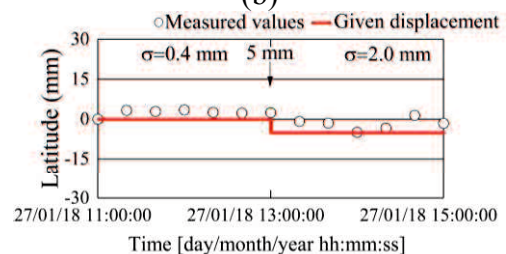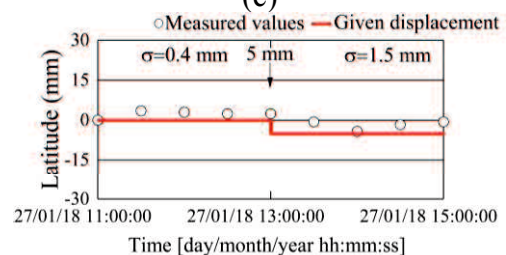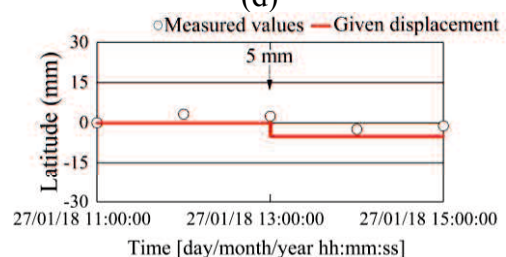
Fig. 5.12. Measurement results by SB-50S (5-mm given displacement in latitude): (a) Post kinematic results with measurement interval of 1 second, (b) 10-minute average of kinematic results, (c) 20- minute average of kinematic results, (d) 30-minute average of kinematic results, (e) 60-minute average of kinematic results.

Table 5.4. Detection of displacement (SB-50S).

Detected displacement by taking average of kinematic results (mm)	10 minutes	20 minutes	30 minutes	60 minutes	10 minutes	20 minutes	30 minutes	60 minutes
	9.2	8.8	8.2	9.4	3.0	3.3	3.1	4.9
Given displacements in Latitude (mm)	10.0				5.0			
Discrepancy (mm)	0.8	1.2	1.8	0.6	2.0	1.7	1.9	0.1

5.4.2. New GPS sensor SB-35

Figs. 5.13 and 5.14 show the measurement results for the cases of given displacements of 10 mm and 2 mm in the longitude direction, respectively. The average for the 1-second kinematic measurement results are also taken for periods of 10, 20, 30, and 60 minutes. The average results are shown in Figs. 5.13b-e and 5.14b-e.

Table 5.5 shows the results for the detection of displacements by SB-35. Although there are discrepancies of 0.1–1.5 mm between the detected and the given displacements, SB-35 also allows for the detection of the 10-mm given displacement at shorter intervals, namely, 10, 20, and 30 minutes, as compared to 60 minutes. In the case of the given displacement of 2 mm, the maximum discrepancy is 2.5 mm. Therefore, it is not effective to detect such a small displacement as 2 mm with this sensor.
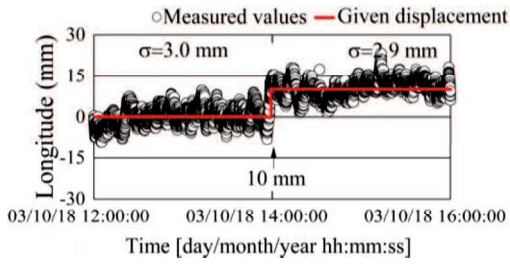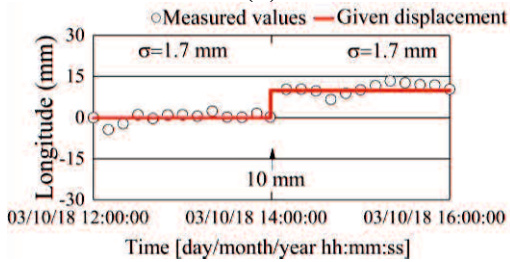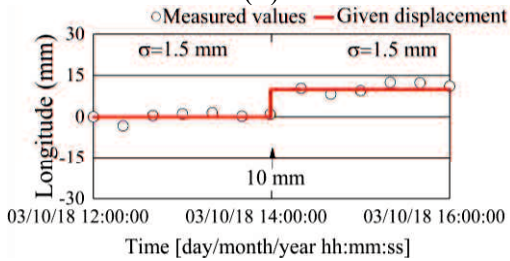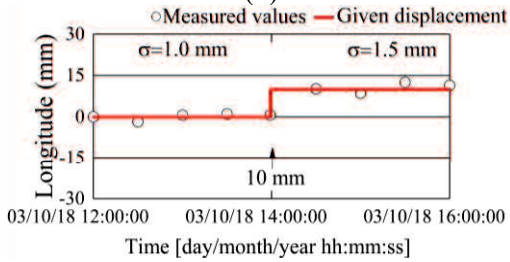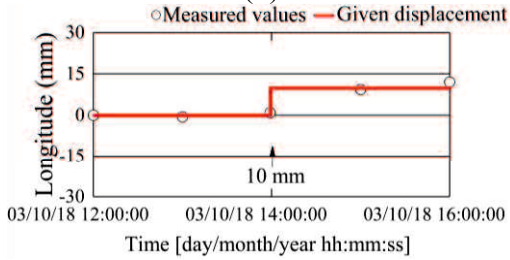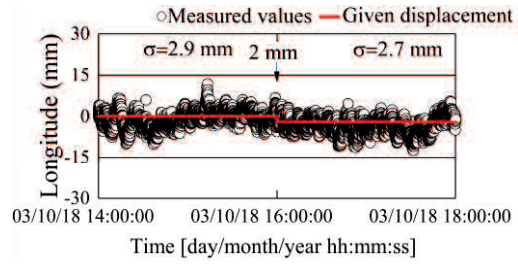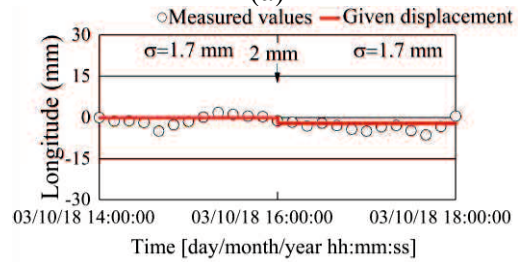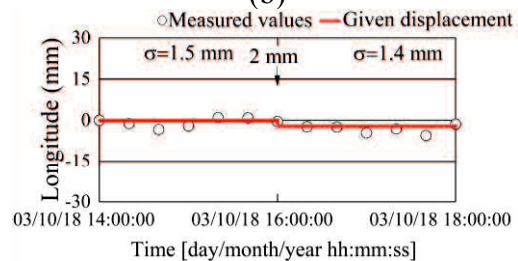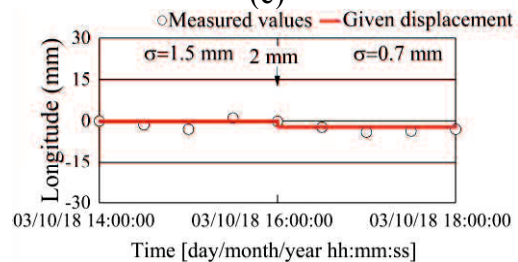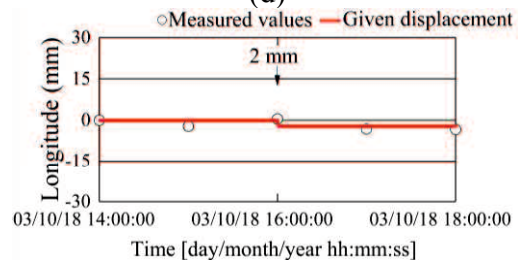
Fig. 5.13. Measurement results by SB-35 (10-mm given displacement in longitude): (a) Real-time kinematic results with measurement interval of 1 second, (b) 10-minute average of kinematic results, (c) 20-minute average of kinematic results, (d) 30-minute average of kinematic results, (e) 60-minute average of kinematic results.

Fig. 5.14. Measurement results by SB-35 (2-mm given displacement in longitude): (a) Real-time kinematic results with measurement interval of 1 second, (b) 10-minute average of kinematic results, (c) 20-minute average of kinematic results, (d) 30-minute average of kinematic results, (e) 60-minute average of kinematic results.

Table 5.5. Detection of displacement (SB-35).

Detected displacement by taking average of kinematic results (mm)	10 minutes	20 minutes	30 minutes	60 minutes	10 minutes	20 minutes	30 minutes	60 minutes
	10.1	9.4	9.5	8.5	0.5	1.9	2.1	4.5
Given displacements in Longitude (mm)	10.0				2.0			
Discrepancy (mm)	0.1	0.6	0.5	1.5	1.5	0.1	0.1	2.5

5.5. Field experiments

Under the condition at the Tokiwa Campus of Yamaguchi University, the new GPS sensors show a potential to monitor displacements. Therefore, field experiments were conducted with these sensors, SB-50S and SB-35, at the same slope where the current one, MG31, has been in use. Fig. 5.15 shows the locations of the new GPS sensors. Two reference sensors, SB-50S-1 and SB-35-1, were installed in the lower area of the slope, while two observation sensors, SB-50S-2 and SB-35-2, were installed in the upper area of the slope.
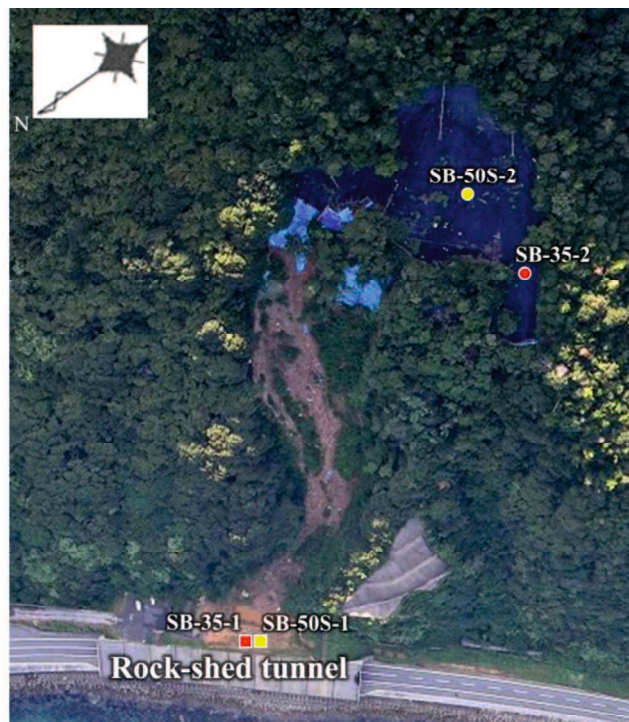
Fig. 5.15. Monitoring site and locations of new GPS sensors.

Fig. 5.16. Reference points: (a) SB-50S-1 and (b) SB-35-1 (b); Observation points: (c) SB-50S-2 and (d) SB-35-2.
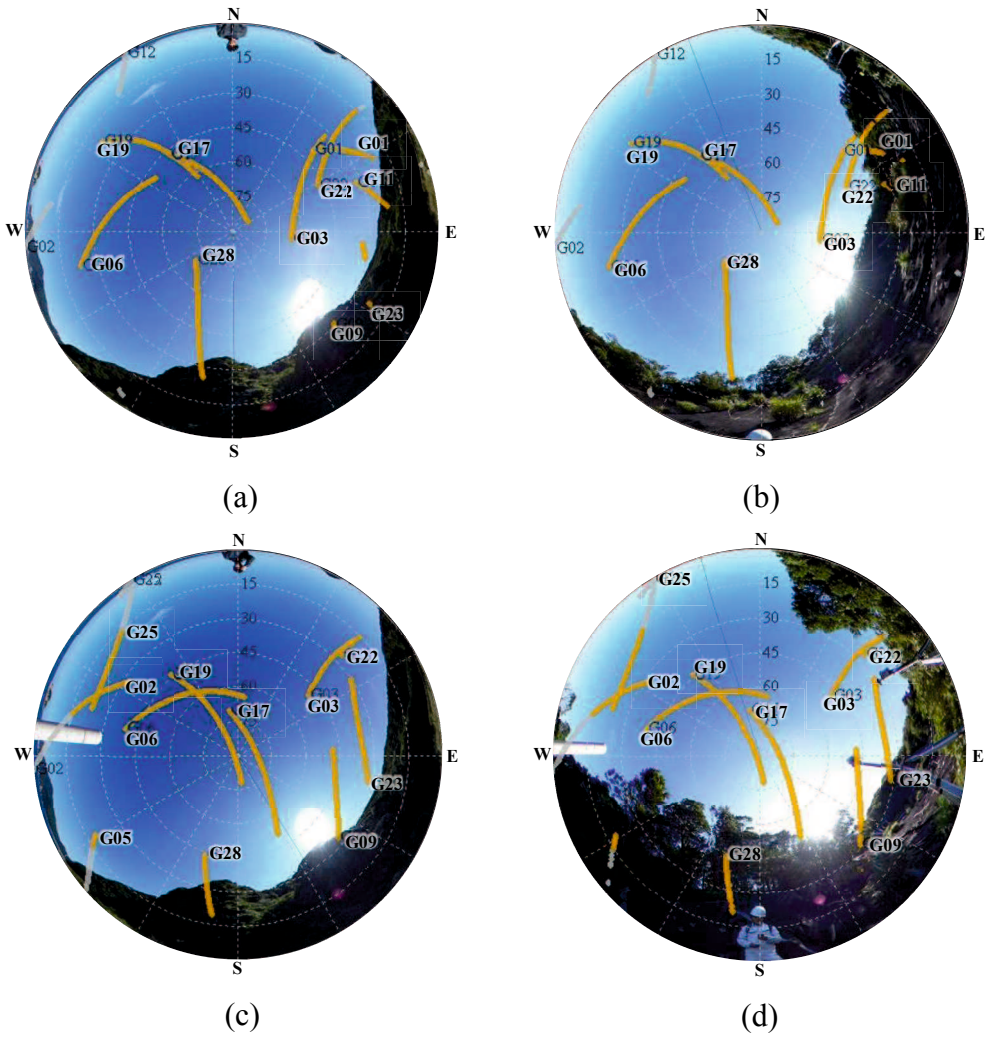
Fig. 5.17. Sky views and trace of satellite orbits above antennas at: (a) SB-50S-1, (b) SB-50S-2, (c) SB-35-1, and (d) SB-35-2.

The baseline length and the height difference between SB-50S-1 and SB-50S-2 are 181 m and 100 m, respectively. The baseline length and the height difference between SB-35-1 and SB-35-2 are 170 m and 91 m, respectively. Fig. 5.16 shows the reference and observation points, while Fig. 5.17 shows the sky views above the antennas.

5.5.1. Kinematic results
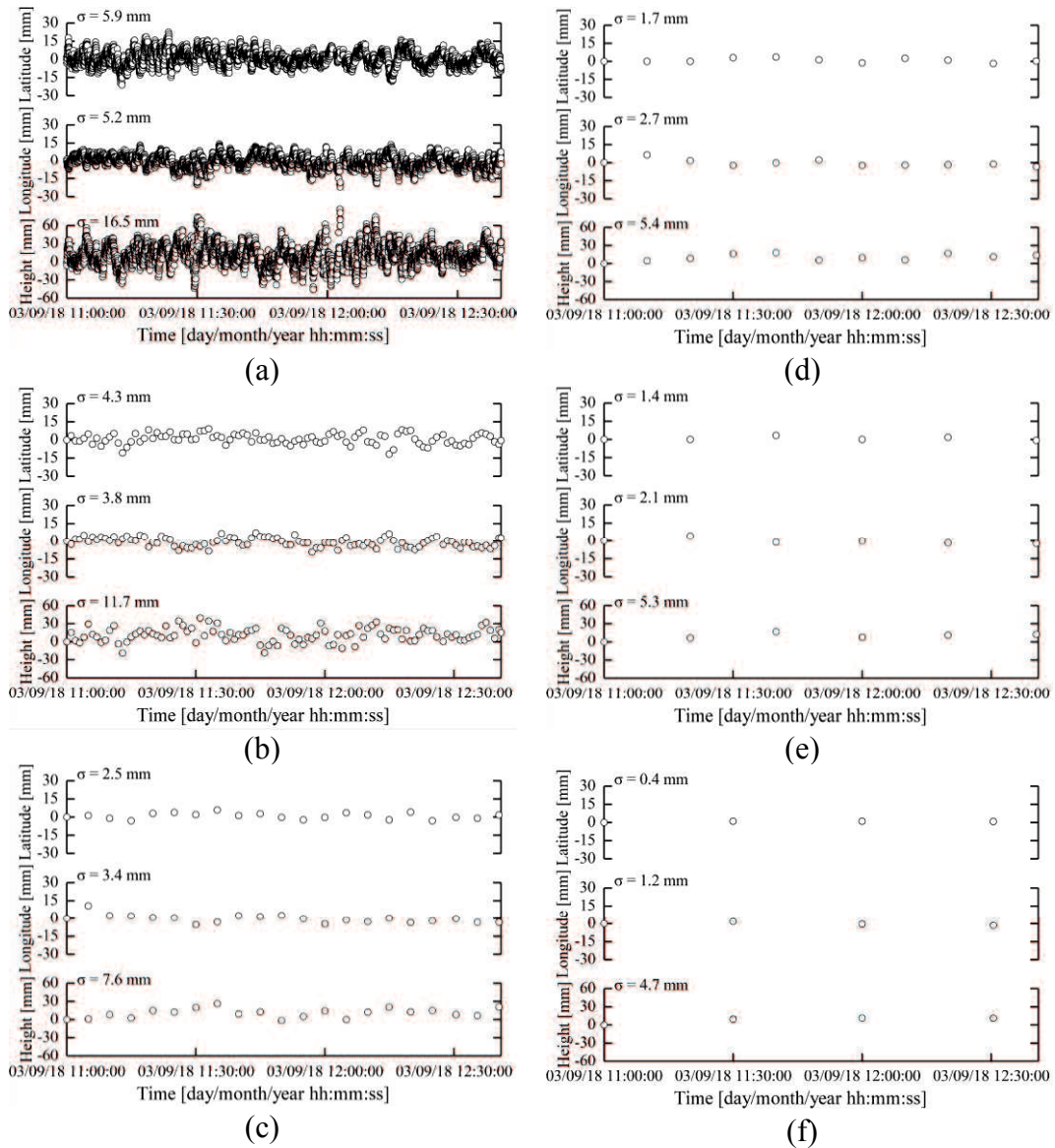
Fig. 5.18. Measurement results by SB-50S (baseline length: 181 m, height difference: 100 m): (a) Post kinematic results with measurement interval of 1 second, (b) 1-minute average of kinematic results, (c) 5-minute average of kinematic results, (d) 10-minute average of kinematic results, (e) 20-minute average of kinematic results, and (f) 30-minute average of kinematic results.

80
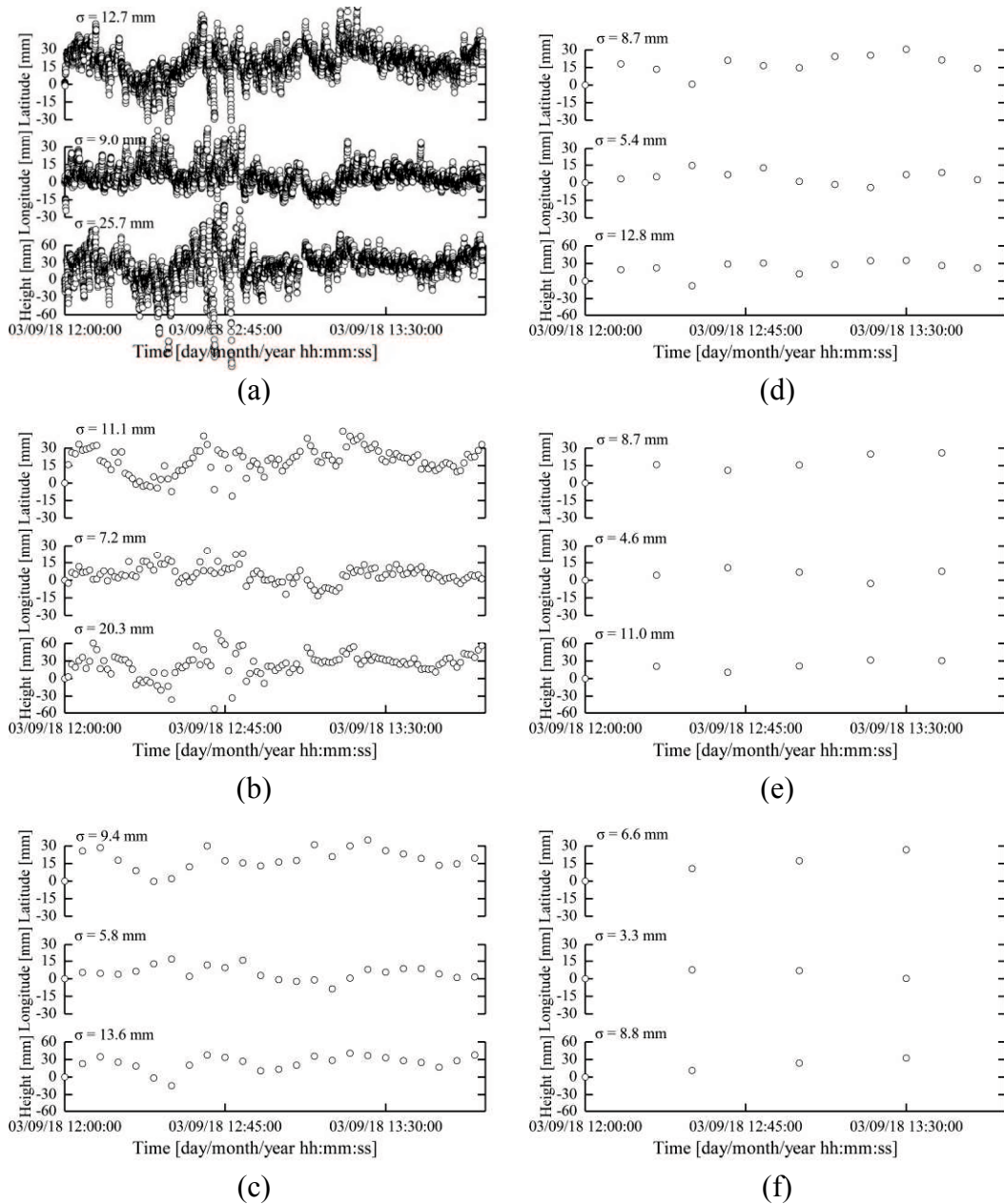
Fig. 5.19. Measurement results by SB-35 (baseline length: 170 m, height difference: 91 m): (a) Real-time kinematic results with measurement interval of 1 second, (b) 1-minute average of kinematic results, (c) 5-minute average of kinematic results, (d) 10-minute average of kinematic results, (e) 20-minute average of kinematic results, and (f) 30-minute average of kinematic results.

Figs. 5.18 and 5.19 show the measurement results by SB-50S and SB-35, respectively. The standard deviations of the kinematic analysis with 1-second measurement interval are 5.9 mm in latitude, 5.2 mm in longitude, and 16.5 mm in height by SB-50S. They are 12.7 mm in latitude, 9.0 mm in longitude, and 25.7 mm in height, respectively, by SB-35 (Table 5.6).

Table 5.6. Standard deviations (field experiments).

Baseline length (m)	Height difference (m)	Sensor	Direction	Standard deviations of kinematic result with measurement interval 1 second, and 1, 5, 10, 20, 30 minutes average of kinematic result (mm)					
				1 second	1 minute	5 minutes	10 minutes	20 minutes	30 minutes
181	100	SB-50S	Latitude	5.9	4.3	2.5	1.7	1.4	0.4
			Longitude	5.2	3.8	3.4	2.7	2.1	1.2
			Height	16.5	11.7	7.6	5.4	5.3	4.7
170	91	SB-35	Latitude	12.7	11.1	9.4	8.7	8.7	6.6
			Longitude	9.0	7.2	5.8	5.4	4.6	3.3
			Height	25.7	20.3	13.6	12.8	11.0	8.8

5.5.2. Interval of measurement time

The arithmetic average of the kinematic results in Figs. 5.18 and 5.19 is also calculated. The average periods are 1 minute, and 5, 10, 20, and 30 minutes. The average results are shown in Figs. 5.18b-f and 5.19b-f.

Table 5.6 and Fig. 5.20 show the relationships between the average periods and the standard deviations. When the average is 10-30 minutes, the standard deviations by SB-50S are almost the same as those by MG31, namely, 1-2 mm in the horizontal direction and 3-4 mm in the vertical one, as discussed in Chapter 3. Those by SB-35 are worse than those by MG31. This is because the observation sensors, SB-50S-2 and SB-35-2, were placed at different locations (see Fig. 5.15). The sky view above SB-35-2 is narrower than that above SB-50S-2 (see Figs. 5.17b and 5.17d). Therefore, the standard deviations by SB-35 are slightly worse than those by SB-50S.

(a) (b)
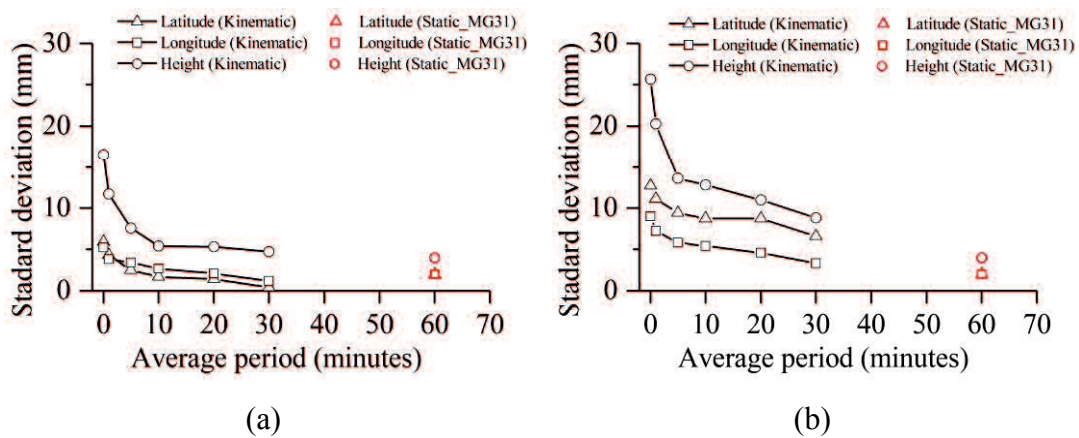
Fig. 5.20. Relationship between average periods and standard deviations (field experiments): (a) SB-50S and (b) SB-35.

5.6. Chapter summary

The performance of two new GPS sensors was investigated by using the kinematic method. Some experiments were conducted to verify the applicability and the reliability of the new sensors for displacement monitoring. The following conclusions can be drawn:

(1) The new sensors were able to obtain certain standard deviations, 1-2 mm in the horizontal direction and 2-3 mm in the vertical one, by using a static analysis with a 1-hour interval or taking the average over a period of 60 minutes of the kinematic results. The standard deviations were improved by taking the average of the kinematic results. If a lower accuracy (standard deviations) is acceptable for monitoring, the interval can be shortened by taking the average of the kinematic results over a period of 10-30 minutes.

(2) The new GPS sensors were able to detect the given displacement of 10 mm, while they were not effective for detecting smaller given displacements, such as 5 mm and 2 mm. By using the kinematic method and the arithmetic average of the kinematic results, the new sensors allowed for the detection of displacements at shorter intervals, namely, 10, 20, and 30 minutes, as compared to 60 minutes.

(3) Field experiments at the slope site also showed the applicability of the new GPS sensors for displacement monitoring. The standard deviations by SB-50S were almost similar to those by MG31, 1-2 mm in the horizontal direction and 3-4 mm in the vertical one, after taking the 1-second average of the kinematic results over a period of 10-30 minutes. The standard deviations by SB-35 were also improved by taking the 1-second average of the kinematic results.

Chapter 6
CONCLUSIONS

6.1. Conclusions

Continuous displacement monitoring plays an important role in assessing the stability of rock structures, such as slopes, etc., and in predicting future failures. The aim of this research was to establish a method for precise and continuous displacement monitoring by using GPS and to verify its application to a large-scale steep slope. To guarantee the reliability of the measurement results, a procedure with error-correction methods, to enhance the accuracy of the displacement monitored with GPS, was proposed, and its applicability for reducing and/or eliminating the errors for long-term monitoring at a large-scale steep slope was verified. Furthermore, the mechanism of the occurrence of large displacements at the slope, due to an increase in the groundwater level, was discussed in consideration of field measurements and numerical simulations. In addition, the measurement performance of new GPS sensors was investigated through the kinematic method.

Based on the objectives of this study and the above themes, the following conclusions can be drawn:

(1) The procedure with error-correction methods is effective for reducing and/or eliminating bias and random errors in the GPS displacement results. Furthermore, the procedure with error-correction methods was applied to the monitoring results obtained every hour for one month at a large-scale steep slope with a height difference of more than 100 m to enhance the accuracy of the displacement monitored with GPS. Although the original results were wavy and scattered, due to the effects of obstructions above certain antennas and tropospheric delays, the wavy and large scattered errors were removed, and the final results were smoothed with only small standard deviations, i.e., 1-2 mm in the horizontal direction and 3-4 mm in the vertical direction. It was proven that the above procedure was able to improve the original scattered monitoring results.

(2) The measurement sensitivity of the GPS displacement monitoring system was

found to be almost equivalent to that of extensometers and the Diffusion Laser Displacement Meter. Three-dimensional displacements were continuously monitored every hour without missing any data for a period of 5 years using the procedure with error-correction methods at the slope. The GPS displacement monitoring system was able to detect small gradual increases in displacement with average velocities of 2-7 mm per month and a quick large increase in displacement of 183 mm per month due to rainfall, as well as changes in the direction of the displacement vector. This was very useful information for assessing the stability evolution of the slope.

(3) A correlation between an increase in the groundwater level after rainfall and the occurrence of large displacements could be recognized in the long-term monitoring results. The mechanism of the occurrence of the large displacement due to the increase in the groundwater level was discussed by using monitoring results and numerical simulations. The numerical simulations were successfully conducted to reveal the possibility of the increase in large displacements due to the increase in the groundwater level. It was found that a rise in the GWL is a trigger to the occurrence of large displacements at the slope. When the groundwater level increased, the water pressure rose, and stress reached the failure criteria; then large displacements occurred at the slope.

(4) The new GPS sensors were able to obtain certain standard deviations, 1-2 mm in the horizontal direction and 2-3 mm in the vertical one, using the static analysis with a 1-hour interval or taking the average over a period of 60 minutes of the kinematic results. The standard deviations were improved by taking the average of the kinematic results. If a lower accuracy (standard deviations) is acceptable for monitoring, the measurement interval can be shortened by taking the average of the kinematic results over a period of 10-30 minutes. The new GPS sensors detected the small given displacement of 10 mm at shorter intervals, namely, 10, 20, and 30 minutes, as compared to 60 minutes. Field experiments at the slope site showed the applicability of the new GPS sensors for displacement monitoring. The standard deviations by SB-50S were almost similar to those by MG31, 1-2 mm in the horizontal direction and 3-4 mm in

the vertical one, after taking the 1-second average of the kinematic results over a period of 10-30 minutes. The standard deviations by SB-35 were also improved by taking the 1-second average of the kinematic results.

6.2. Future research

The numerical simulations provided one possibility for predicting the occurrence of large displacement due to the increase in the groundwater level. It will be necessary to compare the displacement results at the slope by field measurements and numerical simulations to understand the mechanism of the displacement behavior after each heavy rainfall.

The purposes of continuous displacement monitoring are to assess the stability of slopes and to predict future failures. This research has only been focused on the monitoring task by continuous displacement monitoring using GPS. The judging task, using the displacement results, should be considered in future works.

The new GPS sensors provide a kinematic solution immediately after observing the signal phase, for example, every 1 second. When conducting the kinematic method for continuous monitoring for a long period, for instance, 1 year, the tropospheric delays cannot be ignored. Thus, an investigation is required in order to understand the effect of tropospheric delays during the long-term use of the kinematic method.

In Chapter 5, fundamental experiments were only conducted for two cases. It will be necessary to clarify to what extent the baseline length and the height difference affect the measurement accuracy. Furthermore, the duration of the experiments for detecting displacements were short, and only given displacements in the horizontal direction, latitude, and longitude, were performed. It will be essential to conduct further experiments for longer durations and in the vertical direction.

REFERENCES

Abramson L., Lee T., Sharma S, Boyce G. General slope stability concepts. In: Slope stability and stabilization methods. 2nd edition. John Wiley and Sons, Inc; 2002. p. 1–53.

Ashkenazi V, Bingley R, Dodson A, Pena N, Baker T. GPS monitoring of vertical land movements in the UK. In: Proceedings of the 11th International Technical Meeting of the Satellite Division of the US. Institute of Navigation, Nashville, Tennessee, USA, 1998. p. 99–107.

Avila A, Justino F, Wilsonl A, Bromwich D, Amorim C. Recent precipitation trends, flash floods and lanslides in southern Brazil. Enviromental Research Letters 2016;11(11):1–43.

Ballantyne JD, Dean DR, Thompson BL. Monitoring landslide movement with a 35 mm camera. Transportation Research Record 1988;1119:47–54.

Behr J, Hudnut K. Continuous GPS monitoring of structural deformation at Pacoima dam. Seismological Research Letters 1998;69(4):299–308.

Bellone T, Dabove P, Manzino AM, Taglioretti C. Real-time monitoring for fast deformations using GNSS low-cost receivers. Geomatics, Natural Hazards and Risk 2014;7(2):458–70.

Bertacchini E, Capitani A, Capra A, Corsini A, Dubbini M. Integrated Surveying System for Landslide Monitoring , Valoria Landslide (Appennines of Modena, Italy). In: Proceedings of FIG Working Week 2009. Eilat, Israel; 2009.

Biagi L, Grec F, Negretti M. Low-cost GNSS receivers for local monitoring: Experimental simulation, and analysis of displacements. Sensors 2016;16(2140).

Biagi L, Grec F, Negretti M, Visconti MG. Local monitoring by low cost devices and free and open sources softwares. In: Proceedings of FOSS4G Europe. Como; 2015. p. 431–6.

Bond J. An investigation on the use of GPS for deformation monitoring in open pit mines. Frederiction, New Brunswick, Canada, 2004.

Brown N, Troyer L, Zelzer O, Van Cranenbroek J. Advances in RTK and post processed monitoring with single frequency GPS. Journal of Global Positioning Systems 2006;5(1–2):145–51.

Brückl E, Brunner FK, Lang E, Mertl S, Müller M, Stary U. The Gradenbach Observatory-monitoring deep-seated gravitational slope deformation by geodetic, hydrological, and seismological methods. Landslides 2013;10(6):815–29.

Burkholder EF (ed). Special issue: GPS88. Journal of Survey Engineering 1988;114(4).

Burkholder EF (ed). Special issue: GPS88. Journal of Survey Engineering 1989;115(1).

Calcaterra S, Cesi C, Di Maio C, Gambino P, Merli K, Vallario M, Vassallo R. Surface displacements of two landslides evaluated by GPS and inclinometer systems: A case study in Southern Apennines, Italy. Natural Hazards 2012;61(1):257–66.

Chandler JH, Moore R. Analytical photogrammetry: a method for monitoring slope instability. Quarterly Journal of Engineering Geology and Hydrogeology 1989;22:97–110.

Chrzanowski A, Wells W (eds). Proceedings of the 5th FIG International Symposium on Deformation Measurements and the 5th Canadian Symposium on Mining Surveying and Rock Deformation Measurements. Fredericton, Canada; 1988.

Cina A, Piras M. Performance of low-cost GNSS receiver for landslides monitoring: test and results. Geomatics, Natural Hazards and Risk 2015;6(5–7):497–514.

Coe JA, Ellis WL, Godt JW, Savage WZ, Savage JE, Michael JA, Kibler JD, Powers PS, Lidke DJ, Debray S. Seasonal movement of the Slumgullion landslide determined from Global Positioning System surveys and field instrumentation, July 1998-March 2002. Engineering Geology 2003;68:67–101.

Cortez ER, Hanek GL, Truebe MA, Kestler MA. Simplified User's Guide to Time-Domain-Reflectometry monitoring of slope stability. The U.S. Department of Agriculture, 2009.

Cruden DM. A simple definitions of a landslide. Bulletin of the International Association of Engineering Geology 1991;43:27–9.

Dabove P, Manzino AM, Taglioretti C. GNSS network products for post-processing positioning: limitations and peculiarities. Applied Geomatics 2014;6(1):27–36.

Dach R, Lutz S, Walser P, Fridez P, editors. Bernese GNSS Software, Version 5.2. Astronomical Institute, University of Bern, 2015.

Dou J, Bui DT, Yunus AP, Jia K, Song X, Revhaug I, Xia H, Zhu Z. Optimization of causative factors for landslide susceptibility evaluation using remote sensing and GIS data in parts of Niigata, Japan. PLoS One 2015;10(7).

Dunnicliff J. Suggested motheds for surface monitoring of movements across discontinuites. International Journal of Rock Mechanics and Mining Sciences 1984;265–76.

Dunnicliff J. Geotechnical instrumentation for monitoring field performance. A Wiley-Interscience Publication, John Wiley and Sons 1988.

El-Rabbany A. Introduction to GPS - The Global Positoning System. Artech House, Inc, 2002.

Eyo EE, Musa TA, Idris KM, Opaluwa YD. Reverse RTK data streaming for low-cost landslide monitoring. In: Rahman AA, Boguslawski P, Anton F, Said MN, Omar KM, editors. Proceedings of Geoinformation for Informed Decisions. Springer, 2014. p. 19–33.

Flageollet J-C. The time dimension in the study of mass movements. Geomorphology 1996;15(3–4):185–90.

Gassner G, Wieser A, Brunner FK. GPS Software Development for Monitoring of Landslides. In: Proceedings of FIG XXII Congress Washington. USA. 2002. p. 1–12.

Geographical Survey Institute. The new geodetic reference system of Japan - Its adoption and application to our products. Bulletin of the Geographical Survey Institute 2004;50.

Gili JA, Corominas J, Rius J. Using Global Positioning System techniques in landslide monitoring. Engineering Geology 2000;55:167–92.

Gulla G, Nicoletti PG, Sorriso-Valvo M. A portable device for measuring displacements along fractures. In: Proceedings of 5th International Symposium on Landslides. Lausanne; 1988;1. p. 423–6.

Günther J, Heunecke O, Pink S, Schuhbäck S. Developments towards a low-cost GNSS based sensor network for the monitoring of landslides. In: Proceedings of 13th FIG International Symposium on Deformation Measurements and Analysis 4th IAG Symposium on Geodesy for Geotechnical and Structural Engineering. Lisbon; 2008. p. 1–10.

Gutiérrez F, Soldati M, Audemard F, Bălteanud D. Recent advances in landslide investigation: Issues and perspectives. Geomorphology 2010;124(3–4):95–101.

Hoek E, Read J, Karzulovic A, Chen ZY. Rock slopes in civil and mining engineering.

In: Proceedings of the International Conference on Geotechnical and Geological Engineering, GeoEng2000. Melbourne; 2000. p. 1–16.

Hofmann-Wellenhof B, Lichtenegger H, Collins J. Global Positioning System: Theory and Practice, 5th edition. Springer, 2001.

Hopfield HS. Two-quartic tropospheric refractivity profile for correcting satellite data. Journal of Geophysical Research 1969;74(18):4487–99.

Itasca. Universal Distinct Element Code User's Guide. Minneapolis, 2014.

Iwasaki T, Takechi K, Takeishi A, Masunari T, Takechi Y, Shimizu N. Web-based displacement monitoring system using GPS for the maintenance of roadside slopes. In: Proceedings of the 6th International Symposium on Field Measurements in Geomechanics, FMGM03. Oslo; 2003. p. 137–43.

Jäger R, González F. GNSS/LPS Based Online Control and Alarm System (GOCA) - Mathematical models and technical realization of a system for natural and geotechnical deformation monitoring and hazard prevention. In: Proceedings of Geodetic Deformation Monitoring: From Geophysical to Engineering Roles. Berlin; 2006. p. 293–303.

Janssen V, Rizos C. A mixed-mode GPS network processing approach for deformation monitoring applications. Survey Review 2003;37(287):2–19.

Kälber S, Jäger R. A GPS-based online control and alarm system. In: Proceeding of the 10th FIG International Symposium on Deformation Measurements. 2001. p. 164–74.

Kim D (Don), Langley RB, Bond J, Chrzanowski A. Local deformation monitoring using GPS in an open pit mine: initial study. GPS Solutions 2003;7:176–85.

Kitagawa G. Jikeiretsu Kaiseki Programming (Programming for Time series analysis), Iwanami Shoten. Tokyo; 1993. [In Japanese]

Kitagawa G, Gersch W. A smoothness priors-state space modeling of time series with trend and seasonality. Journal of the American Statistical Association 1984;79(386):378–89.

Koo G, Kim K, Yeon Chung J, Choi J, Kwon N-Y, Kang D-Y, Sohn H. Development of a high precision displacement measurement system by fusing a low Cost RTK-GPS sensor and a force feedback accelerometer for infrastructure monitoring. Sensors 2017;17(2745):1–20.

Lagler K, Schindelegger M, Böhm J, Krásná H, Nilsson T. GPT2: Empirical slant delay model for radio space geodetic techniques. Geophysical Research Letters 2013;40(6):1069–73.

Leandro RF, Santos MC, Langley RB. Neutral atmosphere models: development and performance. In: Proceedings of the 2006 National Technical Meeting of the Institute of Navigation. 2006. p. 564–73.

Leica Geosystems. Leica monitoring solutions certainty builds confidence. Switzeland; 2009;

Ma F, Zhao H, Zhang Y, Guo J, Wei A, Wu Z, Zhang Y. GPS monitoring and analysis of ground movement and deformation induced by transition from open-pit to underground mining. Journal of Rock Mechanics and Geotech Engineering 2012;4(1):82–7.

Malet JP, Maquaire O, Calais E. The use of global positioning system techniques for the continuous monitoring of landslides: Application to the Super-Sauze earthflow (Alpes-de-Haute-Provence, France). Geomorphology 2002;43(1–2):33–54.

Masunari T, Shimizu N. Meteorological influence and a correction method for GPS displacement measurements. Journal of Construction Engineering and Management, JSCE 2007;63(4):437–47. [In Japanese]

Masunari T, Takechi Y, Funatsu T, Shimizu N. Meteorological correction using atmospheric weather data of measurement cite for GPS displacement measurements. Journal of Construction Engineering and Management, JSCE 2009;65(3):356–63. [In Japanese]

Masunari T, Takechi Y, Tamura N, Funatsu T, Shimizu N. The influence of overhead obstacles to GPS displacement measurements and a method to reduce this influence. Journal of Construction Engineering and Management, JSCE 2008;64(4):394–402. [In Japanese]

Masunari T, Tanaka K, Okubo H, Oikawa H, Takechi K, Iwasaki T, Shimizu N. GPS-based continuous displacement monitoring system. In: Proceedings of the 6th International Symposium on Field Measurement Geomechanics, FMGM03. Oslo; 2003;537–43.

Misra P, Enge P. Global Positioning System: Signals, Measurements and Performance,

2nd Edition. Gange-Jamuna Press, 2011.

Mora P, Baldi P, Casula G, Fabris M, Ghirotti M, Mazzini E, Pesci A. Global Positioning Systems and digital photogrammetry for the monitoring of mass movements: Application to the Ca' di Malta landslide (northern Apennines, Italy). Engineering Geology 2003;68:103–21.

Moss JL. Using the Global Positioning System to monitor dynamic ground deformation networks on potentially active landslides. International Journal of Applied Earth Observation and Geoinformation 2000;2(1):24–32.

Nakashima S, Kawasaki H, Shimizu N. Monitoring of fill dams using GPS-based displacement measurement system. In: Proceedings of International Symposium on Dams for a Changing World. Kyoto; 2012a. p. 5-7 – 5-12.

Nakashima S, Shimizu N, Hirabayashi K, Masunari T, Iwasaki T, Ono M. Effects of correction of atmospheric delays on GPS displacement. Journal of MMIJ 2012b;128:255–64. [In Japanese]

Naya H, Kubo T, Nakashima S, Shimizu N. Diffusion Laser Displacement Meter for monitoring rock/ground displacement and its practical application. In: Proceedings of the 8th Asian Rock Mechanics Symposium. Sapporo; 2014. p. 2324–30.

Naya H, Mizokami M, Asari S, Masunari T, Shimizu N, Maeda H. Development of a displacement meter that uses a diffusion laser beam and verification of its practical applicability. Journal of the Japan Landslide Society 2008;44(6):339–48. [In Japanese]

Niell AE. Global mapping functions for the atmosphere delay at radio wavelengths. Journal of Geophysical Research 1996;101(B2):3227–46.

Oka N. Application of photogrammetry to the field observation of failed slopes. Engineering Geology 1998;50:85–100.

Perissin D, Wang T. Time-series InSAR applications over urban areas in China. IEEE Journal of Selected Topics in Applied Earth Observations and Remote Sensing 2011;4(1):92–100.

Peyret M, Djamour Y, Rizza M, Ritz JF, Hurtrez JE, Goudarzi MA, Nankali H, Chéry J, Dortz KL, Uri F. Monitoring of the large slow Kahrod landslide in Alborz mountain range (Iran) by GPS and SAR interferometry. Engineering Geology

2008;100(3–4):131–41.

Qin SQ, Wang SJ, Jiao JJ. The predictable time scale of landslides. Bulletin of Engineering Geology and the Environment 2001;59(4):307–12.

Rawat MS, Joshi V, Rawat BS, Kumar K. Landslide movement monitoring using GPS technology : A case study of Bakthang landslide , Gangtok , East Sikkim , India. Journal of Development and Agricultural Economics 2011;3:194–200.

Rizzo V. GPS monitoring and new data on slope movements in the Maratea Valley (Potenza, Basilicata). Physics and Chemistry of the Earth 2002;27(36):1535–44.

Rott H, Nagler T. The contribution of radar interferometry to the assessment of landslide hazards. Advances in Spaces Research 2006;37(4):710–9.

Saastamoinen J. Contributions to the theory of atmospheric refraction. Bullettin Géodésique 1972;105(1):279–98.

Saito H, Korup O, Uchida T, Hayashi S, Oguchi T. Rainfall conditions, typhoon frequency, and contemporary landslide erosion in Japan. Geology 2014;42(11):999–1002.

Scaringi G, Fan X, Xu Q, Liu C, Ouyang C, Domènech G, Yang F, Dai L. Some considerations on the use of numerical methods to simulate past landslides and possible new failures: the case of the recent Xinmo landslide (Sichuan, China). Landslides 2018;(January):1–17.

Schrader DK, Min B-C, Matson ET, Eric Dietz J. Real-time averaging of position data from multiple GPS receivers. Measurement 2016;90:329–37.

Shimizu N. Displacement monitoring by using Global Positioning System for assessment of rock slope stability. In: Proceedings of the 9th International Congress on Rock Mechanics. Paris; 1999. p. 1435–8.

Shimizu N. Monitoring rock deformation using Global Positioning System - Fundamentals, new developments and practical applications. In: Proceedings of Korea-Japan Joint Symposium on Rock Engineering. 2009. p. 17–43.

Shimizu N, Koyama S, Ono H, Miyashita K, Kondo H, Mizuta Y. Field experiments and data processing for continuous measurements by the GPS displacement monitoring system. Journal of the Mining and Materials Processing Institute Japan 1997;113:549–54. [In Japanese]

Shimizu N, Masunari T, Iwasaki T. GPS displacement monitoring system for the

precise measuring of rock movements. In: Qian, Zhou, editors. Harmonising Rock Engineering and the Environment: Proceedings of 12th ISRM International Congress on Rock Mechanics, 2011, Beijing. London: Taylor & Francis Group; 2012. p. 1117–20.

Shimizu N, Matsuda H. Practical applications of the Global Positioning System for the assessment of slope stability based on the Displacement Monitoring Approach. In: Proceedings of 3rd Korea-Japan Joint Symposium on Rock Engineering, ISRM Regional Symposium. Seoul; 2002. p. 57–70.

Shimizu N, Mizuta Y, Kondo H, Ono H. A new GPS real-time monitoring system for deformation measurements and its application. In: Proceedings of 8th FIG International Symposium on Deformation Measurements. Hongkong; 1996. p. 47–54.

Shimizu N, Nakashima S. Review of GPS displacement monitoring in rock engineering. In: Feng X-T, editor. Rock Mechanics and Engineering; 2017. p. 593–626. [Chapter 19]

Shimizu N, Nakashima S, Masunari T. ISRM suggested method for monitoring rock displacements using the global positioning system (GPS). Rock Mechanics and Rock Engineering 2014;47:313–28.

Slope Indicator. Geotechnical and Structural Instrumentation, Volume VI. Durham Geo Slope Indicatior, 2011.

Smelser D. Landslide mitigation action plan, Final report. Washington State Department of Transportation, 2014.

Squarzoni C, Delacourt C, Allemand P. Differential single-frequency GPS monitoring of the La Valette landslide (French Alps). Engineering Geology 2005;79:215–29.

Stewart M, Tsakiri M. The application of GPS to dam surface monitoring. Journal of Geospatial Engineering 1993;3(1):45–57.

Szostak-Chrzanowski A, Chrzanowski A. Interdisciplinary approach to monitoring, analysis, and modeling of deformations. Electronic Journal of Polish Agricultural Universities 2008;11(2).

Tagliavini F, Mantovani M, Marcato G, Pasuto A, Silvano S. Validation of landslide hazard assessment by means of GPS monitoring technique – a case study in the Dolomites (Eastern Alps, Italy). Natural Hazards and Earth System Science

2007;7:185–93.

Takasu T, Yasuda A. Development of the low-cost RTK-GPS receiver with an open source program package RTKLIB. In: Proceedings of the International Symposium on GPS/GNSS. Jeju; 2009.

Taşçi L. Dam deformation measurements with GPS. Geodesy and Cartography 2008;34(4):116–21.

Terada S. Fundamental developments of a GPS sensor for continuous spatio-temporal displacement monitoring. Master thesis, Yamaguchi University, 2017. [In Japanese]

Tyuji M. Survey. Maruzen Kabushikigaisya, 1979. [In Japanese]

US Army Corps of Engineers. Monitoring structural deformations using the global positioning system. In: Structural Deformation Surveying, Engineer Manual EM 1110-2-1009; 2002. p. 8-1 − 8-42. [Chapter 8]

Vermeer M. Review of the GPS deformation monitoring studies. In: STUK-YTO-TR 186. Helsinki; 2002;

Wang G. GPS landslide monitoring: Single base vs. Network solutions — A case study based on the Puerto Rico and Virgin Islands Permanent GPS Network. Journal of Geodetic Science 2011;1(3):191–203.

Wang G, Soler T, Asce M. OPUS for horizontal subcentimeter-accuracy landslide monitoring: Case study in the Puerto Rico and Virgin islands region. Journal of Survey Engineering 2012;138(3):143–53.

Wang GQ. Kinematics of the Cerca del Cielo, Puerto Rico landslide derived from GPS observations. Landslides 2012;9(1):117–30.

Wyllie DC, Mah CW. Rock slope engineering civil and mining. Taylor & Francis Group, 2004.

Xiao R, He X, Li L. Continuous monitoring of landslide and atmospheric water vapor using GPS: Application in Pubugou hydropower resettlement zone. China Satellite Navigation Conference 2012. p. 305–13.

Yin Y, Zheng W, Liu Y, Zhang J, Li X. Integration of GPS with InSAR to monitoring of the Jiaju landslide in Sichuan, China. Landslides 2010;7:359–65.

Zhang L, Schwieger V. Investigation of a L1-optimized Choke Ring Ground Plane for a low-cost GPS receiver-system. Journal of Applied Geodesy 2017;12(1):55–64.

Zhang L, Stange M, Schwieger V. Automatic low-cost GPS monitoring system using WLAN communication. In: Proceedings of the FIG Work Week 2012 - Knowing to Management the Territory, Protection the Environment Evaluate Cultural Heritage. 2012. p. 1–17.

Zhu W, Zhang Q, Ding X, Zhao C, Yang C, Qu F, Qu W. Landslide monitoring by combining of CR-InSAR and GPS techniques. Advances in Spaces Research 2014;53:430–9.